The importance of Joule heating on the voltage-triggered insulator-to-metal transition in VO_2

by

Alyson Spitzig

B.Sc., Dalhousie University, 2015

A THESIS SUBMITTED IN PARTIAL FULFILLMENT OF
THE REQUIREMENTS FOR THE DEGREE OF

MASTER OF SCIENCE

in

The Faculty of Graduate and Postdoctoral Studies

(Physics)

THE UNIVERSITY OF BRITISH COLUMBIA

(Vancouver)

October 2018

© Alyson Spitzig 2017

Abstract

The large change in resistivity in VO_2 has attracted considerable attention since VO_2 was first discovered in 1959. Recently, the ability to trigger the insulator-to-metal transition (IMT) with a strong electric field has been observed, but there has been debate about whether the transition is due to field-effects. We apply a voltage bias across a VO_2 thin film via a conductive atomic force microscope (CAFM) tip and measure the resultant current. We observe the IMT as a jump in the measured current in the IV curves. We fit the IV curves to the Poole-Frenkel (PF) conduction mechanism in the insulating state, immediately preceding the IMT. The PF conduction mechanism describes the thermal excitation of electrons into the conduction band in insulators, facilitated by strong electric fields. The PF mechanism is temperature dependent, and we use the temperature dependence to calculate the local temperature of the film before the transition. We directly compare the local electric field and local temperature of the film immediately preceding the IMT. We determine that the transition is not solely due to the applied electric field, but rather that the tip has locally warmed the film close to its IMT temperature through Joule heating.

Preface

The results of this thesis are to be published later in 2017. The film studied was grown and characterized by Changhyun Ko and Shiriram Ramanthan. IV measurements, and preliminary analysis were performed by Hoffman group members Adam E. Pivonka, Harry Mickalide, Alex Frenzel, Jeehoon Kim, Kevin O'Connor, and Eric Hudson. Dielectric constant measurements of VO_2 were taken by You Zhou and Changhyun Ko. The author, Alyson Spitzig completed all calculations and conclusions therein, with mentorship by Jennifer E. Hoffman and Jason D. Hoffman.

Table of Contents

Abstract ii

Preface iii

Table of Contents iv

List of Tables vi

List of Figures vii

Acknowledgements x

Dedication xi

1 Introduction 1
- 1.1 Literature Review 5

2 Data Collection and Correction 9
- 2.1 Conductive Atomic Force Microscopy 9
- 2.2 VO_2 Film Growth and Characterization 10
  - 2.2.1 Physical Film Properties 10
  - 2.2.2 Dielectric constant of VO_2 12
- 2.3 *IV* Collection and Correction 15
- 2.4 Conduction Mechanisms in Insulators 30
- 2.5 A Second Data Set 37

3 Analysis 40
- 3.1 Electric field 40
- 3.2 Poole-Frenkel Fitting 41
- 3.3 Temperature 46
  - 3.3.1 Number of Jumps 47
- 3.4 Discussion 49

4 Nanoscale Thermometry 52
4.1 Other Nanoscale Thermometry Techniques 52
4.2 Extension of Thermometry Technique 58

5 Conclusion 61

Bibliography 62

Appendices

A Power Gradient 76
A.1 Input energy from tip 77
A.2 Heat required to cause IMT in VO_2 78
A.3 Thermal Conductivity of SiO_2 78

B Uncertainty in the calculated Temperature 83
B.1 Dielectric contant, $\varepsilon_{\mathrm{V}}(T)$ 84
B.2 Thickness, d 85
B.3 PF slope, P 85
B.4 Temperature, T 86

C Model Circuit and Bounding Circuit Element Values . . . 90
C.1 Setting up equations for the upsweep 90
C.2 Solving the case of the Insulating State 92
C.2.1 Current through R_2 92
C.2.2 Current through the film 93
C.2.3 Current through the capacitor 94
C.3 Solving the case of the Metallic State 94
C.3.1 Current through R_2 95
C.3.2 Current through the film 95
C.4 Setting up equations for the downsweep 98
C.4.1 Current through the film 98
C.4.2 Lower bound on R_2 98
C.5 Summary 99

List of Tables

2.1 Summary of previous measurements of ε_{V}. 12
2.2 Measured or calculated values of the effective resistance and decay time in our data. 18
2.3 Measured or calculated values of circuit components from the case where the capacitor is in parallel with both the film and the external resistance. 20
2.4 Measured or calculated values of circuit components from the case where the capacitor is in parallel with the film. 22
2.5 Measured or calculated values of circuit components from the case where the capacitor is in parallel with the external resistance. 23
2.6 Measured or calculated values of circuit components from the case where the capacitor is in parallel with part of the external resistance. 25
2.7 Summary of conduction mechanisms in insulators. 31
2.8 List of variables in conduction mechanisms. 32

4.1 Summary of nanoscale thermometry techniques. PF conduction refers to the technique described in this paper. 57

List of Figures

1.1 Morin's first measurements of the metal-to-insulator transition of Ti- and V- oxides 2
1.2 Structure of VO_2 above (left) and below (right) the structural phase transition, around 340 K. 3
1.3 Observation of voltage triggered IMT. 4
1.4 Band representation above (left) and below (right) the electronic transition temperature. 5
1.5 Hall carrier density across the IMT. 6
1.6 Plane representation of the V atoms' distortion from the rutile structure 7

2.1 Diagram of CAFM 10
2.2 Bulk film characterization. 11
2.3 Nanoscale film characterization. 12
2.4 All measured dielectric constant data for VO_2 of varying thickness on various substrates. 13
2.5 Different functional forms considered when fitting Ko's ε_V data. 14
2.6 The raw data with the current spike and exponential decay in both the ramping up and down data. 16
2.7 Exponential decay in the IV data when ramping up the voltage. 17
2.8 Exponential decay in the IV data when ramping down the voltage. 18
2.9 Possible effective circuit diagrams. 19
2.10 Possible effective circuit diagram and resultant IV curve for a stray capacitance in parallel with both the film and external resistance. 21
2.11 Possible effective circuit diagram and resultant IV curve for a stray capacitance in parallel with only the film. 22
2.12 Possible effective circuit diagram and resultant IV curve for a stray capacitance in parallel only the external resistance. . . 24

2.13 Possible effective circuit diagram and resultant IV curve for a stray capacitance in parallel with only part of the external resistance. 25
2.14 Final IV simulation output current, decomposed into signal from each component. 26
2.15 Final IV simulation output current, for voltage ramping down. 26
2.16 Final calculated temperature as a function of increased current through I_C. 28
2.17 Final calculated temperature as a function of increased metallic state resistance of VO_2 29
2.18 Energy band diagram of likely conduction mechanisms. 33
2.19 A typical IV curve before the transition from the data analyzed in this thesis, linearized for each of the conduction mechanisms in insulators. 35
2.20 Topography from the dataset A. 37
2.21 A typical IV curve from the first data set for the applied voltage ramping up and down. 38
2.22 A typical IV curve before the transition from data set A, linearized for each of the conduction mechanisms in insulators. 39

3.1 Electric field at the transition. 41
3.2 The PF slope at each point on the image. 42
3.3 A representative PF linearized IV curve with the minimized PF fit. The red star marks the numerical inflection and the yellow line indicated the fit minimum PF slope. 42
3.4 A typical PF linearized IV curve, with black points indicating the center of a fixed length 21-point fitting region and the corresponding PF slope and rms error. 44
3.5 The PF slope as a function of number of data points and colorbar corresponding to the rms error. 45
3.6 Relation between the dielectric constant, PF slope and temperature of the film. 45
3.7 Temperature of the film immediately preceding the transition. 47
3.8 PF linearized IV curves from adjacent pixels with multiple jumps, one fit above and one fit below the first, smaller transition. 48
3.9 A trimodal map of the number of jumps in each IV curve. . . 49
3.10 Examples of IV curves that are too noisy, or calculate physically unreasonable temperatures. 51

4.1 The Au-Cr junction on the tip in Kim's thermal probe technique. 53
4.2 Al plasmon shift at two temperatures. 55
4.3 Thermo-resistive scanning probe. 59
4.4 Reported applicable temperature ranges and spatial resolution of thermometry techniques. 60

A.1 Map showing the voltage (a) and current (b) through the film at the transition. 76
A.2 Energy input into the film via the tip. 77
A.3 SiO_2 thermal conductivity $\kappa(T)$. 80
A.4 Approximation of the temperature using a sweeping PF fit. . 82
A.5 Energy leaked through the SiO_2 interface as a function of SiO_2 thickness. 82

B.1 The uncertainty associated with fitting a straight line to an IV curve. 85
B.2 A representative curve, with the maximum domain PF slope. 86
B.3 A map of the slope found by considering the largest voltage range at each IV curve. 87
B.4 Comparison of fitting the slope with different conditions on the fitting region. 87
B.5 The uncertainty in the PF slope due to choosing a fitting region. 88
B.6 The total uncertainty in the PF slope at each point in the image. 88
B.7 The uncertainty in the temperature at each point in the image. 89

C.1 The circuit we consider. 91
C.2 IV curves. 97
C.3 Plot of Eqn. C.45 showing R_2 as a function of $R_{\text{total,i}}$. 99
C.4 Wide area maps of insulating state resistance of the film ($R_{1,\text{i}}$), external resistor 2 (R_3), and the capacitance (C). 100
C.5 Same as above, but only calculated over the region where all constraints are satisfied. 100
C.6 Maps showing the various correction terms to the voltage across the film. 101

Acknowledgements

I would like to take this opportunity to thank my supervisor Professor Jennifer Hoffman, for first taking me on as a Master's student, and then a PhD candidate. From the start of my Master's degree at The University of British Columbia, and continuing with my studies at Harvard University, she has challenged me and helped me improve as a researcher and a scientist.

I would also like to thank Dr. Jason Hoffman, for his continued patience, feedback, and improvements on my work.

Thank you to Professor Mona Berciu for fitting my thesis into her busy schedule.

Dedication

To all my friends, old and new, who helped me get to this point.
And of course to my family, without which I probably would have gotten here sooner.

And of course.. *coffee* ☕

Chapter 1

Introduction

Transition metal oxides host a wide range of properties. Due to their partially filled *d* bands and many valence states, transition metals can form many different compounds when combined with oxygen. Transition metal oxides can be paramagnetic (Ti_2O_3, VO_2), antiferromagnetic (FeO, NiO), ferrimagnetic (Mn_3O_4), ferromagnetic (CrO_2), or diamagnetic (TiO_2, CrO_3). They also display various electronic properties such as charge density waves ($K_{0.3}MoO_3$), defect ordering ($Ca_2Mn_2O_5$, $Ca_2Fe_2O_5$), insulator-to-metal transition (IMT) (VO_2, V_2O_3, $La_{1\text{-}x}Sr_xVO_3$), and superconductivity ($YBa_2Cu_3O_7$) [1]. Of particular interest, and focus of this thesis, is the IMT observed in vanadium dioxide, VO_2.

In 1959, Morin first reported the 4 order of magnitude change in the conductivity of VO_2 at 340 K (Fig. 1.1) [2]. Morin also reports the IMT in the lower oxide states; V_2O_3 has an IMT at 160 K and VO at 120 K. The IMT temperature of VO_2 is the closest to room temperature of the V-O phases, and of the 2 vanadium oxides that show an IMT above room temperature it has the largest change in conductivity [3]. The large and sudden change in conductivity close to and above room temperature makes VO_2 particularly applicable for a range of sensors and switches, such as broad-band all-optical switching [4], nano-mechanical resonators [5], window coatings [6–8], and electro-optic modulators [9]. The phase transition in VO_2 is very close to room temperature, thermodynamically stable, and can be triggered by an applied voltage [3, 10], making it well suited for use in next generation Mott transition field effect transistors [11], or a phase change memristor, the missing circuit element [12–14].

In 1961, shortly after the discovery of the IMT, Westman observed that VO_2 undergoes a structural phase transition (SPT) at the same temperature, 340 K [15]. VO_2 transitions from monoclinic (M1) at room temperature (as assumed by Morin), to a rutile (R) structure when heated above 340 K (nominally, in the metallic state). A schematic of the two lattice structures is shown in Fig. 1.2, with the rutile phase on the left and monoclinic on the right.

These two transitions initiated a long debate of whether VO_2 is a Mott

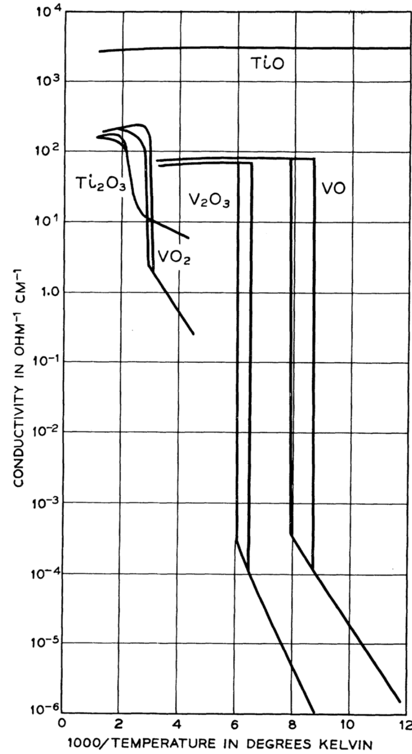

Figure 1.1: Morin's first measurements of the metal-to-insulator transition of Ti- and V- oxides. Conductivity as a function of reciprocal temperature for the lower oxides of titanium and vanadium. Measurements were made along the [100] direction in VO, and along the c axis in V_2O_3 and VO_2 [2].

or a Peierls insulator. A Mott insulator is a material that, by conventional band theory, would conduct electricity but instead, due to strong on-site electron-electron repulsion, it is energetically unfavorable for two electrons to occupy the same site. In these materials, half-filling locks each electron to its site, and resists the flow of electricity, resulting in an insulator. In the insulating state of a Mott insulator the electrons tend to anti-align, forming an antiferromagnetic phase [17], however VO_2 does not have a magnetically ordered ground state. The Peierls distortion is based on a one-dimensional chain of atoms minimizing energy by forming dimers. In a Peierls insulator, when the dimers from the lattice constant doubles and halves the Brillouin zone, which opens a gap at the Fermi level. In this case, once again, half-filling results in a full band, and thus an insulator. Due to how the V-V atoms

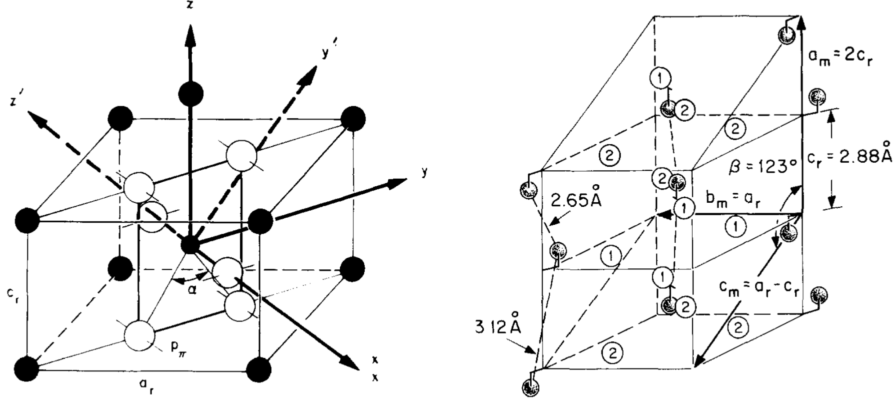

Figure 1.2: Rutile structure (R) of VO_2 above (left) and monoclinic structure (M1) of VO_2 below the SPT (right). Open circles are O^{2-} ions, dark circles are V^{4+} ions. Notice that approximately 2 rutile unit cells (left) make up one monoclinic unit cell (right). Reproduced from Goodenough [16].

pair and the electronic structure of the orbital polarization, the electronic structure of VO_2 is effectively a one-dimensional system [18].

In Sect. 1.2 we give a more detailed overview of the developments in the literature with regard to VO_2. Many theories and experiments find arguments for the material to be Mott [19], Peierls [20], or some combination of both [21].

Regardless of the driving force behind the IMT, multiple groups have reported a voltage triggered transition to the metallic state, observed as a sudden jump in the measured current, shown in Fig. 1.3 [10, 21–26]. However, this voltage induced transition has raised several important questions that we address in this work: By which mechanism is the applied voltage triggering the transition? When high electric fields are applied across a VO_2 film, what is the local temperature of the film?

To answer these question we image the temperature of a VO_2 thin film on the nanoscale under an applied voltage bias. Film growth and characterization details are given in Sect. 2.2. We analyze current-voltage (IV) curves measured with a conductive atomic force microscope (CAFM) (Sect. 2.1). First, the raw IV curves must be corrected to ensure that we are analyzing the current and voltage through the film, not any external resistances or components (Sect. 2.3). Using the IV through the film, we conclude that the Poole-Frenkel (PF) conduction mechanism is the dominant mechanism in our film (Sect. 2.4).

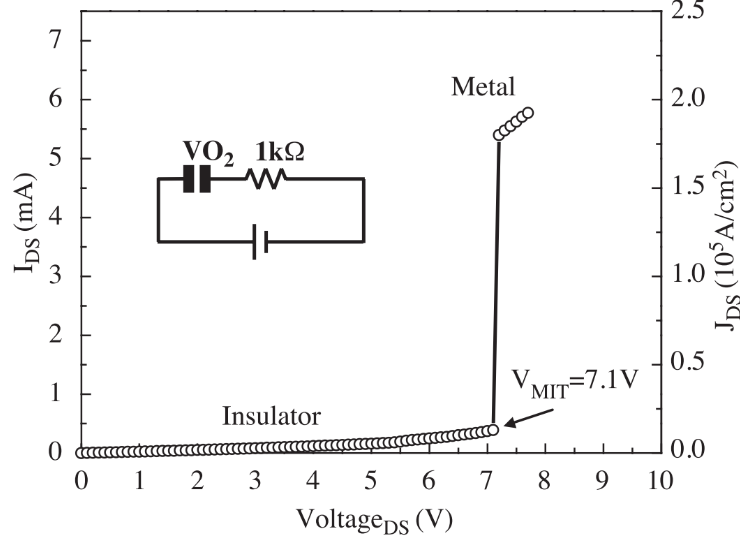

Figure 1.3: Abrupt IMT induced by a DC voltage in a VO_2 thin film. The inset displays the circuit used for experiments. The left y-axis, I_{DS} is the drain-source current and the right y-axis, J_{DS} is the corresponding current density. Reproduced from Chae *et al.* [22].

Next, we find the applied bias voltage at the transition and, along with the local film thickness, calculate the electric field at the transition (Sect. 3.1). We fit the *IV* curves to the PF conduction mechanism (Sect. 3.2), which then enables us to extract the temperature of the film immediately preceding the transition (Sect. 3.3).

In Chapter 4 we briefly consider nanoscale thermometry. We first reflect on our novel technique (Sect 4.1), then discuss our thermometry technique in relation to existing methods (Sect. 4.2), and consider the possibility of extending our technique to other materials (Sect. 4.3).

In Chapter 5, we compare the electric field and temperature at the transition. The electric field at the transition is found to be consistent with previous reports of an electric-field assisted transition [21, 24, 27]. We calculate that the average local temperature immediately preceding the transition is 335 K, and conclude that Joule heating plays an important role in triggering the IMT.

1.1 Literature Review

With the discovery of the SPT in VO_2, many theories arose with the assumption that the structural transition caused the electronic transition [28, 29]. In 1971, Goodenough described the electronic transition in terms of the V $3d$ band splitting into t_{2g} and e_g levels, with the t_{2g} bands arising from the d orbitals parallel with the rutile c axis, $d_{||}$. Through the structural transition, the pairing of the V-V bonds splits the $d_{||}$ orbitals, and the antiferroelectric zig-zag-type displacement raises the π^* band, opening a gap at the Fermi energy, as shown in Fig. 1.4. Nevertheless, Goodenough claims the electronic transition is predominantly due to the antiferroelectric distortion in the VO_6 octahedra as opposed to the V-V pairing [16]. Numerical calculations also suggested that the insulating state arises from the band splitting caused by the monoclinic distortion [30]. Eventually DFT and LDA calculations validated Goodenough's predictions [31].

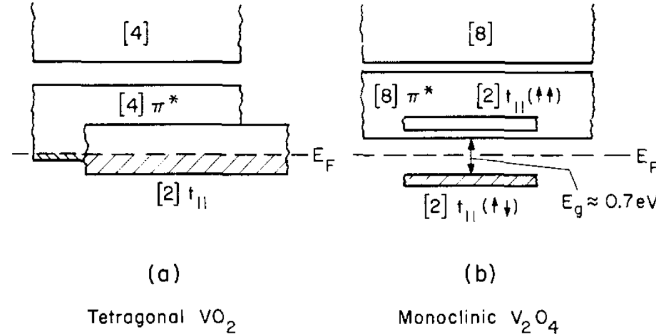

Figure 1.4: Band representation above (left) and below (right) the electronic transition temperature [16].

In these early studies, defects such as V-vacancies and oxygen non-stoichiometry strongly influenced properties such as conductivity, thermal properties, optical properties, and activation energy, which led to large variations between samples [28]. Nevertheless, it was concluded that the carriers in VO_2 are electrons and have relatively low mobility and density. Mobilities of 0.1 - 1 $cm^2/(V{\cdot}s)$ in the insulating state and 1 - 10 $cm^2/(V{\cdot}s)$ in the metallic state were found. This relatively small change in mobility cannot account for the large change in conductivity, suggesting that metallic state is due to an increase in carrier density [28, 29]. Zylbersztejn and Mott studied the nature of the carriers in VO_2 through Cr and Nb doping. They concluded

that Goodenough's band picture is correct for the metallic state, but that the insulating state arises from electron correlations, and a local Hubbard model [32].

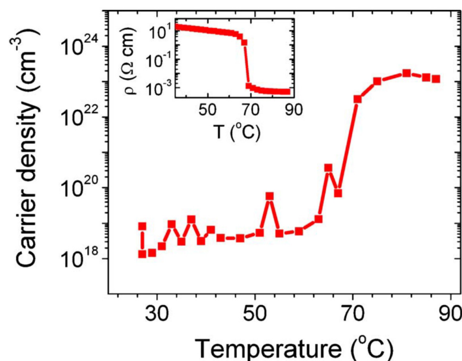

Figure 1.5: Carrier density of a VO_2 film measured using 1.4 T fixed field apparatus. The resistivity of the film is displayed in the inset. Reproduced from Ruzmetov *et al.* [33].

Doping and strain have been used to synthesize and investigate new phases of VO_2. Marezio stabilized an intermediate lattice distortion, labelled M2, with Cr-doping. In this intermediate phase, half the V chains pair and move closer, while the other half rotate out of the rutile c axis [34]. The two distorted phases, which occur on alternating V chains, are shown in Fig. 1.6, with respect to a rutile lattice plane. The same intermediate phase was also found to be stabilized with Al doping [35], and through uniaxial stress along the $[110]_R$ direction [36]. Pouget and Launois also stabilized a transitional phase (T) between M1 and M2, once again through Cr-doping and uniaxial stress. In the T phase the alternating chains of V-V pairs twist slightly off-axis, and the off-axis V atoms form pairs, although neither chain completely enters the M1 phase [37]. The M2 phase showed that the zig-zag distortion is coupled to the V-V pairing distortion on alternating chains. The M2 phase is a metastable modification of the M1 phase, whose free energy is only slightly higher than the M1 phase at room temperature and pressure. Interestingly, the M2 phase transition to the metallic state is consistent with a Mott-Hubbard transition [37, 38]. The discovery of the M2 phase separated V into two sub-lattices, which was difficult to account for by band theories at the time. Up to this point, theories had described the insulating state as a consequence of the monoclinic crystal distortion, but now electron correla-

tions were deemed essential to the transition [31]. Although the importance of electron correlations cannot be denied, the question remains whether the Coulomb interaction opens the Peierls gap [18, 39, 40], or if the pairing V atoms induce a Mott instability [41].

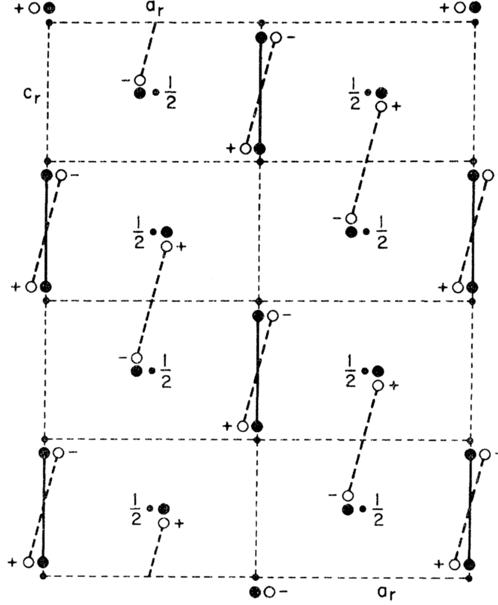

Figure 1.6: Plane representation of the V atoms distortion from the rutile structure [34]. In the M1 phase (open circles) all the V atoms both pair and twist from the rutile positions. In the M2 phase (filled circles) half of the V atoms pair but do not twist and the other half form un-paired zig-zag chains. (The distortions from the rutile structure are exaggerated by a factor of 2 for clarity.)

Using a metal-oxide-metal sandwich structure, Stefanovich triggered the transition with voltage pulses, and found that the delay time of the transition was dependent on the magnitude of the voltage pulse [42]. He found that a simple thermal model did not accurately describe the delay time, and concluded that in strong electric fields the transition cannot be described by an electrothermal model alone. Shortly after, Boriskov surmised that the conductivity must be electric field dependent, and determined that VO_2 followed the PF conduction mechanism for increasing charge carrier density [43, 44]. There are many mechanisms by which electrons can conduct through an insulator, influenced either by high fields or temperature,

including Schottky emission, Fowler-Nordheim Tunneling, thermionic-field emission, direct tunneling, PF conduction, hopping conduction, Ohmic conduction, space charge-limited conduction and ionic conduction [45]. In Sect. 2.4 we will consider all mechanisms and independently conclude that the dominant mechanism is in fact PF conduction.

While the microscopic origin of the IMT remains unclear, in recent years the focus has turned to fabricating high quality films, and directly controlling the transition for potential applications. It has been found that IMT can be induced by ultra fast laser pulses [5, 46–49] or the application of strong electric fields or voltage pulses [10, 21–26]. The electronic transition can be affected by changes in strain, either by varying the substrate [19, 50–54], or doping the film [35, 55, 56]. Films have been grown on Si(001), *c*-, *r*-, and *m*- plane Al_2O_3 [57, 58], TiO_2(001) and TiO_2(110) [59], and Ge(100) [60]. It was found that by stretching the c axis the IMT temperature is increased, and by compressing the c axis it is reduced [59].

In the last couple of years, studies on VO_2 have shifted toward for more specialized potential applications. The reversibility of the phase transitions are being investigated for applications in H storage [61], memristors [62], and hybrid metamaterial switching [63]. Films grown by oxide molecular beam epitaxy can finely control V-O stoichiometry, and is it found that the IMT temperature can be lowered through the formation of O-vacancies, but in doing so the resistivity change is also reduced [64]. O-vacancies can also induced through strong applied electric fields, reducing and eventually suppressing the IMT [53]. O-vacancy formation, diffusion, and recovery are studied for the potential application of ionic-liquid gating on VO_2 [65].

A delay between the IMT and SPT has been realized, where a metallic monoclinic phase has been observed [66–69]. Strain has also been used to completely suppress the SPT, while preserving the IMT. [19]

Many groups have observed the coexistence of the insulating and metallic phases, dating back to 1966 [70], but the phenomenon has been brought to the forefront more recently [10, 71, 72]. Phase coexistence suggests that the IMT originates in one region, and slowly spreads to the rest of the crystal or film. The percolation behavior was first observed indirectly through small avalanches the IMT in bulk IV measurements [73], followed by the observation of persistent metallic domains below the IMT [74], and finally was probed on the nanoscale in local IV maps [10, 72]. The SPT is also found to percolate through the film [75]. The percolation of the transitions has sparked interest in nanoscale measurements to shed some light on the origin of the IMT and SPT.

Chapter 2

Data Collection and Correction

2.1 Conductive Atomic Force Microscopy

A conductive atomic force microscope (CAFM) uses a probe consisting of a cantilever with a tip that comes to a point with a radius on the order of a 35 nm. A diagram of the basic geometry is shown in Fig. 2.1. An input laser signal is split, and 90% of the signal is fed into a variable optical attenuator as a reference signal to subtract off any noise from laser fluctuations. The remaining 10% intensity enters a custom single mode fiber, exits the flat end of the fiber and reflects off the end of the cantilever where it interferes with the incoming signal. The interference is measured by a balanced photodiode detector. The interference measures tip deflection, which is used to image the three-dimensional shape of the surface and provide z deflection feedback to keep the force between the tip and the surface constant. The tip can also be used to manipulate the surface through strong applied voltages. In contact mode, the current through the film is simultaneously measured by the conductive cantilever. CAFM can measure currents in the range of 2 pA to 1 μA.

We use a home-built AFM with a conductive cantilever in contact mode (cantilever with typical spring constant $k_c = 45$ N/m [1]). An interferometer of wavelength 1550 nm is used. In contact mode, we fix the cantilever deflection at a typical height of 7 nm, maintaining a constant force of $\sim$ 320 nN between the probe and sample. Applying pressure along the c-axis of VO_2 shifts the transition temperature at a rate of -1.2 K/kbar [76]. Assuming a tip contact radius of $\sim$ 35 nm we calculate the pressure applied by the tip to be 8.2 $\times 10^7$ Pa, or 820 bar. This pressure corresponds to a maximum shift of the IMT temperature of about 1 K, so we are far from initiating the transition through the applied pressure due to the tip.

[1] part number: HQ:NSC16/Cr-Au, purchased from μmasch: http://www.spmtips.com/nsc/16/cr-au

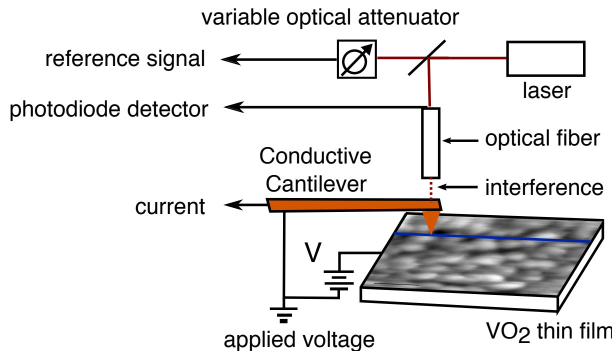

Figure 2.1: Diagram of a CAFM. The tip rasters the surface of the film and the z deflection is recorded by laser interferometry. When collecting electronic measurements the voltage bias between the film and tip is ramped and the resultant current is measured.

2.2 VO_2 Film Growth and Characterization

2.2.1 Physical Film Properties

The VO_2 film we study was grown by rf sputtering from a VO_2 target (99.5% AJA International Inc.) [77]. A VO_2 target is used in place of typical reactive V sputtering because using a VO_2 target preserves the stoichiometry, expanding the range of stable growth parameters [57]. The chamber base pressure was maintained at 3×10^{-8} Torr. The rf gun power is set to 270 W.

A heavily As-doped Si(001) substrate (ρ = 0.002 - 0.005 Ω cm) was heated at 550 °C during growth [77]. X-ray diffraction (XRD) data, using a ScintagXDS2000, with Cu $K\alpha$ radiation ($\lambda \sim 1.5418$ Å) indicates a polycrystalline monoclinic VO_2 film, with primary surface the (011) orientation (Fig. 2.2 (a)) [10].

Cross sectional transmission electron microscopy (TEM) measured the average thickness of the film to be 187 nm (Fig. 2.3 (a)). Also observed in the TEM image is a thin SiO_x interfacial layer, measured to be $\sim$ 2 nm thick. Topography from z deflection of CAFM gives the spatial height variation of a 500×500 nm^2 region of the film surface. The topography is shown in Fig. 2.3 (c), where individual grains can be seen. The local thickness of the film is calculated by adding the z deflection measured and the average thickness, giving local film thicknesses in the range of 167 nm to 207 nm. A typical line cut trace (shown in Fig. 2.3 (b)) demonstrates the surface roughness and approximate grain size. The root mean square (rms) roughness R_{RMS}

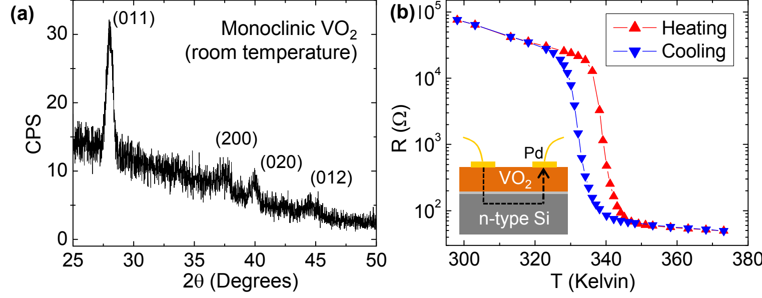

Figure 2.2: (a) XRD profile of the VO_2 film studied. Multiple peaks are observed, corresponding to a polycrystalline film, but the (011) orientation is most prominent. (b) The resistance-temperature measurement of the VO_2 film studied. Reproduced from Kim *et al.* [10].

is calculated by

$$R_{\mathrm{RMS}} = \sqrt{\frac{1}{n}\sum_{1}^{n}(\Delta y)^2}. \tag{2.1}$$

R_{RMS} of the image is 6.3 nm.

We estimate the average grain diameter in two ways. First, using the cross sectional TEM image, we measure the total length of the image to be 545 nm, and divide by the number of grains (7). This one dimensional measurement gives a rough estimate of the grain diameter to be 78 nm. The second method uses the full topography, shown in Fig. 2.3 (c), where the total grains are counted (48), and the length and width are measured. The average of the grain length and width is taken to be the diameter of the grain. This two dimensional measurement gives an average diameter of 67 nm, with a deviation of 13 nm. We estimate the average grain diameter to be $\sim$ 72 nm.

Resistance measurements of the film as a function of temperature gives the IMT temperature of our film to be about 339 K upon heating, and around 334 K while cooling (Fig. 2.2 (b)). A voltage bias was applied between two neighboring 500×500 $\mu\mathrm{m}^2$ Pd contact pads, 1 mm apart. The resistance through the VO_2 film was calculated from the measured current between the pads. Varying the distance between the pads did not change the resistance, verifying that the current flowed vertically through the film (as shown in the inset in Fig. 2.2 (b)), and that there was negligible resistance from the Si substrate.

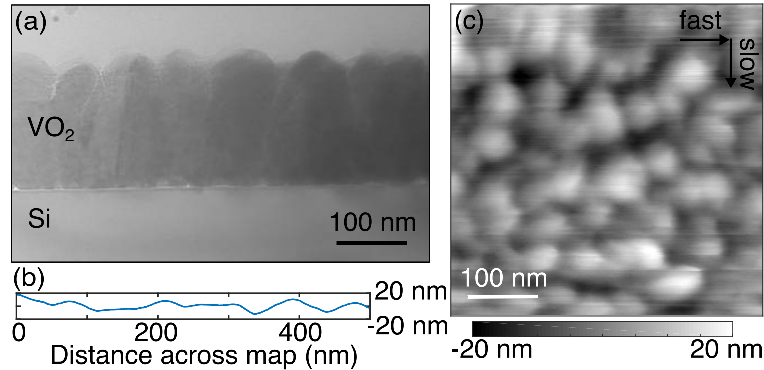

Figure 2.3: (a) Cross sectional TEM image of the VO_2 film studied. An average thickness of 187 nm is measured. (b) A line cut from the topography measured by AFM showing the typical height variation across the map. (c) An AFM image of the surface of the VO_2 film, where individual grains can be seen.

2.2.2 Dielectric constant of VO_2

There have been many measurements of the dielectric constant of VO_2, labelled ε_V, with some of these measurements presented in Table 2.1 and Fig. 2.4.

Table 2.1: Summary of previous measurements of ε_V. Also plotted Fig. 2.4.

Author	Film	Substrate	Temp. (K)	ε_V
Zylbersztejn [32]	single crystal	-	298	39
Barker [70]	single crystal	-	299	40.6
Yang [25]	100 nm	HfO_2/n-Si	293 - 373	35 - 66000
Hood [78]	160 nm	Al_2O_3(0001)	348 - 371	1000 - 16700
Ruzmetov [24]	100 nm	Si(001)	293	240
Yang [60]	100 nm	Ge(100)	293, 333	13.5, 7.9
Ko, unpublished	370 nm	Al(100)	293 - 328	4.5 - 920
Ko, unpublished	370 nm	Si(100)	293 - 333	4.5 - 16.2

In general, ε_V is frequency dependent, and since our IV curves were acquired by a DC measurement we do not consider the high frequency measurements reported by Yang [25] and Hood [78]. Ruzmetov's [24], Yang's [60], and Ko's measurements of ε_V were calculated using the Poole-Frenkel (PF) slope. By using the known temperature and measuring the PF slope, the dielectric constant was calculated. Measurements of ε_V grown on Si are

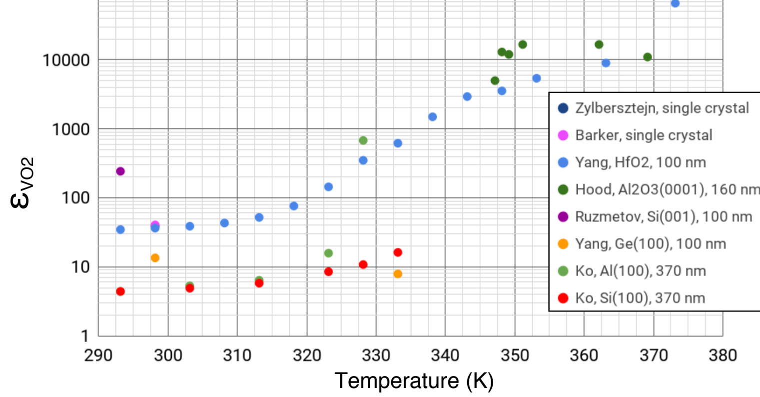

Figure 2.4: All measured dielectric constant data for VO_2 of varying thickness on various substrates. Notice the log scale of the y-axis. Citations in Table 2.1.

the most similar to our experiment and minimize the difference in the strain of the film.

Ruzmetov's measurement on Si was performed by an AFM tip on a 200 nm Au contact [24]. The PF slope is inversely proportional to T and ε_{V}, so if the temperature of the film was higher than assumed it would increase the calculated value of ε_{V}. Therefore, it may be possible that the film warmed during Ruzmetov's measurement, which artificially increased the measurement of ε_{V}. For Ko's measurement the temperature of the film is fixed by depositing large Pd pads in thermal equilibrium with the sample. Since smaller devices are more susceptible to heat dissipation due to surface-to-volume ratio thermal effects could play a role because of the smaller size of the contact in comparison with Ko's measurement. We use Ko's measurement of ε_{V} grown on Si, since it is the most similar to our film, and less susceptible to thermal effects than Ruzmetov's measurement.

We fit a functional form to the temperature dependent ε_{V} data to interpolate and extrapolate over the 293 K - 340 K range. An exponential dependence of the form

$$\varepsilon_{\mathrm{V}}(T[^{\circ}\mathrm{C}]) = a + b \cdot e^{T/c} \tag{2.2}$$

was found to fit the desired data range the closest, with fit parameters and

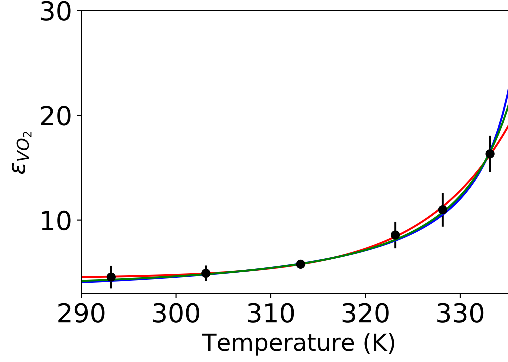

Figure 2.5: Different functional forms considered when fitting Ko's ε_{V} data. Red is the exponential form used (Eq. 2.2), blue and green fits are of the form in Eq. 2.4. The blue curve uses the measured transition temperature of our film $T_C = 339.5$ K, and the green curve fit the transition temperature to $T_C = 345$ K.

standard error of

$$\begin{aligned} a &= 4.44 \pm 0.12 \\ b &= 0.0176 \pm 0.0047 \\ c &= 9.22 \pm 0.37\ ^\circ\mathrm{C}. \end{aligned} \tag{2.3}$$

Although the shift from celsius to Kelvin is a well-defined linear shift, fitting to an exponential function in Kelvin produced a much larger relative error in the parameter b. The fit is performed in celsius to keep the relative error reasonable, then shifted to Kelvin when calculating the temperature of the film. When calculating the film temperature the input temperature must be in Kelvin for consistency with the fundamental constants in the PF slope.

We also considered a fit of the form

$$\varepsilon_{\mathrm{V}}(T) = a_1 + \frac{b_1}{(T_C - T)^{c_1}} \tag{2.4}$$

where T_C is the IMT temperature ($T_C = 339.5$ K for our film) and a_1, b_1, and c_1 are parameters to be fit. A second fit of the same form is considered where the IMT temperature, T_C is a fourth fit parameter.

Figure 2.5 shows the three fits considered, with the exponential fit shown in red (Eq. 2.2), and the two fits of the form in Eq. 2.4 is shown in blue and green. The blue curve is the three-parameter fit where the transition

temperature is assumed to be 339.5 K, the green curve is the four-parameter fit, with T_C fit to 345 K.

We find that the exponential form has the lowest rms error for Ko's data on Si. The exponential form was also found to fit all temperature dependent sets of ε_V data (Fig. 2.4) before the transition temperature. We use the exponential form (Eq. 2.2) since we are primarily using the fit to interpolate and extrapolate data over the range 293 K to 340 K, assuming the insulating state is not stable above 340 K.

2.3 *IV* Collection and Correction

With the AFM in contact mode, the ~~voltage bias~~ is ramped from 0 to 15 V and back, measuring the current at 0.05 V intervals at each point on a 256 × 256 grid over the 500 × 500 nm^2 image area. A typical *IV* curve is shown in Fig. 2.6, with the voltage ramp up shown in blue, and ramp down shown in red. At low voltages the film is in the insulating state, and at high voltages the film is in the metallic state. The IMT can be seen as the sudden increase in the measured current (decrease for voltage ramping down). At each point four consecutive sweeps are performed, and are found to be consistent with each other, ruling out sudden changes in film quality or contact resistance. Data from the second sweep is analyzed throughout this work. We use the data from ramping the voltage up to calculate the electric field and temperature.

In each raw *IV* curve there are two artifacts that must be addressed. The first is the presence of a current spike and subsequent exponential decay, both when ramping up and down, immediately following the IMT (Fig. 2.6). The large spike and decay is due to a stray capacitance (C) in the system, which we show does not affect the current through the film in the insulating state. The second is the presence of a large resistance in the metallic state, which occurs at voltages greater than the transition. In the metallic state we expect a negligible film resistance, but observe a non-negligible relationship between I and V. This non-negligible resistance does not arise from the VO_2 film, but it does have to be accounted for to precisely determine the voltage across the film.

First, we calculate the resistance of the film in the metallic state, then measure the effective resistance and decay time in the insulating and metallic state. We estimate the metallic state resistance of VO_2 to confirm it is much less than the measured resistance at high voltages. The metallic state

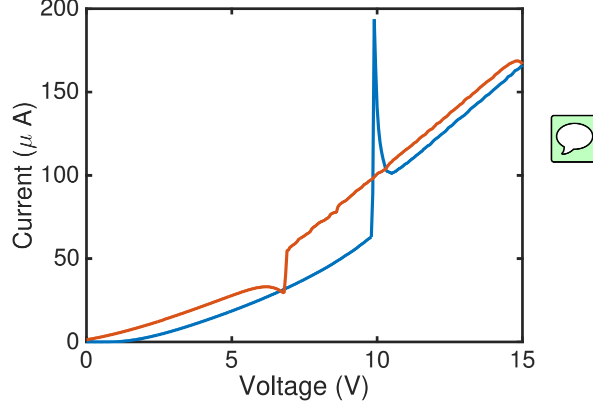

Figure 2.6: The raw data with the current spike in both the ramping up (blue) and down (red) data. The linear region at higher voltages ~~is~~ signals the film is in the metallic state. The slope in the metallic state is fit to calculate R_{ext}.

resistance of VO_2 is calculated using

$$R_{\text{film, met}} = \frac{d}{\sigma_{\text{metal}} \cdot A}, \tag{2.5}$$

where d is the thickness of the film, σ_{metal} is the metallic state conductivity, and A is the average area of a grain. We use the average area of a grain, assuming the conductivity and thermal conductivity are sufficiently large at the grain boundary such that the induced current or temperature does not diffuse into neighboring grains, thus only the grain in contact with the tip is in the metallic state. We make this assumption based on the observation of percolation of the IMT through separate grains [10]. We use the metallic state conductivity previously measured to be $\sigma_{\text{metal}} = 10^5\ \Omega^{-1}\ \text{m}^{-1}$ [29, 33]. Assuming a film thickness of 187 nm and grain diameter of 72 nm, these values give an upper bound estimate of the metallic state resistance as

$$R_{\text{film, met}} \approx \frac{1.87 \times 10^{-7}\ \text{m}}{10^5\ \Omega^{-1}\ \text{m}^{-1} \cdot 4 \times 10^{-15}\ \text{m}^2} \approx 470\ \Omega. \tag{2.6}$$

This calculated resistance is an upper bound, since we do not consider current leak into neighboring grains.

The linear relationship between I and V is identified as an effective resistance in both the insulating and metallic state. When ramping up (red line in Fig. 2.7 (a)) the average effective ~~total~~ resistance in the metallic state,

$R_{\text{eff, met}}$ is found to be 66 kΩ for the image. When the voltage is ramped down the average effective resistance in the insulating state, $R_{\text{eff, ins}}$, is measured to be 166 kΩ for the image (red line in Fig. 2.8 (a)). The effective resistance in the insulating state is used as a loose guide for what we expect for the VO_2 metallic state, since we expect the film to follow the PF conduction mechanism in the insulating state, not Ohmic conduction (See Section 2.4).

When ramping the voltage up (down) we observe a large current spike at the transition, which decays exponentially into the metallic (insulating) state. These spikes indicate a stray capacitance in our system, which discharges when the film undergoes the IMT. In both the metallic and insulating state we fit to the exponential decay and calculated a decay time, τ. Figs. 2.7 and 2.8 focus on the exponential decay in the *IV* curves in the ramping up and down data sets respectively. To fit the decay time the linear offset is subtracted off in both cases, and is indicated by the red line in panel (a) of both figures. Panel (b) shows the shifted exponential decay and corresponding fit, where the ramp rate of 500 V/s has been used to convert the x-axis from volts to seconds. Finding two different decay constant values is not surprising since the film resistance is changing between the two states, and $\tau = RC$.

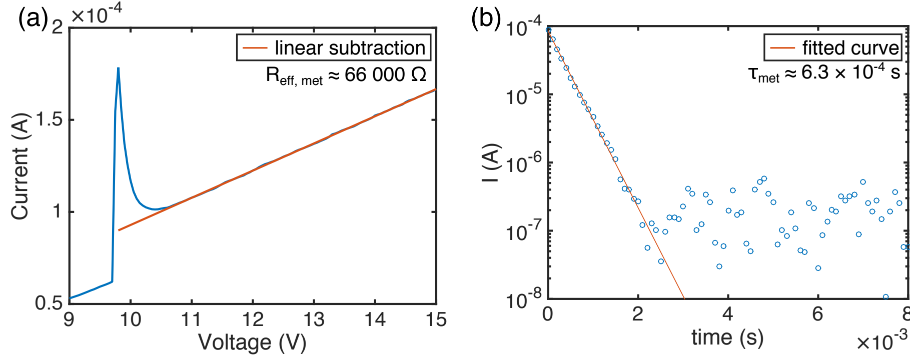

Figure 2.7: Exponential decay in the *IV* data when ramping up the applied voltage. (a) The capacitance spike in the data when the applied voltage is ramped up. The red line indicates the line that was subtracted from the data to leave the exponential decay. (b) The exponential decay data (blue) and fit (red) used to determine the decay constant τ.

We have so far measured the effective resistance and the decay time in both the insulating and metallic state, and calculated the metallic state

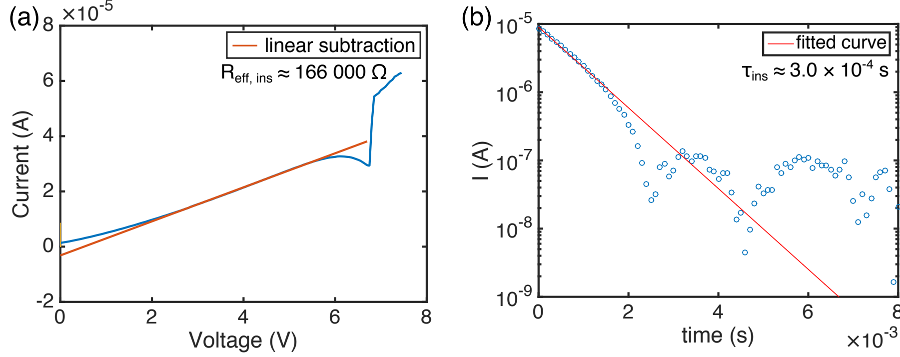

Figure 2.8: Exponential decay in the *IV* data when ramping down the applied voltage. (a) The capacitance spike in the data when the voltage is ramped down. The red line indicates the line that was subtracted from the data to leave the exponential decay. (b) The exponential decay data (blue) and fit (rted) used to determine the decay constant τ. Recall that the voltage is ramped down, so when converting to time the spike happens first, then the decay, as expected of the usual exponential decay.

resistance of the film. Table 2.2 summaries these measured values. The table also lists the unknown values that must be solved for.

Next, we must relate the measured time constant and effective resistances to the film resistance, external resistance, and stray capacitance. Because the tip-sample geometry is effectively a 2-probe *IV* measurement, we must correct for the external series resistance in the contacts and leads. We model the film as a simple resistor (R_{film}), and the additional resistance as a second external resistance (R_{ext}) in series with the film. We model the data collection by the CAFM as an effective circuit diagram, with the three models we consider shown in Fig. 2.9. The voltage correction will be different depending

	Insulating	Metallic
R_{eff}	166 000† Ω	66 000 Ω
τ	6.3×10^{-4} s	3.0×10^{-4} s
R_{film}	unknown	470 Ω
R_{ext}	unknown	
C	unknown	

Table 2.2: Measured or calculated values of the effective resistance and decay time in our data.

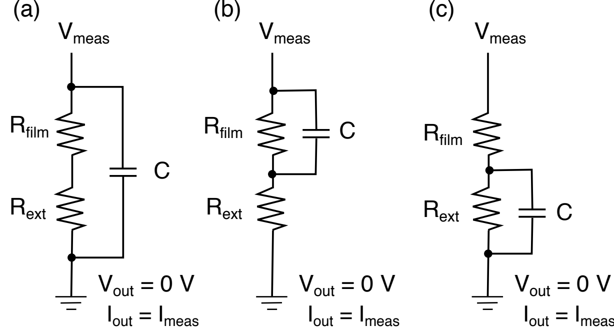

Figure 2.9: Possible effective circuit diagrams. (a) The stray capacitance in parallel with both the film and external resistance. (b) The stray capacitance in parallel with only the film resistance. (c) The stray capacitance in parallel with only the external resistance.

on the geometry of the effective circuit, so we first determine which of the three cases depicted in Fig. 2.9 produces the capacitance spike we observe in our data. In each case we simulate the circuit using approximate values to determine which configuration produces the capacitance spike we observe.

The Thevenin equivalent circuit will be used to determine the voltage and resistance that should be used when calculating the decay constant $\tau = R_{\mathrm{TH}}C$. Thevenin's Theorem state that any combination of batteries and resistances with two terminals can be replaced by a single voltage source, V_{TH} and a single series resistor R_{TH}. To calculate the Thevenin equivalent voltage one first identifies the load, in this case the capacitor, and calculates the open circuit voltage at the load terminals. The Thevenin resistance is V_{TH} divided by the current with the terminals short circuited.

Stray Capacitance parallel to both resistors

We first focus on the case where the capacitance is in parallel with both resistances (Fig. 2.9 (a)) is the simplest. The Thevenin voltage is the measured voltage, and the Thevenin resistance is the sum of the resistances in series,

$$R_{\mathrm{TH}} = R_{\mathrm{film}} + R_{\mathrm{ext}}, \tag{2.7}$$

in both the insulating and metallic state. Once the load capacitor is reinstated into the circuit, the time constant becomes $\tau = R_{\mathrm{TH}}C$ which we use to relate the measured decay time in the insulating and metallic state to the model resistances and capacitor.

	Insulating	Metallic
R_{eff}	166 000 Ω	66 000 Ω
τ	6.3 $\times 10^{-4}$ s	3.0 $\times 10^{-4}$ s
R_{film}	73 070 Ω	470 Ω
R_{ext}	65 530 Ω	
C	4.5 nF	

Table 2.3: Measured or calculated values of the effective resistance and decay time from our data (black), and the solved parameters from the case where the capacitor is in parallel with both the film and external resistance (blue). †equation and value not used to solve for parameters.

Taking into account the decay times in the insulating and metallic state gives 2 more equations. Putting these 3 equations together, we can solve for approximate average values of $R_{\text{film, ins}}$, R_{ext}, and C, which are filled in blue in Table 2.3.

$$\begin{aligned} R_{\text{eff, met}} &= 66000\ \Omega = (470\Omega + R_{\text{ext}}) \\ \tau_{\text{ins}} &= 6.3 \times 10^{-4}\ \text{s} = C \cdot (R_{\text{film, ins}} + R_{\text{ext}}) \\ \tau_{\text{met}} &= 3.0 \times 10^{-4}\ \text{s} = C \cdot (470\ \Omega + R_{\text{ext}}) \end{aligned} \tag{2.8}$$

We use LT Spice[2] to simulate this circuit, using the solved values and ramping the voltage at the same rate as the collected data (500 V/s in 0.05 V intervals), and instantaneously change the film resistance from its insulating state resistance to its metallic state resistance when the input voltage is 10 V. The simulated signal is shown in Fig. 2.10. From this figure we can see that this configuration does not produce a capacitance spike.

Stray capacitance in parallel with the film

The cases with the capacitance in parallel with one of the resistors (Fig. 2.9 (b) and (c)) have very similar Thevenin equivalent circuit calculations. The Thevenin voltage when the capacitor is in parallel with the film (external resistance) can be seen as the voltage through the film (external resistance). The Thevenin resistance in both cases is the film and external resistance added in parallel,

$$R_{\text{TH}} = \frac{R_{\text{film}} \cdot R_{\text{ext}}}{R_{\text{film}} + R_{\text{ext}}}. \tag{2.9}$$

[2] www.linear.com/ltspice

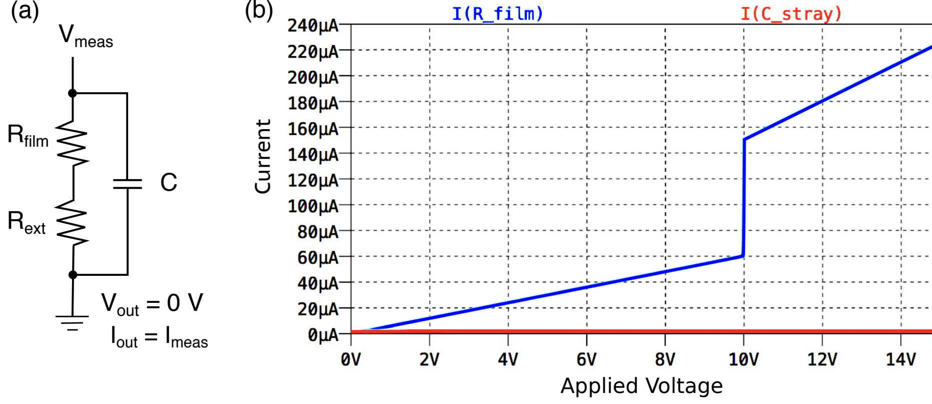

Figure 2.10: (a) Possible effective circuit diagram. (b) The simulated result of the circuit from (a), with values from Table 2.3. The measured current is the sum of the displayed measurements.

The time constant for both of these cases is $\tau = R_{\text{TH}}C$, which we use to relate the measured decay time in the insulating and metallic state to the model resistances and capacitor.

$$\begin{aligned}
R_{\text{eff, met}} &= 66000\ \Omega = R_{\text{ext}} + 470\ \Omega \\
\tau_{\text{ins}} &= 6.3 \times 10^{-4}\ \text{s} = C \cdot \frac{R_{\text{film, ins}} \cdot R_{\text{ext}}}{R_{\text{film, ins}} + R_{\text{ext}}} \\
\tau_{\text{met}} &= 3.0 \times 10^{-4}\ \text{s} = C \cdot \frac{470\ \Omega \cdot R_{\text{ext}}}{470\ \Omega + R_{\text{ext}}}
\end{aligned} \tag{2.10}$$

Solving these three equations for the 3 unknowns, finds an insulating state resistance of the film of approximately 1000 Ω, which is hardly insulating. In this case, we include the effective resistance in the insulating state, and allow the metallic state resistance of the film to vary. This is equivalent to adding a secondary external resistance in series with the film and parallel with the stray capacitor. Our new system of equations to solve is

$$\begin{aligned}
R_{\text{eff, ins}} &= 166000\ \Omega = R_{\text{film, ins}} + R_{\text{ext}} \\
R_{\text{eff, met}} &= 66000\ \Omega = R_{\text{film, met}} + R_{\text{ext}} \\
\tau_{\text{ins}} &= 6.3 \times 10^{-4}\ \text{s} = C \cdot \frac{R_{\text{film, ins}} \cdot R_{\text{ext}}}{R_{\text{film, ins}} + R_{\text{ext}}} \\
\tau_{\text{met}} &= 3.0 \times 10^{-4}\ \text{s} = C \cdot \frac{R_{\text{film, met}} \cdot R_{\text{ext}}}{R_{\text{film, met}} + R_{\text{ext}}}
\end{aligned} \tag{2.11}$$

	Insulating State	Metallic State
R_{eff}	166 000[†] Ω	66 000 Ω
τ	6.3 $\times 10^{-4}$ s	3.0 $\times 10^{-4}$ s
R_{film}	123 000 Ω	23 000 Ω
R_{ext}	43 000 Ω	
C	19.9 nF	

Table 2.4: Measured or calculated values of the effective resistance and decay time from our data (black), and the solved-for parameters from the case where the capacitor is in parallel with the film (blue). [†]Assumes the insulating state is a simple Ohm resistor, which we argue in the following section it is not.

We let the metallic state resistance of the film be a parameter to solve the system, the results of which are summarized in Table 2.4.

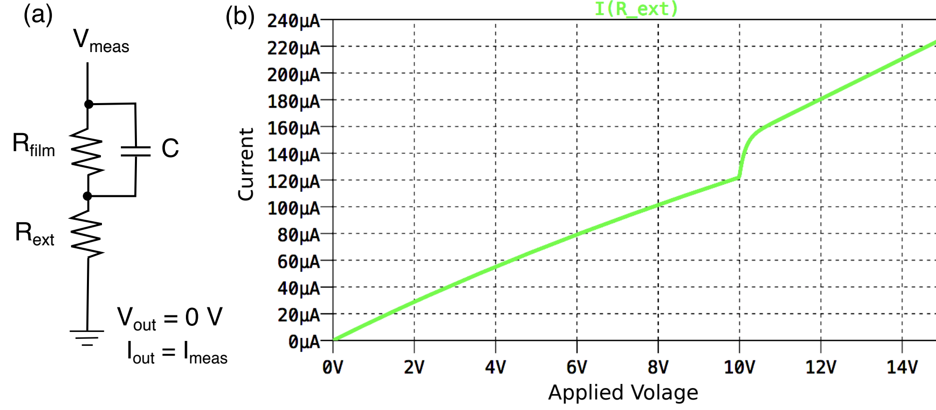

Figure 2.11: (a) Possible effective circuit diagram. (b) The simulated result of the circuit from (a), with values from Table 2.4. The measured current is the current through the external resistance.

Once again, we see that this configuration does not produce the measured signal, so we move to the final configuration.

Stray capacitance in parallel with the external resistance

For the decay time in this case, the Thevenin equivalent resistance is the same as the capacitor in parallel with the film, Eq. 2.9. Since the two cases are so similar, we expect an unphysical solution using three equations, so

	Insulating State	Metallic State
R_{eff}	166 000[†] Ω	66 000 Ω
τ	6.3 $\times 10^{-4}$ s	3.0 $\times 10^{-4}$ s
R_{film}	123 000 Ω	23 000 Ω
R_{ext}	43 000 Ω	
C	19.9 nF	

Table 2.5: Measured or calculated values of the effective resistance and decay time from our data (black), and the solved parameters from the case where the capacitor is in parallel with the external resistance (blue). [†]Assumes the insulating state is a simple Ohm resistor, which we argue in the following section it is not.

we once again solve the system of four equations and include the effective resistance in the insulting state.

$$
\begin{aligned}
R_{\text{eff, ins}} &= 166000\ \Omega = R_{\text{film, ins}} + R_{\text{ext}} \\
R_{\text{eff, met}} &= 66000\ \Omega = R_{\text{film, met}} + R_{\text{ext}} \\
\tau_{\text{ins}} &= 6.3 \times 10^{-4}\ \text{s} = C \cdot \frac{R_{\text{film, ins}} \cdot R_{\text{ext}}}{R_{\text{film, ins}} + R_{\text{ext}}} \\
\tau_{\text{met}} &= 3.0 \times 10^{-4}\ \text{s} = C \cdot \frac{R_{\text{film, met}} \cdot R_{\text{ext}}}{R_{\text{film, met}} + R_{\text{ext}}}
\end{aligned}
\tag{2.12}
$$

Of the three cases, however, only the configuration with the capacitance in parallel with the external resistance results in a capacitance spike and subsequent decay at the IMT. In this situation however, the magnitude of the metallic state resistance is orders of magnitude larger than the calculated value. A fourth configuration is then considered, where the external resistance is split between two external resistors in series, and the stray capacitance is in parallel with one (Fig. 2.13 (a)). Calling the part of the resistance that is in parallel with the capacitor R_{ext1}, and the remaining external resistance R_{ext2}, the Thevenin equivalent resistance is found by first adding the film resistance and R_{ext2} in series, then adding R_{ext1} in parallel,

$$
R_{\text{TH}} = \frac{(R_{\text{film}} + R_{\text{ext2}}) \cdot R_{\text{ext1}}}{R_{\text{film}} + R_{\text{ext2}} + R_{\text{ext1}}}. \tag{2.13}
$$

Physically, the resistance R_{ext1} could describe the resistance across a thin oxide layer between the film and substrate, which creates a capacitor. This

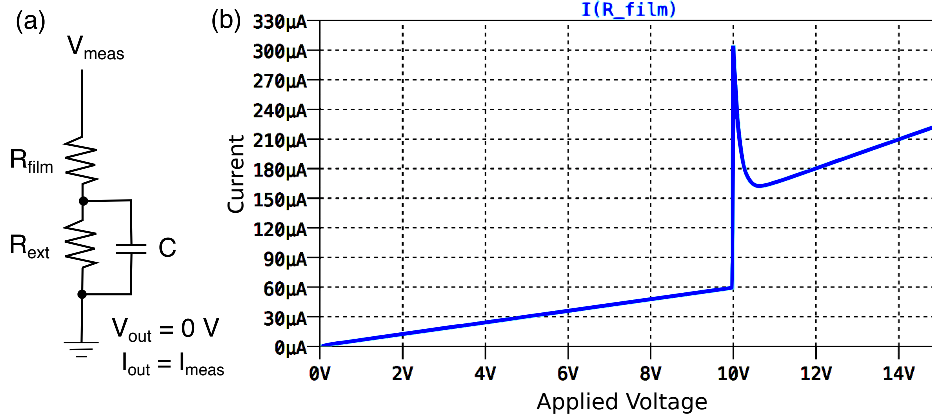

Figure 2.12: (a) Possible effective circuit diagram. (b) The simulated result of the circuit from (a), with values from Table 2.5. The measured current is the current through the film.

oxide would be very thin, which could account for the relatively high values of the stray capacitance calculated above. The resistance R_{ext2} can physically be anywhere in the circuit, provided it is in series with the film resistance. Specifically it could represent the contact resistance between the tip and the film surface.

$$\begin{aligned}
R_{\text{eff, ins}} &= 166000\ \Omega = R_{\text{film, ins}} + R_{\text{ext, 1}} + R_{\text{ext, 2}} \\
R_{\text{eff, met}} &= 66000\ \Omega = 470\ \Omega + R_{\text{ext, 1}} + R_{\text{ext, 2}} \\
\tau_{\text{ins}} &= 6.3 \times 10^{-4}\ \text{s} = C \cdot \frac{(R_{\text{film, ins}} + R_{\text{ext2}}) \cdot R_{\text{ext1}}}{R_{\text{film, ins}} + R_{\text{ext2}} + R_{\text{ext1}}} \\
\tau_{\text{met}} &= 3 \times 10^{-4}\ \text{s} = C \cdot \frac{(470\ \Omega + R_{\text{ext2}}) \cdot R_{\text{ext1}}}{470\ \Omega + R_{\text{ext2}} + R_{\text{ext1}}}
\end{aligned} \tag{2.14}$$

Now we solve for the 4 unknowns, $R_{\text{film, ins}}$, R_{ext1}, R_{ext2}, and C, finding similar numbers to the previous configuration, but we can constrain the film resistance in the metallic state. The values are reported in Table 2.6, and the LT Spice simulation is shown in Fig. 2.13 (b).

In Fig. 2.14, the current contributions from various elements have been explicitly plotted. The current through R_{film} and R_{ext2} are equal due to Kirchhoff's current law and are equal to the current measured by the AFM. Therefore, we do not need to correct the measured current, only the voltage.

One final check that is performed to justify this configuration is the

	Insulating State	Metallic State
R_{eff}	166 000† Ω	66 000 Ω
τ	6.3 $\times 10^{-4}$ s	3.0 $\times 10^{-4}$ s
R_{film}	100 500 Ω	470 Ω
R_{ext1}	42 600 Ω	
R_{ext2}	22 900 Ω	
C	19.9 nF	

Table 2.6: Measured or calculated values of the effective resistance and decay time from our data (black), and the solved parameters from the case where the capacitor is in parallel with some of the external resistance (blue). †Assumes the insulating state is a simple Ohm resistor, which we argue in the following section it is not.

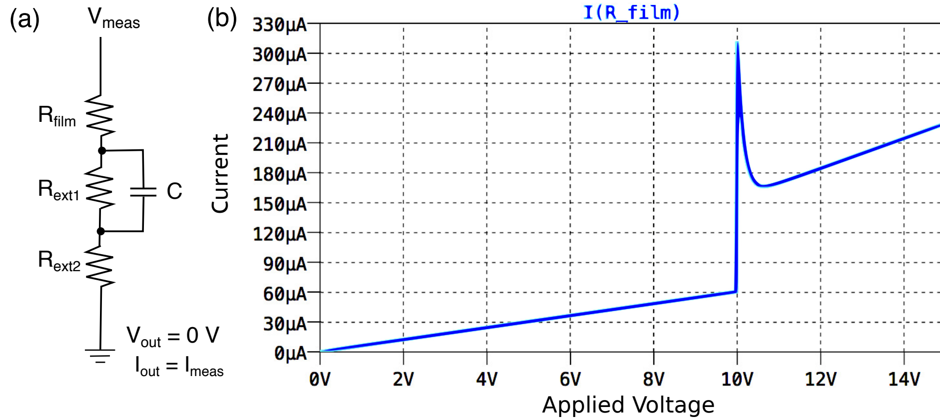

Figure 2.13: (a) Final effective circuit diagram where the capacitance is in parallel with only part of the external resistance. (b) The simulated result of the circuit from panel (a), using the values reported in Table 2.6.

simulation for when the voltage is ramped down. Using the same circuit as shown in Fig. 2.13 (a), but starting V_{meas} at 15 V and ramping to 0 V results in a similar order of magnitude spike and decay as we observe in the down case. The simulation is shown in Fig. 2.15.

Now that we have confirmed the effective circuit diagram and solved for the values, the voltage through the film can be determined in terms of the measured current and the current leak through the capacitor, I_C.

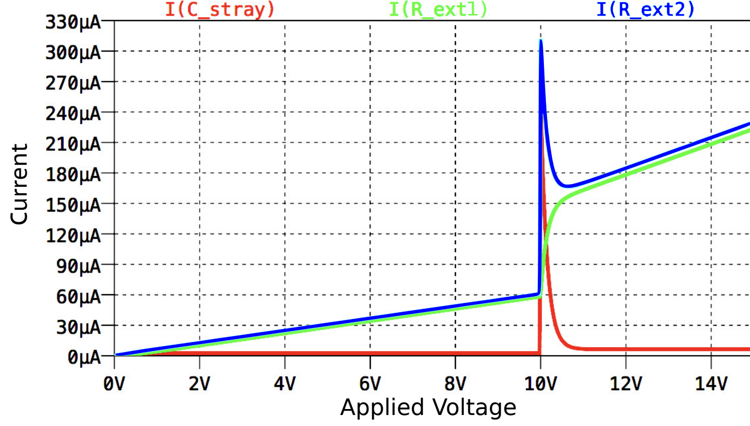

Figure 2.14: Final *IV* simulation output current, decomposed into signal from each component.

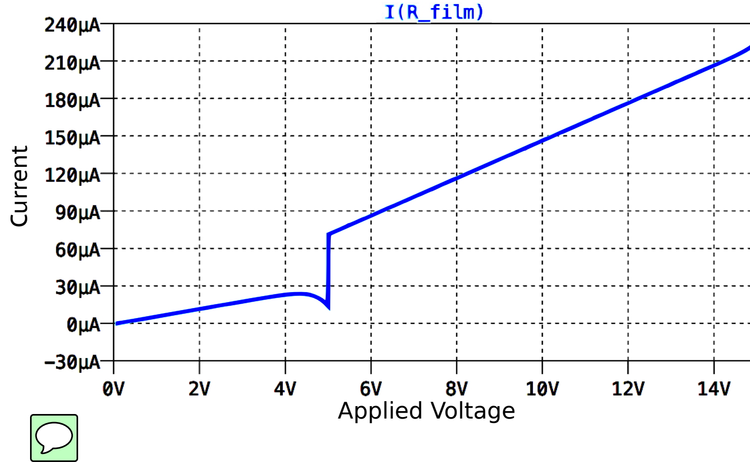

Figure 2.15: Final *IV* simulation output current, for voltage ramping down.

Kirchhoff's voltage law states

$$V_{\text{meas}} = I_{\text{meas}} \cdot R_{\text{film}} + I_{\text{meas}} \cdot R_{\text{ext, 2}} + (I_{\text{meas}} - I_C) \cdot R_{\text{ext, 1}}, \tag{2.15}$$

which we rearrange for the voltage through the film, $V_{\text{film}} = I_{\text{meas}} \cdot R_{\text{film}}$.

However, we first address to the assumption and resulting equation corresponding to treating the insulating state resistance as a simple Ohmic resistor. This simplification was adequate to produce a fourth equation to solve and to roughly model the system using LT Spice, however, we will not use it to explicitly solve for the circuit elements. Instead, we write the

voltage data correction in terms of metallic state resistance of the system which is the fit metallic state slope and the metallic state resistance of the film ~~which~~ we calculated using metallic state conductivity.

$$\begin{aligned} V_{\text{film}} &= V_{\text{meas}} - I_{\text{meas}}(R_{\text{ext, 1}} + R_{\text{ext, 2}}) + I_C \cdot R_{\text{ext, 1}} \\ &= V_{\text{meas}} - I_{\text{meas}}(R_{\text{eff, met}} - 470\ \Omega) + I_C \cdot R_{\text{ext, 1}}. \end{aligned} \tag{2.16}$$

Next, we use the 3 equations and 4 unknowns with the constraint that all resistances and capacitance values much be positive to find the upper and lower bound of the charge on the capacitor in the insulating state. Then, we quantify the magnitude of $I_C \cdot R_{\text{ext, 1}}$. Approximating realistic, yet high values for I_C and $R_{\text{ext, 1}}$,

$$\begin{aligned} V_{\text{film}} &\approx V_{\text{meas}} - 50\ \mu\text{A} \cdot 65500\ \Omega + 4\ \mu\text{A} \cdot 45000\ \Omega \\ &\approx V_{\text{meas}} - 3.4\ \text{V} + 0.18\ \text{V} \\ &\approx V_{\text{meas}} - 3.4\ \text{V} \cdot 95\% \\ &\approx V_{\text{meas}} - I_{\text{meas}}(R_{\text{eff, met}} - 470\ \Omega) \cdot 0.95. \end{aligned} \tag{2.17}$$

Furthermore, analysis of the circuit, circuit elements, and bounding the values of the circuit elements was performed by Jason Hoffman. The details of this analysis can be found in Appendix C. This analysis bounds $R_{\text{film}}^{\text{metal}}$ below ~ 22 kΩ, $R_{\text{ext, 1}}$ between 46 kΩ and 68 kΩ, which greatly reduces the total plausible solution space. The resulting insulting state resistance, $R_{\text{ext, 2}}$, and capacitance are solved over this range in Fig. C.5. The stray capacitance is found to be very large, on the order of 100 nF for larger $R_{\text{ext, 1}}$ values. Even though this region of the parameter space satisfies all conditions, it produces non-realistic values. For each solution the product $I_C \cdot R_{\text{ext, 1}}$ and $I_{\text{meas}}(R_{\text{eff, met}} - 470\ \Omega)$ are calculated (Fig. C.6) and the resulting percentage correction. A large fraction of the solution space has a correction factor less than 10%, so we use a 5% (or equivalently, 95% of $I_{\text{meas}}(R_{\text{eff, met}} - 470\ \Omega)$ correction factor as an average correction.

As a check, we perform our PF analysis and vary the percentage correction from 100% down to 50% (or a the ratio of $I_C \cdot R_{\text{ext, 1}}$ to $I_{\text{meas}}(R_{\text{eff, met}} - 470\ \Omega)$ from 0% to 50%) to calculate the resulting temperature. From the analysis in Appendix C, we would only expect a correction of 80% for plausible values of the circuit elements. Varying the correction down to a 90% correction factor, only chagnes the final temperature calculation by 1 K. We take this into account in the final reported temperature uncertainty.

To better describe the current in the insulating state and the IMT, a non-linear approximation of the film resistance could be considered. The

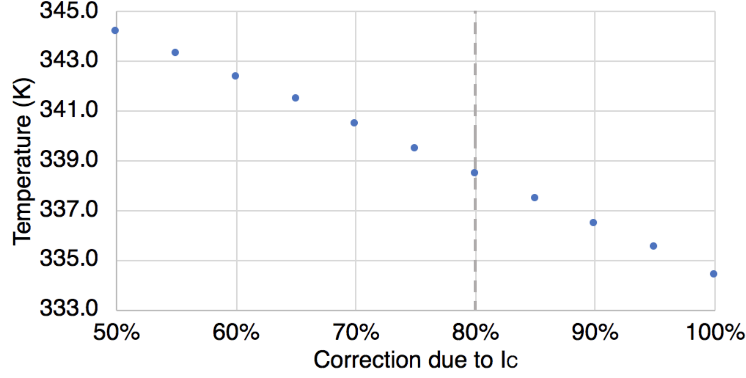

Figure 2.16: Final calculated temperature over a square in the middle of the image 100 × 100 pixels large, as a function of increased current through I_C. Only for percentages greater than 80% (marked with a dashed line), the correction percentage corresponds to a plausible solution to the 3 equations. A value of 95% is used throughout the analysis.

second check we perform is to account for the possibility of a larger metallic state resistance. Our PF analysis was rerun assuming the resistance of VO_2 in the metallic state is increased up to 20 000 Ω. The final temperature calculation is shown as the resistance of the metallic state of VO_2 is increased in Fig. 2.17. The temperature increases by 0.2 K when the metallic state resistance is increased by a factor of 10. We account for this variation in the final reported temperature uncertainty.

Finally, we look to map these resistances onto physical components in the CAFM. We are not sure of the composition of the interfacial layer between the Si substrate and the VO_2 film, but we assume it is between Si and SiO_2. We estimate the lower bound through the SiO_x interfacial layer by assuming the resistivity is closest to that of Si, $\sim$ 3200 Ωm, using the interface layer thickness of 2 nm, and grain contact area of 4 $\times 10^{-15}$ m^2,

$$\begin{aligned} R_{\text{interface}} &= \rho_{\text{Si}} \cdot d/A \\ &= (3200\ \Omega\text{m}) \cdot (2 \times 10^{-9}\ \text{m})/(4 \times 10^{-15}\ \text{m}^2) \\ &\approx 1.6 \times 10^{9}\ \Omega. \end{aligned} \tag{2.18}$$

Similarly we estimate the capacitance using the dielectric constant of SiO,

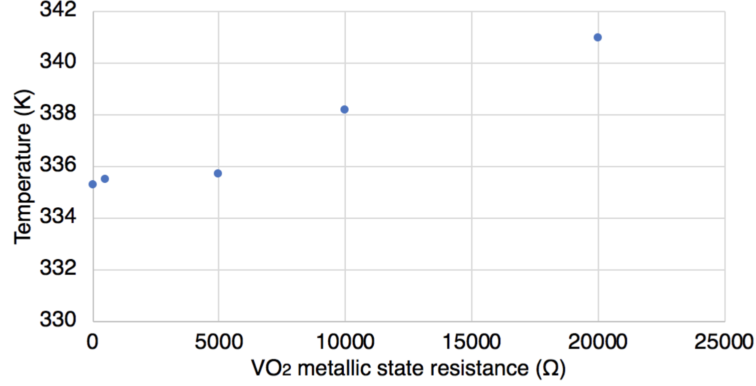

Figure 2.17: Final calculated temperature over a square in the middle of the image 100 × 100 pixels large, as a function of increased metallic state resistance of VO_2. A value of 470 Ω is used throughout the analysis.

$\epsilon_{\text{SiO}} = 5.5$ [79],

$$\begin{aligned} C_{\text{interface}} &= \epsilon_{\text{SiO}}\epsilon_0 A/d \\ &= (5.5)\cdot(8.85\times10^{-12}\ \text{F/m})\cdot(4\times10^{-15}\ \text{m}^2)/(2\times10^{-9}\ \text{m}) \\ &\approx 10^{-16}\ \text{F}. \end{aligned} \tag{2.19}$$

Both of these values are off by orders of magnitude; 5 orders of magnitude too large in the case of resistance, and 8 orders of magnitude too small in the case of capacitance. One way to reconcile the large difference between the calculated and measured R and C is to look at the ratio A/d. The area to thickness ratio is present in both calculations, and seems to be too small by 8 orders of magnitude. Instead, we work backwards and consider a larger effective area. Starting with the calculated stray capacitance, we estimate the effective area

$$\begin{aligned} A &= C\cdot d/(\epsilon_{\text{SiO}}\epsilon_0) \\ &= 1.9\times10^{-8}\text{F}\cdot 2\times10^{-9}\text{m}/(5.5\cdot 8.85\times10^{-9}\ \text{F/m}) \\ &\approx 7.8\times10^{-7}\ \text{m}^2. \end{aligned} \tag{2.20}$$

An effective area of 7.8 $\times10^{-7}$ m^2 corresponds either to a circle of radium 500 μm, or a square of side length 880 μm. Again working backwards, we

use this area to calculate the resistivity of the SiO_x layer,

$$\begin{aligned} \rho_{\mathrm{SiO_x}} &= R_{\mathrm{ext1}} \cdot A/d \\ &= 44100\ \Omega \cdot 7.8 \times 10^{-7}\mathrm{m}^2/2 \times 10^{-9}\mathrm{m} \\ &\approx 1.7 \times 10^{7}\ \Omega\mathrm{m}. \end{aligned} \tag{2.21}$$

This resistivity is within the range of reasonable resistivity values of the interface layer, since $\rho_{\mathrm{Si}} = 3200\ \Omega$m, and good SiO_2 has resistivity $\rho_{\mathrm{SiO_2}} \approx 10^{15}\ \Omega$m

We have determined the effective circuit diagram for our data, and identified it with a leaky SiO_x layer in between the film and substrate. Yang and Hu model a leaky gate dielectric in the same manner as we have, with a resistor and capacitor in parallel, and a second resistor in series [80]. The resistor in parallel represents the effective device resistance due to leakage through the oxide, and the resistor in series represents any series resistance, such as that through the substrate and gate itself.

2.4 Conduction Mechanisms in Insulators

To determine which conduction mechanism dominates our VO_2 film, we review all conduction mechanisms in insulators [45]. Table 2.4 summarizes these mechanisms, with the current I and voltage V dependence, and typical electric field ($\mathbf{E}$) and temperature ranges where each mechanism is applicable. The table also includes the film properties that must be known or measured in order to accurately calculate the temperature.

Table 2.7: Summary of conduction mechanisms in insulators [45]. Additional sources cited individually.

Mechanism	Limited	I and V linearized form	Required properties	Typical **E**	Typical T
Schottky Emission [81]	Electrode	$\ln(I) = \frac{e^{3/2}}{(4\pi\varepsilon_0\varepsilon_\mathrm{i} d)^{1/2} k_B T} V^{1/2} + C$	ε_i, d	$\mathbf{E} \lesssim 500$ MV/m	T $\gtrsim 400$ K
Fowler-Nordheim Tunneling [81, 82]	Electrode	$\ln\left(\frac{I}{V^2}\right) = \frac{-8\pi(2em^*)^{1/2}\phi_\mathrm{B}^{3/2} d}{3h}\frac{1}{V} + C$	m^*, ϕ_B, d	$\mathbf{E} \gtrsim 100$ MV/m, $d \lesssim 10$ nm	T $\lesssim 100$ K
Thermionic-Field Emission [81]	Electrode	$\ln\left(\frac{I}{V}\right) = \frac{\hbar^2 e^2}{24m^* d^2 (k_B T)^3} V^2 + C$	m^*, d	$\mathbf{E} \lesssim 500$ MV/m	T $\lesssim 2000$ K
Direct Tunneling [82, 83]	Electrode	$I = -\frac{ae^2}{2\pi h d^2} V \exp\left(\frac{-4\pi(2em^*\phi_B)^{1/2} d}{h}\right)$	m^*, ϕ_B, d	$\mathbf{E} \lesssim 100$ MV/m, $d \lesssim 10$ nm	T $\lesssim 100$ K
Poole-Frenkel Conduction [25, 84]	Bulk	$\ln\left(\frac{I}{V}\right) = \frac{e^{3/2}}{(\pi\varepsilon_0\varepsilon_\mathrm{i} d)^{1/2} k_B T} V^{1/2} + C$	ε_i, d	$\mathbf{E} \gtrsim 15$ MV/m	100 K - 400 K
Hopping Conduction [85]	Bulk	$\ln(I) = \frac{er}{dk_B T} V + C$	r, d	$\mathbf{E} \lesssim 50$ MV/m	$\lesssim 300$ K
Ohmic Conduction	Bulk	$I = \frac{ae\mu n}{d} V \exp\left(\frac{-E_\mathrm{g}}{2k_B T}\right)$	E_g	$\mathbf{E} \lesssim 10$ MV/m	200 K - 500 K
Space Charge-Limited Conduction	Bulk	$I = \frac{9a\mu\varepsilon_\mathrm{i}\theta}{8d^3} V^2$	μ, d	$\mathbf{E} \gtrsim 10$ MV/m	200 K - 500 K
Ionic Conduction [86]	Bulk	$\ln(I) = \frac{er_\mathrm{i}}{2dk_B T} V + C$	r_i, d	T dependent†	T $\gtrsim 500$ K

†Strongly temperature and material dependent.

Table 2.8: List of variables in conduction mechanisms.

Variable	Definiton
e	electron charge
ε_0	free space dielectric constant
ε_i	dielectric constant of the insulator
d	film thickness
m^*	effective electron mass
ϕ_B	barrier height
a	tip contact area
r	carrier hopping distance, distance between traps
μ	electron mobility
n	density of states (in the conduction band)
E_g	(band) energy gap
θ	ratio of free-carrier density to the total (free plus trapped) carrier density
r_i	ion hopping distance

We linearize one representative voltage-corrected IV curve before the transition for each mechanism, and each are plotted in Fig. 2.19 to determine the dominant mechanism.

We know we fit our IV data in the insulating regime, so the temperature must be between room temperature and the IMT temperature, giving a range of 293 K - 340 K. We calculate the electric field at the IMT by finding the voltage at the transition and dividing by film thickness, giving a maximum electric field magnitude around 35 MV/m (Sect. 3.1). For the mechanisms, the order of magnitude of the electric field and temperature of our film are within reason of the ranges given.

We immediately dismiss some mechanisms by looking at the linearized plots. Ohmic behavior is the usual metallic conduction, which we observe in the metallic state, so we don't expect VO_2 to follow the ohmic behavior in the insulating state. Space charge-limited conduction occurs when the injected carrier density is greater than the thermally excited carrier density in an Ohmic material, which follows an $I \propto V^2$ dependence. Since we do not observe Ohmic conduction in the insulating state, we do not expect to observe the space charge-limited conduction [87]. Furthermore, from both of the linearized plots (Fig. 2.19 (g) and (h)) we see that neither exhibits a linear dependence. Ionic conduction, in general, is only observed at high temperature. Additionally the mechanism would destroy the crystal lattice by moving the ions, which we do not observe between four sweeps.

Fig. 2.18 shows the remaining conduction mechanisms in terms of energy band diagrams. The angle of the potential barrier of the insulator represents applied field strength. Vertical arrows correspond to thermal excitation. Notice for the electrode limited mechanisms the carrier originates in the electrode and is conducted through the insulator to the semi-conducting or

conducting substrate, where as in the bulk limited cases, PF and hopping, the carrier is excited from a trap in the material.

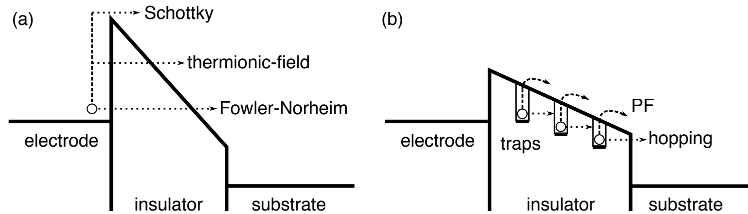

Figure 2.18: Energy band diagram of (a) Schottky emission, thermionic-field emission, and Fowler-Nordheim emission, and (b) PF and hopping conduction.

For the electrode limited mechanisms shown, high fields are required, and is demonstrated by a steep slope of the insulator band. Schottky emission is characterized by the thermal excitation of the carrier to overcome the electrode-insulator barrier height, Fowler-Nordheim occurs at lower temperatures where the carrier tunnels through the insulator, and thermionic-field is a combination of thermal excitation and tunneling through the insulator. Direct tunneling, not shown, occurs in low fields where the entire width of the insulator is seen as a barrier by the carrier. Given the average thickness of our film (187 nm), we can immediately rule out the carrier tunneling through our film. In particular, Fowler-Norheim tunneling and direct tunneling are not dominating our film.

The difference between PF and hopping conduction is similar to that of Schottky and Fowler-Nordheim. In the PF mechanism the carriers are thermally excited out of traps, and trap height is reduced by an applied field, and in hopping the carriers tunnel from trap to trap.

Electrode limited mechanisms depend on the electrode - semiconductor interface, in this case the gold coated tip in contact with the VO_2 film. The Schottky-Mott rule for barrier height is the difference between the metal work function and the semiconductor vacuum ionization energy. These values have been measured to be 5.30 eV for gold deposited at 50 °C and 5.15 eV for insulating VO_2 respectively, resulting in a barrier height of 0.15 eV [88]. The Schottky-Mott rule is not found to be an accurate prediction of the barrier in all metal-insulator interfaces due to a phenomenon known as Fermi level pinning. Fermi level pinning describes how the conduction band of the semiconductor bends at an interface independent of the metal with which it is in contact. Importantly, it removes the work function dependence

of that barrier height, instead stating that the barrier energy is constant and simply equal to one half of the semiconductor band gap. In VO_2 the band gap is $\approx$ 0.7 eV, giving a barrier height of about 0.35 eV [16].

The thermal energy, $k_B T$, at 340 K is $\sim$ 0.03 eV, an order of magnitude lower then the barrier height. Even though Schottky emission describes the thermal excitation of carriers, high fields can reduce the barrier height. The current density for Schottky emission is described as

$$J = A^* T^2 \exp\left[\frac{\sqrt{e^3|\boldsymbol{E}|}}{\sqrt{4\pi\epsilon_0\epsilon_\mathrm{i}}k_B T} - \frac{e\phi_\mathrm{B}}{k_B T}\right], \tag{2.22}$$

where the first term in the exponent describes how the barrier is lowered by an applied field, and all variables are defined in Table 2.8. Using our applied field of $\sim$ 35 MV/m, the barrier is lowered by $\sqrt{e^3|\boldsymbol{E}|/4\pi\epsilon_0\epsilon_\mathrm{i}} = 0.05$ eV. Even with the tip-sample potential barrier lowered by the applied field, the thermal energy is not sufficient for Schottky emission in VO_2.

Thermionic-field emission is generally seen at higher fields than Schottky emission at comparable temperatures. Petrin calculated the current density dependence for the three types of emission: Schottky, field, and thermionic-field emission at 300 K [89]. For a barrier height comparable to VO_2 close to room temperature thermionic-field only dominates between 180 MV/m and 320 MV/m, which is an order of magnitude larger than our applied field. We conclude that thermionic-field emission does not dominate our VO_2 film.

PF conduction and hopping conduction are the only remaining mechanisms that are applicable in our electric field and temperature range. Looking at the linearized plots (Fig. 2.19), both PF (e) and hopping (f) appear to have a linear region at the higher applied voltage just before the transition.

The current density due to the hopping conduction mechanism is described by

$$\mathbf{J} = ern_C\nu \exp\left(\frac{er|\mathbf{E}| - E_\mathrm{a}}{k_B T}\right) \tag{2.23}$$

where e is the electric charge, r is the hopping distance, n_C is the concentration of carriers, ν is frequency of thermal vibrations, and E_a is the activation energy. We fit the hopping mechanism by plotting $\ln I$ as a function of V. In a hopping-dominated material the slope of the linear fit would be equal to $er/(dk_B T)$. VO_2 has not been demonstrated to follow the hopping mechanism, and the hopping distance, r, has not been reported. Since both r and T are unknown, it is challenging to accurately calculate the temperature of the film. However, we can check for consistency by fitting the IV curve and assuming reasonable values for the hopping distance or temperature. When

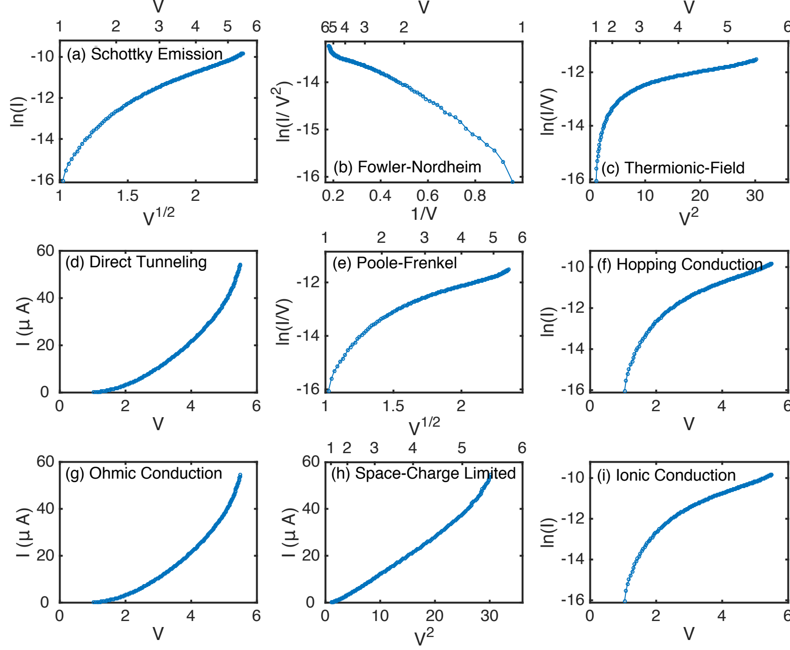

Figure 2.19: A typical IV curve from the data analyzed in this thesis, linearized for each of the conduction mechanisms in insulators. Where the scale has been altered, the true voltage scale is shown on the top axis. Current is displayed in A, and voltage in V unless otherwise indicated. (a) Schottky Emission. (b) Fowler-Nordheim Tunneling. (c) Thermionic-Field Emission. (d) Direct Tunneling. (e) Poole-Frenkel Emission. (f) Hopping Conduction. (g) Ohmic Conduction. (h) Space Charge-Limited Conduction. (i) Ionic Conduction.

the hopping distance is fixed at a reasonable length, in the 0.1 - 3 nm range [84], the temperature is well below room temperature which we know is not accurate. Fixing the temperature in the range 293 K - 340 K results in a hopping distance on the order of tens of nanometers. We conclude that our film is not dominated by the hopping mechanism because it predicts unreasonable film properties.

Taking into consideration the electric field and temperature ranges, and comparing the linearized plots, we conclude that PF emission is the dominant conduction mechanism in our VO_2 film, in agreement with literature [21, 25].

PF conduction is when high fields and temperatures excite carriers out of

traps into the conduction band. Poole first described the effects of thermal excitations on trapped carriers, $\sigma = \sigma_0 e^{\alpha|\mathbf{E}|}$ and in 1938 Frenkel incorporated the effect of high electric fields, describing how high fields lower the effective trap height, and therefore lower the thermal energy required for trapped carriers to become excited into the conduction band [44].

The potential of a trap is lowered by $\Delta U = e|\mathbf{E}|r_0 + \frac{e^2}{4\pi\epsilon_0\epsilon_\text{i} r_0}$, the energy from the applied field and the coulomb interaction with the trap, where r_0 is the distance to the maximum from the trap. The maximum potential occurs when the two contributions are equal, $e|\mathbf{E}|r_0 = \frac{e^2}{4\pi\epsilon_0\epsilon_\text{i} r_0}$, giving $r_0 = \left(\frac{e}{4\pi\epsilon_0\epsilon_\text{i}|\mathbf{E}|}\right)^{1/2}$. Thus the potential energy of the trap is lowered by

$$\Delta U = 2e|\mathbf{E}|r_0 = \frac{e^{3/2}|\mathbf{E}|^{1/2}}{(\pi\epsilon_0\epsilon_\text{i})^{1/2}}. \tag{2.24}$$

Using the thermal ionization probability equation, $\exp[-(E_\text{a} - \Delta U)/k_B T]$, where E_a is the activation energy of the trap, the PF conductivity is written as

$$\sigma = \sigma_0 \exp\left[\frac{e^{3/2}E^{1/2}}{(\pi\epsilon_0\epsilon_\text{i})^{1/2}k_B T} - \frac{E_\text{a}}{k_B T}\right], \tag{2.25}$$

and the PF current density is

$$\mathbf{J} = \sigma_0 \mathbf{E} \exp\left[\frac{e^{3/2}E^{1/2}}{(\pi\epsilon_0\epsilon_\text{i})^{1/2}k_B T} - \frac{E_\text{a}}{k_B T}\right]. \tag{2.26}$$

Thus we see that the IV linearized form of the PF mechanism for VO_2 is

$$\ln\left(\frac{I}{V}\right) = \frac{e^{3/2}}{(\pi\varepsilon_0\varepsilon_\text{V} d)^{1/2}k_B T}V^{1/2} + C \tag{2.27}$$

Where ϵ_V is the temperature dependent dielectric constant of VO_2 from Eq. 2.2. We plot $\ln(I/V)$ as a function of $V^{1/2}$, and fit to the linear region immediately preceding the transition. We define the linear relationship between $\ln(I/V)$ and $V^{1/2}$ as P,

$$P \equiv \frac{e^{3/2}}{(\pi\varepsilon_0\varepsilon_\text{V} d)^{1/2}k_B T}. \tag{2.28}$$

2.5 A Second Data Set

Two separate maps of *IV* curves and topography were collected on the same VO_2 film. The data set we have been discussing up until this point we will refer to as dataset B. This is the data used for electric field and temperature analysis. Another smaller dataset, hereafter referred to as dataset A, was acquired before dataset B. Here we discuss dataset A only briefly, and argue that it has several crucial flaws, before returning to conduct the remainder of our analysis on the more complete dataset B.

The *IV* curves for data set B were collected on a 256 $\times$ 256 grid over a 500 $\times$ 500 nm^2 region.

Data set A was over a 1 $\times$ 1 μm^2 region, splitting the image into a 64 $\times$ 64 grid, and collecting *IV* curves at each point at a ramp rate of 95 V/s. The first problem was the topography showed signs of drift during measurement. The tip had not completely settled, and continued to move during the start of the measurement. Although this drift would not affect the *IV* measurements, the topography appears stretched along the left and top of the image. The second issue was that voltage bias was only ramped up to 12 V, and approximately a third of the pixels in the center of the image did not transition, leaving our analysis difficult. In our analysis we must calculate the voltage across the film, where we use the post-transition resistance to subtract off the external resistance. With little to no data points in the metallic state we could not get accurate fits to correct the data.

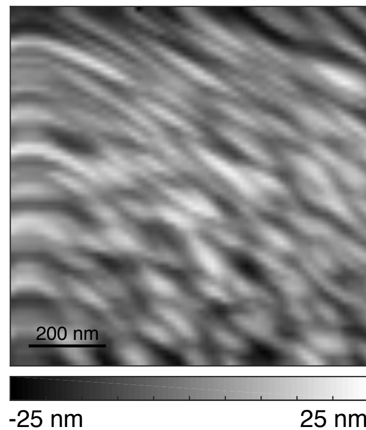

Figure 2.20: Topography from the dataset A.

A typical *IV* curve with sufficient data in the metallic state from dataset

A is shown in Fig. 2.21. *IV* curves from this data set do not show the capacitance spike at the transition. We also note the much more narrow hysteresis in this *IV* curve. If we consider the transition to be due to thermal effects, then because these *IV* curves were collected at the slower ramp rate the film has more time to cool while ramping down, and therefore would transition to the insulating state sooner than observed in data set B (Fig. 2.6).

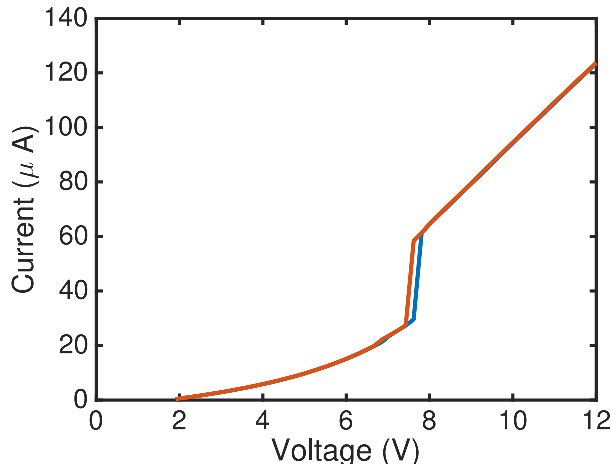

Figure 2.21: A typical *IV* curve from the first data set for the applied voltage ramping up (blue) and down (red).

We attempted to perform the same PF analysis on dataset A. However, after attempting to linearize dataset A in the aforementioned conduction mechanisms it became clear it behaved fundamentally different than data set B (Fig. 2.22). Similar to data set B, all mechanisms except for PF and hopping conduction can be eliminated based on electric field and temperature ranges. Also similar to data set B we considered the hopping mechanism, but this fitting produced either an unreasonable hopping distance or an unreasonable temperature.

Unlike data set B however, the PF dependence does not appear linear. All mechanisms with explicit T dependence are inversely proportional to T when the *IV* curves are linearized. So all curves must, at the very least, flatten out indicating a constant or increasing T, which we do not observe for the PF conduction mechanism (Fig. 2.22 (e)). The slightly concave quadratic behavior seen in dataset A would imply that as the bias is increased, the PF slope increases, corresponding to a decreasing temperature, which is not

physically reasonable.

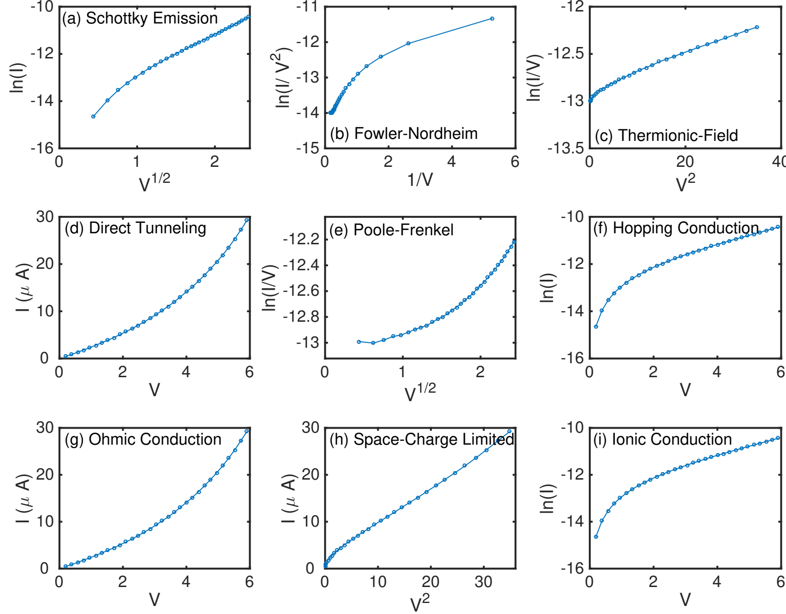

Figure 2.22: A typical IV curve from the first data set, linearized for each of the conduction mechanisms in insulators. Current is displayed in A, and voltage in V unless otherwise indicated. (a) Schottky Emission. (b) Fowler-Nordheim Tunneling. (c) Thermionic-Field Emission. (d) Direct Tunneling. (e) Poole-Frenkel Emission. (f) Hopping Conduction. (g) Ohmic Conduction. (h) Space Charge-Limited Conduction. (i) Ionic Conduction.

Because of the spatial drift, the lack of transition in a third of the field of view, and the unknown dominant conduction mechanism a second data set was collected, data set B. For the second data set there was no spatial drift, and the voltage was ramped to 15 V resulting in all pixels transitioning. When collecting IV curves, the ramp rate for the voltage bias was increased in order to reduce any thermal relaxation in the VO_2 between measurements. In doing so, the second data set is found to follow the PF mechanism. Due to the 5x higher voltage ramp rate in dataset B, the stray capacitance produced a large current spike and subsequent decay at the transition. As discussed in Sect. 2.3.2, we were able to account for the stray capacitance (Sect. 2.3), and proceed with the temperature calculation.

Chapter 3

Analysis

3.1 Electric field

For each IV curve on the map, we find the voltage at which the current jumps. The voltage through the film at the transition, and the local film thickness are used to calculate the applied field across the film at the transition. The local field at the transition for each point on the image is shown in Fig. 3.1 (a) with histogram and color bar for the map in (b). The histogram shows a narrow range of electric fields at the transition, which indicates that by applying a voltage bias we are causing the transition. We find an average applied electric field at the transition of 32 MV/m $\pm$ 3 MV/m, consistent with previous reports of an electric-field driven transition [21, 24, 27].

Fig. 3.1 shows that the electric field values for the top two thirds of the image are smaller than those required at the bottom third of the image. This behavior is also observed in the voltage and the current at the transition, so we are confident it is not due to a changing VO_2 film thickness as shown in Fig. A.1, in Appendix A where we consider the energy input by the tip to cause the transition, and conclude that an increase in thickness of the interfacial SiO_x layer on the order of 1 nm could plausibly leak sufficient heat to increase the required energy to warm the film. The increase in energy flow through the SiO_x layer could consequently cause an increase in the required voltage to cause the transition and resultant current at the transition.

Comparing the electric field at the transition with the topography of the film, we can distinguish individual grains in the electric field map. The electric field at the transition shows little variation within each grain, but grain edges require a higher applied electric field to transition. Higher required field could be due to variations within the film, either a change in V-O stoichiometry or strain, or could be the consequence of the tip being in contact with multiple grains at once. We can rule out changes in tip-sample resistance since we correct for the external resistance when correcting for the voltage through the film.

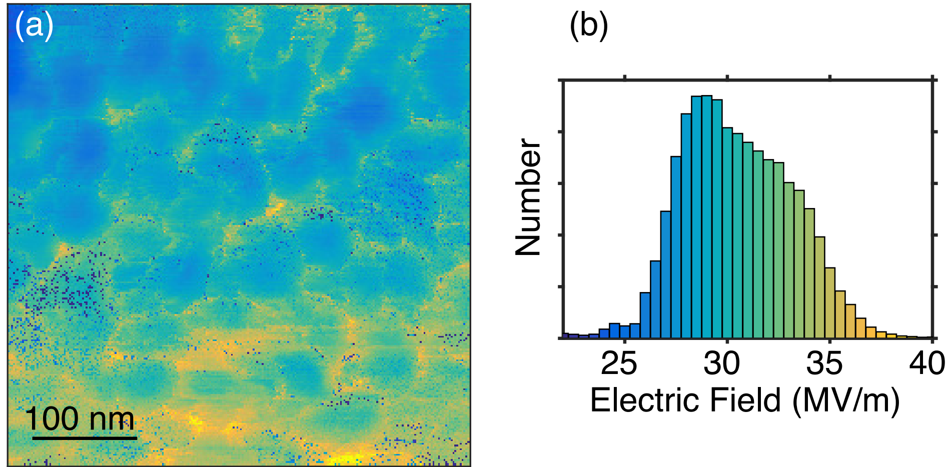

Figure 3.1: (a) Map of the electric field at the IMT. (b) Histogram of the electric field values at the transition. The color corresponds to the color bar for the map in (a).

3.2 Poole-Frenkel Fitting

When fitting the PF slope, first the inflection point is found by taking two numerical derivatives and finding the minimum value. We vary both endpoints around the inflection point, including at least 10 points on each side, and fit PF slope for numerous ranges, while keeping the overall linear fit root-mean-square (rms) error below a pre-defined value. We then choose the fit range with the lowest PF slope. Since the temperature is inversely proportional to the slope, the procedure of minimizing the slope finds the maximum pre-transition temperature. Fig. 3.3 shows a representative IV curve, with the numerical inflection point marked with a red star and the minimized PF slope found through this method is shown as a yellow line. The method of minimizing the slope is done for each IV curve in the 2-D map, and Fig. 3.2 shows the resultant PF slope at each point, along with a histogram of the values.

The fit shown in Fig. 3.3 is counter intuitive in two ways. First, we are minimizing the slope, and yet the fit is not centered at the inflection point, which is presumably the point of the curve that has the most shallow slope. Second, more than 21 points are used in the fit slope, which seems like it would only increase the value of the slope.

Addressing the first concern, we notice that the IV curve is asymmetri-

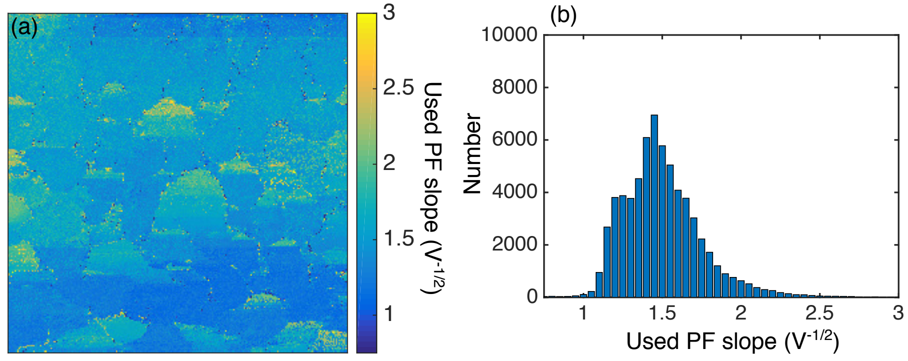

Figure 3.2: (a) The PF slope found by allowing both endpoints to vary and minimizing the slope. (b) The corresponding histogram.

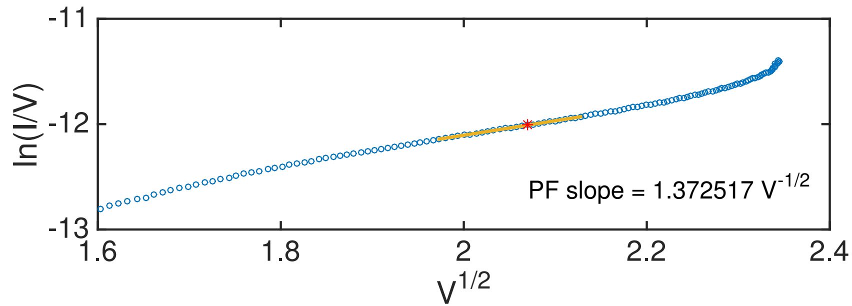

Figure 3.3: A representative PF linearized IV curve with the minimized PF fit. The red star marks the numerical inflection and the yellow line indicated the fit minimum PF slope.

cal, and consequently that the inflection is not necessarily the center of the most linear region. Looking at the same data as Fig. 3.3, the asymmetry is emphasized in Fig. 3.4, where a fixed fit region of 21 data points was moved along the IV curve, with the center point marked in black for the various fits. The corresponding PF slope (b), and rms error (c) is also shown for each fit. We can justify fitting close to, but not necessarily centered at the inflection point by looking at the PF slope and rms error of these fits. When fitting the PF slope we select the smallest slope to maximize the temperature since this slope still results in a low rms error, even if it is not the lowest. From panel (c) we see that the IV curve is the most linear in the vicinity of the inflection point, but not necessarily centered exactly at the inflection point.

Furthermore we notice from panel (b) that near the inflection point the center of the fit has very little affect on the PF slope, however as the fit range approaches the transition the PF slope greatly increases, and soon doubles in magnitude from $\sim 1.5\ V^{-1/2}$ near the inflection, increasing up to $> 3\ V^{-1/2}$. The upturn near the transition may be due to a the film not being dominated by the PF mechanism at the onset of the transition.

To see why more than 21 data points are included in the fit, we look at the fit produced from each region considered. The first fit includes the inflection point and 10 points on either side, then the start point and end point are systematically extended away from the inflection, fitting and recording the slope for each set of endpoints, which gives multiple fits with the same number of data points. Figure 3.5 shows the PF slope for all fit ranges considered for a particular pixel (same pixel as Fig. 3.3), and displays the corresponding rms error as a colorbar. We notice that the single 21-point fit has a relatively low PF slope, but adding more data points causes the PF slope to decrease a small amount for up to the inclusion of 5 extra data points. Why including more data points decreases the PF slope is again related to the asymmetry of the IV curves, where including more points on one side of the inflection finds the more flat region of the curve. Because we are fitting near the inflection point, adding more points to the fit leaves the rms error is relatively unchanged.

Looking back at the dielectric constant of VO_2 we can check that the minimized PF slopes are reasonable. Ko's measured dielectric data and error and our temperature fit, $\varepsilon_V(T)$ are shown in Fig. 3.6, along with the corresponding PF slope as a color-scale for reasonable values of T and ε_V and a constant film thickness of 187 nm. From this plot, we expect the PF slope to be between about 1 and 3 $V^{-1/2}$, which we do find across the image (Fig. 3.2).

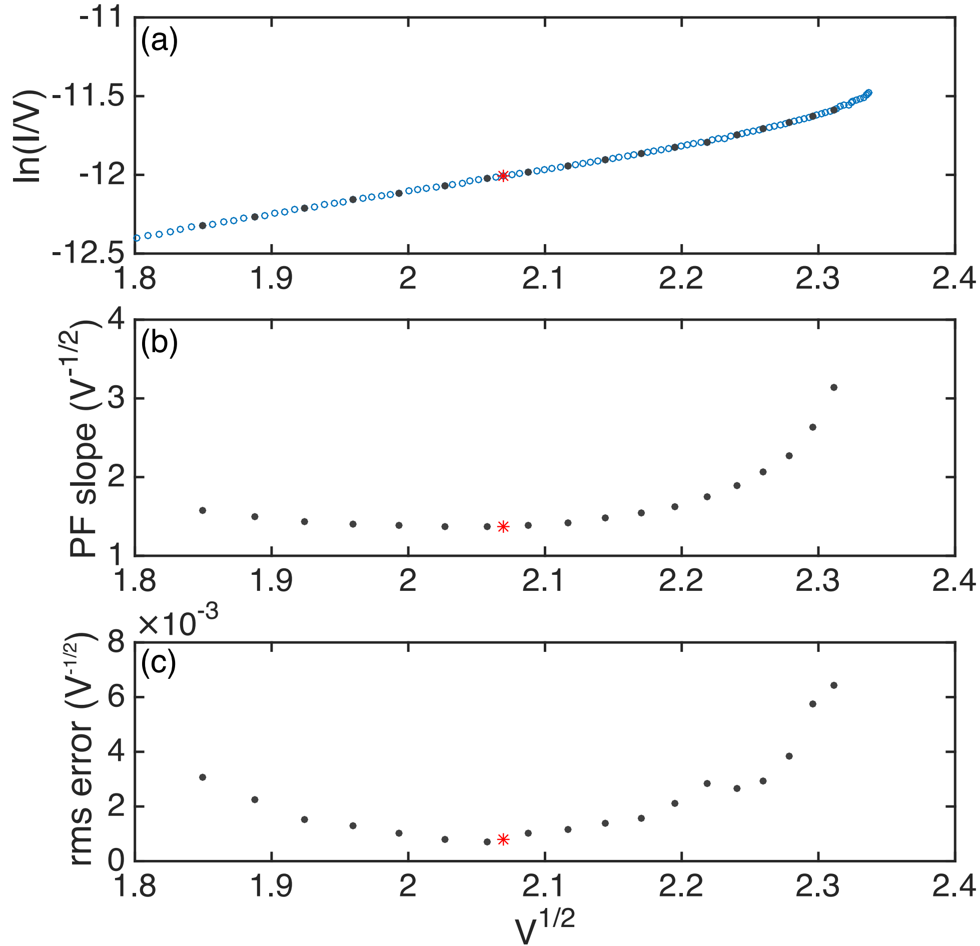

Figure 3.4: (a) A typical PF linearized IV curve, with black points indicating the center of a fixed length 21-point fitting region. (b) The resultant PF slope from the 21-point region centered at the black points. (c) The rms error corresponding to the fit centered at each black point. The numerically solved inflection and corresponding PF slope and rms error are shown as a red star on each panel.

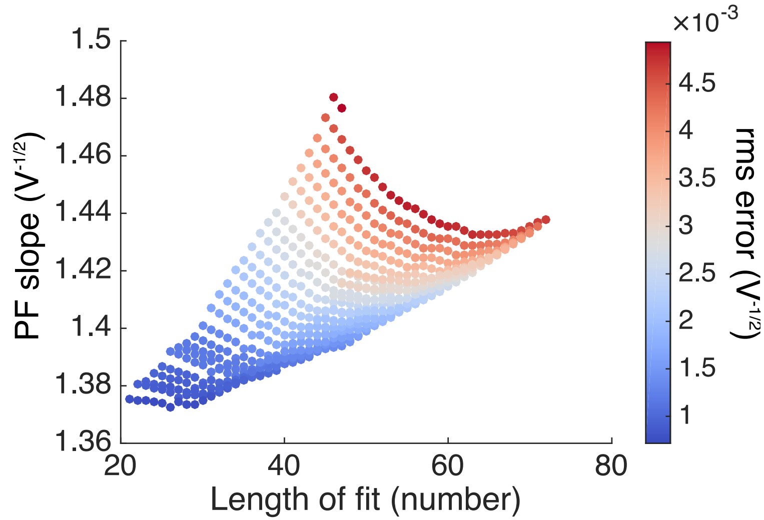

Figure 3.5: The PF slope as a function of number of data points and colorbar corresponding to the rms error.

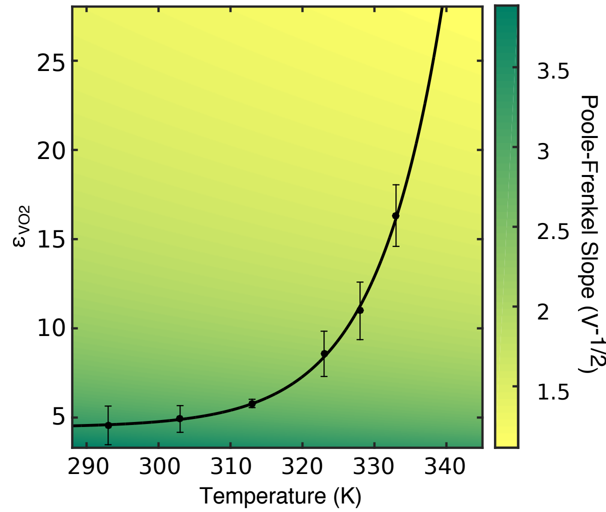

Figure 3.6: Relation between the dielectric constant, PF slope and temperature of the film. The raw dielectric constant data for a similar film of VO_2 grown on n-type Si(100) substrate (black points) with reported errors and a phenomenological exponential fit to the data (black line) as a function of temperature are overlaid on the corresponding PF slope P for the average film thickness $d = 187$ nm.

3.3 Temperature

We fit the PF linearized IV curves, and use the defined relation $P = e^{3/2}/[(\pi\varepsilon_0\varepsilon_V d)^{1/2}\ k_B T]$ (Eq. 2.28). Most of the factors in P are fundamental constants, leaving only the film thickness d and relative dielectric constant ε_V to be measured, before determining T, both of which have already been measured.

The interpolated temperature-dependent dielectric constant, $\varepsilon_V(T)$ must be used self-consistently to determine the temperature of each point on the map. The temperature immediately preceding the transition is calculated at each point on the map, and the resulting temperatures are shown in Fig. 3.7 (a), along with the corresponding histogram (b). We find an average temperature of 335 K, with a standard deviation of 4 K. We note the sharp cut off of calculated temperatures at 340 K, the bulk IMT temperature, very close to the IMT temperature of our film $\sim$ 339 K.

We once again notice that the temperature varies little within each grain, but that the calculated temperature seems to abruptly change across some grain boundaries. Some of the sharp changes in temperature across grain boundaries correspond to grains that exhibit more than one current jump in the IV curves. The grains with multiple jumps can be correlated with some of the cooler grains in the temperature map. In the following section we discuss IV curves with multiple jumps. We also notice a similar, but less pronounced effect as observed in the electric field map, where higher temperatures were calculated in the bottom third of the image. Higher calculated temperatures in the bottom third of the image are consistent with the hypothesis that the SiO_x interfacial layer caused the VO_2 film to require more input energy, and hence it was warmed to a slightly higher temperature than the first 2 thirds of the film.

The uncertainty in the temperature extracted from each IV curve is around 4 K, which is determined by combining the uncertainty from film thickness d, the dielectric constant ε_V, and the PF slope, P. The details of which are outlined in Appendix B.

The VO_2 film was not heated by an external heater and all IV curves were collected at room temperature, yet we calculate an average temperature of each pixel directly under the tip, just before the transition to be 335 K. This raised calculated temperature is evidence that Joule heating has occurred via the voltage-induced current. We note that due to the necessity of fitting a slope, the calculated temperature is a temporal average immediately preceding the transition and the real temperature at the transition is presumably larger, and even closer to the IMT temperature.

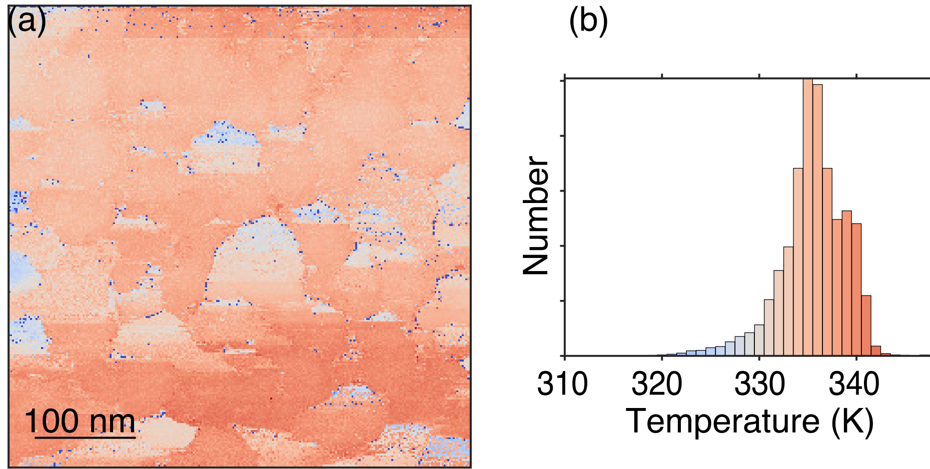

Figure 3.7: (a) Map of the temperature of the film immediately preceding the IMT as calculated through the application of the PF conduction mechanism. (b) Histogram of the temperature map. The color corresponds to the color bar for the map in (a).

3.3.1 Number of Jumps

We observe about 20% of IV curves that have more than one transition. Figure 3.8 shows two PF linearized IV curves from adjacent pixels with more than one transition, one fit above and one fit below the first, smaller transition. We characterize each curve by the number of jumps, and a map of the number of transitions is shown in Fig. 3.9 (a). By comparing with the topography of the image we notice that the number of transitions is generally consistent within grains. For over half of IV curves with multiple jumps, the region preceding the largest and final jump is fit as a measure of the temperature before the temperature, just like curves with one transition. An example of a curve fit before the largest transition is shown in Fig. 3.8 (b). However, in less than 10% of all curves the data immediately preceding the final jump is too noisy, or there are not enough data points to be accurately fit. In these cases the curve is fit before the preceding smaller jump as an approximation of the temperature before the IMT. Figure 3.8 (a) is an example of a curve where the PF slope was fit below the smaller transition.

Curves with multiple jumps may be due to a slightly O-deficient V-O stoichiometry in part or all of the grain, or stacked grains in the z-direction. O-vacancies lower the transition temperature in VO_2, which would account

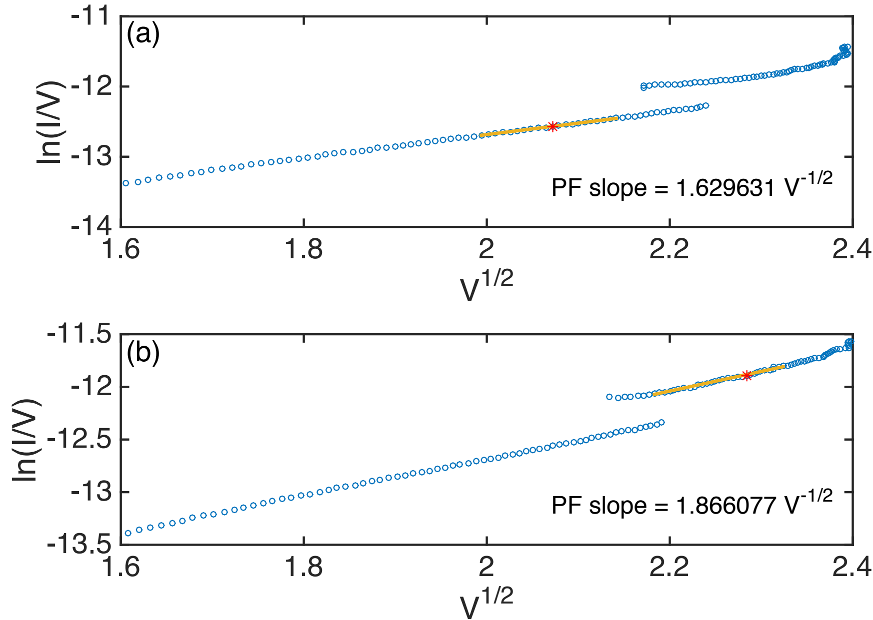

Figure 3.8: Adjacent PF linearized *IV* curves with multiple jumps. (a) An *IV* curve fit before the first jump as an approximation, since the data post first transition is too noisy. (b) An *IV* fit before the final and largest transition (post-transition not shown). In both data sets the discontinuity arises from the correction of the continuously ramped V_{meas}, to show V_{film} on the x-axis.

for some parts of the region in contact with the tip transitioning before the stoichiometric VO_2 regions. Stacked grains over the thickness of the film could transition at different temperatures, which we observe as a partial transition in an *IV* curve.

In Fig. 3.9 (b) we show the temperature histogram in dark green and overlay the temperature values from curves with two or more transitions light green. This histogram indicates that fitting the curves with multiple transitions follows a similar distribution to that of all of the temperatures calculated, even if it may lower the overall average temperature of the image.

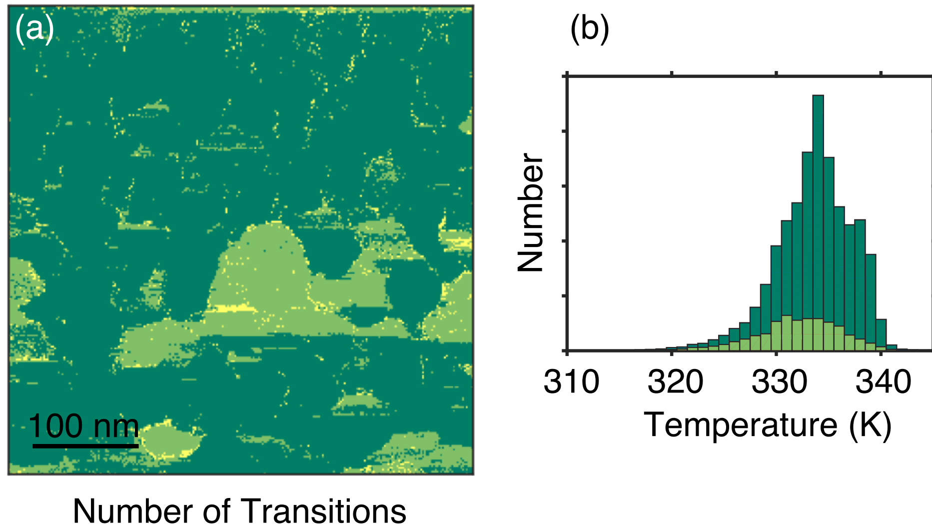

Figure 3.9: (a) A trimodal map of the number of jumps in each IV curve. The regions of dark green have one transition, the light green regions have two transitions in the IV curves, and the yellow points have more than two transitions in their IV data. (b) The temperature histogram, with the values due to pixels with more than one jump indicated by the light green color.

3.4 Discussion

Both the electric field and temperature maps show little variation within each grain, but larger values at the grain boundaries. While the grains are evident in the topographic maps, the behavior observed in the electric field and temperature maps are not an artifact from using the topography in our calculations. Differences between the interior and boundary of the grains are observed in the raw IV data and in the PF slope map (Fig. 3.2), where the film thickness has not yet been taken into account, which is evidence that we are in fact measuring local properties of the film.

The temperature of the film must lie in a narrow window between room temperature and the measured IMT temperature (i.e., 293 K - 340 K). If the temperature calculation produced values outside of this range, we would be forced to concede that either the PF mechanism is not applicable or some other aspect of the calculation is incorrect. However, using only the independently measured dielectric constant and fundamental constants, only 804 of 65,536 pixels (1.2%) of the measured temperatures do not fall within this range. In a further 540 cases the noise is too large or the data correction

procedure was not fit correctly so we disregard the pixel, giving it a 'not a number' value, one such example is shown in Fig. 3.10. This degree of self consistency gives us confidence in our calculations.

The pixels that don't fall into the reasonable temperature range fail to do so because of errors when fitting, noisy *IV* curves, or are within error of the IMT temperature. The error on each temperature calculation is 4 K (Appendix B), and the pixels with calculated temperature up to 4 degrees above 340 K are not unreasonable. In total there are 93 pixels with a calculated temperature above 344 K, and all but 2 these are due to poor fits due to noisy data.

Of the 804 that do not fall within the range 293 K - 340 K, 776 all are above 340 K and 28 are below 293 K. Looking specifically at the pixels with a calculated temperature above 342 K the number drops to only 175. We manually check the *IV* curves with calculated temperatures above 342 K to determine whether bad fitting or poor data quality is causing high temperatures to be calculated. Of the 175 pixels above 342 K, 120 occur in the first row of the image and are due to noisy *IV* curves, and a further 33 of the fits are due to poor quality *IV* curves elsewhere in the map. 4 are due to poor fitting as a result of two jumps in the *IV* curve. The remaining 18 throughout the map are the result of good fits where the calculated a temperature was above 342 K. An example of a curve with a calculated temperature above 344 K is shown in Fig. 3.10 (d), with *IV* through the film shown in (c). Extrapolating from the distribution of *IV* curves above 342 K, we argue that the majority of the *IV* curves with a calculated temperature between 340 K and 344 K are not at a higher calculated temperature, but instead are due to poor fits or noisy data.

Of the 28 that result in a temperature below 293 K all calculated temperatures are due to fitting the PF slope too close to noise immediately preceding the transition or fitting across as small 'jump' in the data that was not classified as a transition. An example of the latter is shown in Fig. 3.10 (f), with the voltage corrected *IV* data shown in (e).

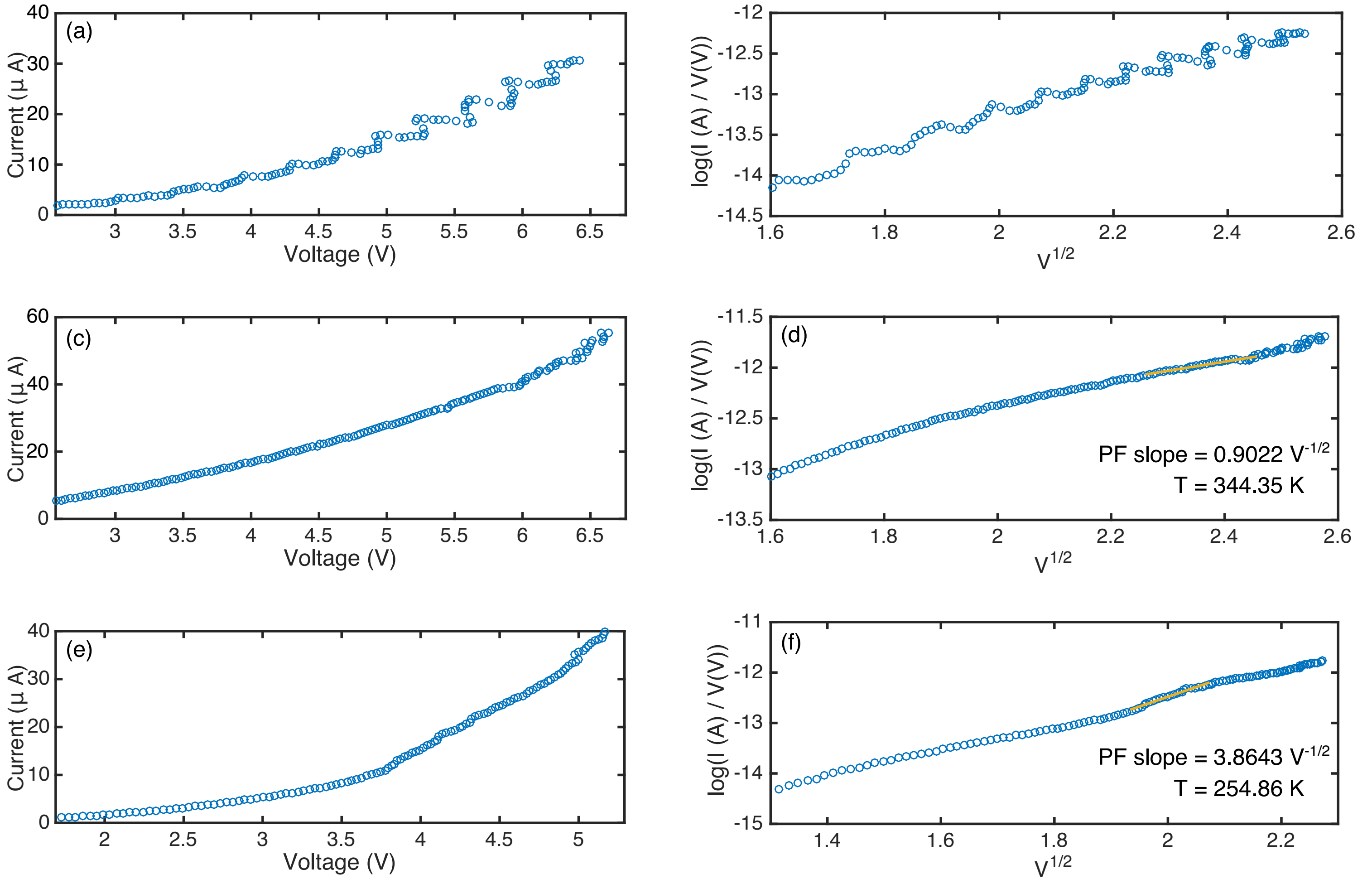

Figure 3.10: **(a)** An example of an *IV* curve through the film that is too noisy to fit. **(b)** PF-linearized *IV* data from (a) that is too noisy to fit. **(c)** An example of an *IV* curve through the film that results in a temperature above 344 K. **(d)** PF-linearized *IV* data from (d) that calculates a temperature above 344 K. **(e)** An example of an *IV* curve through the film that results in a temperature below 293 K. **(f)** PF-linearized *IV* data from (e) that calculates a temperature below 293 K.

Chapter 4

Nanoscale Thermometry

4.1 Other Nanoscale Thermometry Techniques

The technique described within this thesis is capable of measuring the temperature of a film with uncertainty 4 K within the range 100 K - 400 K, and with spatial resolution on the order of 70 nm diameter without the need for a calibration. Most available local thermometry techniques are severely constrained by poor spatial resolution, limited temperature range, need for calibration, or inability to determine absolute temperature without a known reference. We describe other thermometry techniques at the forefront of research, which employ the thermoelectric effect, temperature dependent excited states in fluorescent Er/Yb particles, nitrogren vacancy (NV) centers, and electron energy loss spectroscopy, and temperature dependent Raman modes, near-IR radiation and reflectivity, scanning probes, and superconducting junctions.

Sadat *et. al* and Kim *et. al* use the thermoelectric effect, which describes the relationship between electric voltages and temperature differences, where the proportionality is known as the Seebeck coefficient. Both groups use a coated AFM tip, and can achieve spatial resolution on the order tip contact diameter, of around 10 nm. Sadat uses a Pt-coated AFM cantilever tip in contact with an Au surface to calibrate the relationship between the voltage and temperature [90]. To calibrate, a Au-Al_2O_3-Au layered structure is fabricated which electrically isolates the two Au layers. A sinusoidal electrical current of known frequency and amplitude is passed through to bottom Au layer, resulting in a temperature oscillation at twice the input frequency. The temperature oscillations (ΔT) on the top electrode are directly related to the voltage oscillations (V_{Au}) in the top Au layer by

$$V_{\text{Au}} = I_{\text{top}} R \alpha \Delta T, \tag{4.1}$$

where I_{top} is a constant supplied current, R is the resistance and α is the temperature coefficient of the top Au layer, which are characterized experimentally separately. Next, the tip is brought into soft contact with the Au, and the thermoelectric voltage of the Pt-Au junction is measured and

related to the induced temperature of the junction. A relationship between V_{tip} and ΔT is established and can map thermal gradients across a film. Kim *et. al* obtain the Seebeck coefficient of a Au-Cr junction on a tip (Fig. 4.1) [91]. With the tip in thermal contact with the film, the film is heated and they measure the thermoelectric voltage across the Au-Cr junction on the tip and the temperature difference between the substrate and cantilever using two thermocouples. They then relate the difference in temperature to the measured voltage, extracting the Seebeck coefficient of the Au-Cr tip junction.

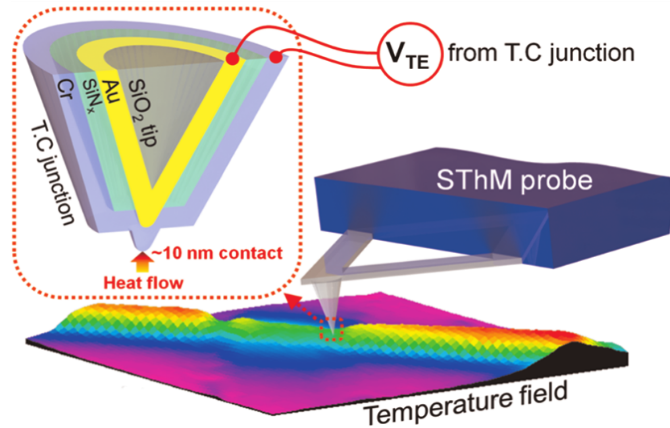

Figure 4.1: The Au-Cr junction on a tip in Kim's thermal probe technique. Reproduced from Kim *et. al* [91].

Fluorescent particles made from Er/Yb ions doped onto a film have been used as a temperature probe by exploiting the temperature dependent excited states of the ions [26, 92]. The spatial resolution of the technique is determined by particle size, which is on the order of 1 μm. The particles are excited by a non-linear mechanism called photon up-conversion, where a laser diode of wavelength 980 nm causes two photons to be absorbed by an Yb ion. The excitation is then transmitted to an adjacent Er ion which radiatively relaxes to its ground level, emitting photons at lower wavelength, which are measured by a microscope and photomultiplier tubes. In this case there are two peaks of interest corresponding to transitions between the excited energy levels ${}^2H_{11/2}$ and ${}^4S_{3/2}$, and the ground level ${}^4I_{15/2}$, at wavelengths 527 nm and 550 nm respectively. The relative integrated intensity of the two peaks is temperature dependent and is related by $I_{527}/I_{550} \propto \exp -\Delta E/k_B T$, where I_{527} and I_{550} are the integrated intensity of the peaks at 527 nm and 550 nm

respectively in the photoluminescence spectra, ΔE is the difference in energy between the transitions [92]. The relationship I_{527}/I_{550} must be calibrated by measuring the fluorescence spectra of a heated substrate at two known temperatures. Zimmers *et. al* used this technique on a VO_2 thin film, using room temperature and the IMT temperature as calibration points [26]. Using the IMT temperature as a calibration point seems circular and may implicity impose assumptions about the IMT on the rest of the measurement.

Typically the first order Raman modes in semiconductors exhibit a temperature dependent shift that can be be calibrated to measure the temperature of films [93]. Reparaz *et. al* use two lasers, a heating laser below a film or membrane and a probe laser above to determine the thermal conductivity of a material or to map the thermal field of the surface. The relationship between the Raman shift and temperature is calibrated using a known bath temperature and heater temperature. A linear relationship between temperature and Raman shift is fit from 200 K - 800 K, and a separate linear relationship is found below 150 K.

Mecklenburg *et. al* use a scanning transmission electron microscope to measure the electron energy loss spectroscopy (EELS) of 80 nm thick Al wires [94]. Since they are detecting phonons, they detect temperature variations on the order of the phonon's mean free path, between 2 and 5 nm. They quantify the local change in density of Al wires through the EELS data, they then use well-studied thermal expansion data of Al to relate the shift of the plasmon peak to a temperature shift. Fig. 4.2 shows the EELS data for Al at room temperature, 293 K, and raised temperature 413 K. The peak shift is quite small, so they use curve fitting to improve the sensitivity of quantifying the energy shift and temperature shift. This technique could be extended to metals and semiconductors that have sufficiently sharp plasmon resonances and have well documented and accurate thermal expansion data.

Two notable methods use a charge coupled device (CCD) camera to capture near-IR radiation [95] or near-IR reflectivity which are proportional to a temperature variation [96, 97]. Techniques that use near-IR wavelengths and a CCD camera are spatially limited by the detection wavelength, and can only probe length scales on the order of 400 nm. Teyssieux *et. al* use Planck's law for grey body radiation to relate the IR signal to the temperature. In this case the emissivity of the material must first be measured. First, the optical characteristics of a sufficiently large chromium thin film is measured by a spectrometer. An emissivity of 0.7 is determined and is assumed to be constant over the temperature range of interest. Second, the film is heated by a large flat resistor and a thermocouple and pyrometer are used to measure the film's surface temperature to calibrate the effective

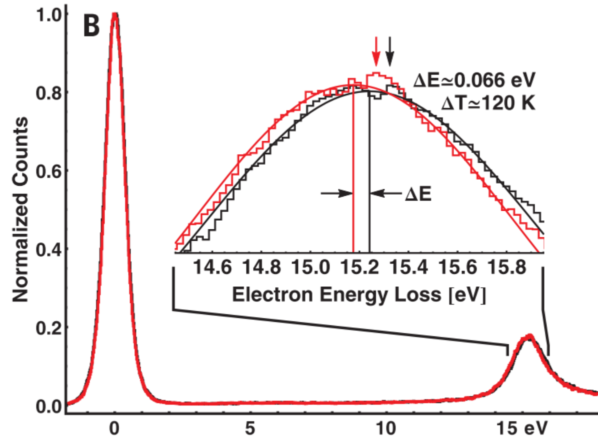

Figure 4.2: Aluminum EELS data characteristic of 293 K (black) and 413 K (red).The vertical lines in the inset indicate the plasmon peak centers, as determined by curve-fitting, and the arrows indicate the peak maxima. Reproduced from Mecklenburg *et. al* [94].

transmittivity of the microscope. They can relate the radiated IR signal measured to the temperature. Since this technique relies on radiation from the material, the minimum detection temperature is on the order of 500 K. Tessier *et. al* use a CCD camera to measure the near-IR reflectivity R and the reflectivity variations ΔR [96]. A spatial map of the relative reflectivity, $\Delta R/R$ is imaged which eliminates parasitic reflections and the uniform background reflection. The relative reflectivity is related to temperature variations by $\Delta R/R = (1/R)(\partial R/\partial T)\Delta T$, where $(1/R)(\partial R/\partial T)$ is constant. In this method the temperature variations are found, and must be related to a known reference temperature.

Menges *et. al* account for unknown tip-sample contact resistance that arises in thermal resistive scanning probe measurements by measuring the time-dependent and time averaged heat flux [98]. They use tip-sample heat flux measurements to calculate the temperature field map of an InAs nanowire. When using sufficiently small frequency, the applied voltage bias leads to a steady-state temperature increase and a continuous modulation of the temperature, at twice the excitation frequency. The change in sample temperature affects the tip-sample heat transfer ($\dot{Q}_{\mathrm{ts,AC}}$), which in turn is related to the power dissipated in the probe sensor and sensor temperature, and is proportional to the electrical resistance of the sensor. A diagram of the measurement and relevant resistances and heat flow is depicted in Fig.

4.3. Sensor temperature is given by $T_{\text{sensor}} = T_{\text{sensor,DC}} + T_{\text{sensor,AC}} \sin(2\omega t)$. The change in sample temperature can be written as,

$$\Delta T_{\text{sample}} = T_{\text{sensor,AC}} - \dot{Q}_{\text{ts,AC}} \times R_{\text{ts}}, \tag{4.2}$$

where the R_{ts} is the electrical resistance in the tip-sample contact, and can be written as

$$R_{\text{ts}} = \frac{T_{\text{sensor,DC}} - T_{\text{sensor,AC}} - T_{\text{RT}}}{(\dot{Q}_{\text{ts,DC}} - \dot{Q}_{\text{ts,AC}})}, \tag{4.3}$$

with T_{RT} as room temperature, the reference temperature. By measuring the time-dependent and time-averaged heat flux $T_{\text{sensor,DC}}$ and $T_{\text{sensor,AC}}$ are measurable quantities, so R_{ts} can be accounted for and T_{sample} can be calculated.

Fluorescent nitrogen-vacancy (NV) centers have temperature dependent crystal field splitting, which have been used to measure the temperature of films, and even extended to human cells [99, 100]. The transition frequency can be optically detected with a spatial resolution on the order of 100 nm, the nominal diameter of the particles. In the absence of an external magnetic field, the transition frequency between $m_s = 0$ and $m_s = \pm 1$ has a known temperature dependence of -$2\pi \times 77$ kHz/K, due to temperature dependent lattice strains. The frequency dependence of the splitting has been reported for the temperature range 300 - 700 K, and determines the applicable temperature range for this technique [101]. The electronic spin of an NV center must first be decoupled from a fluctuating external magnetic field for accurate temperature sensing. The NV center is decoupled from an external field by applying a microwave pulse for half the population time, τ, to populate a superposition of $m_s = 1$ and $m_s = -1$ states. Then a 2π echo pulse is applied that switches the population of the two states. After a full population time, 2τ, the magnetic field induced shifts have been eliminated, and temperature gradients can be accurately sensed.

Halbertal *et. al* describe a non-contact scanning probe technique, based on a superconducting quantum interference device (SQUID) on the apex of a sharp quartz pipette, SQUID-on-tip (SOT) [102]. The current measured by a superconducting junction has a strong temperature dependence in the vicinity of the critical temperature of the junction, $I_C(T) \simeq I_0(1 - T/T_C)$. When biasing the SOT above the critical current of the junction, the current through the SOT is linearly temperature dependent. They find $dI_{\text{tSOT}}/dT = -9.5\ \mu\text{A/K}$ for their Pb SC junction below the critical temperature, and $dI_{\text{tSOT}}/dT = -13.7\ \mu\text{A/K}$ near the critical temperature. Since the SOT is not in contact with the film, the temperature of the device and the temper-

ature measured by the tip must first be correlated. To correlate the temperature measured by the SOT and the temperature of the film they exploit IMT of a In_2O_3 film grown on a SiO_2/Si substrate on a Au/Cr heater with a Al_2O_3 insulating layer. They globally vary the temperature and measure $R(T)$ in the In_2O_3 and the current through the SOT as a function of temperature in thermal equilibrium conditions to correlate the temperatures. Then, by driving a micro-heater with an AC current, they induce a temperature at double the frequency in the film and the SOT. The resulting AC temperature is measured by applying a probing DC current along the current leads of the In_2O_3. Finally, they measured the resultant temperature in the SOT as a function of SOT height above the film to calibrate the temperature of the SOT as a function of height. This method has comparable spatial resolution to our technique, but is limited by low SC critical temperatures.

We summarize the techniques and any required calibration or measurement in Table 4.1 and Fig. 4.4, with the applicable temperature range and spatial resolution.

Table 4.1: Summary of nanoscale thermometry techniques. PF conduction refers to the technique described in this paper.

Technique	Calibration	Temperature range	Spatial resolution
thermoelectric effect [90, 91]	material dependent tip-contact calibration	variation about RT	10 nm
fluorescent Er/Yb particles [26, 92]	ratio of photon emission at 527 nm and 550 nm, must fit 2 parameters	300 K - 400 K	1000 nm
Raman shift [93]	calibrate temperature dependence of Raman shift	$<$ 800 K	300 nm
EELS [94]	correlate the plasmon resonance and thermal expansion of the material	200 K - 600 K	5 nm
near-IR radiation [95]	CCD camera to measure radiation, must first relate signal to temperature	$>$ 500 K	400 nm
near-IR reflectivity [96, 97]	CCD camera to measure reflection, must first relate to temperature	variation about RT	440 nm
thermo-resistive scanning probe [98]	must account for tip-sample contact resistance	variation about RT	10 nm
NV centers [99, 100]	external measurement of temperature dependence of NV spins	120 K - 700 K	50 nm
SC junction [102]	thermal properties of sensor and coupling to sample must be measured	near T_c	50 nm
PF conduction	must measure film dielectric constant and thickness	100 K - 400 K	70 nm

4.2 Extension of Thermometry Technique

We have demonstrated the use of IV curves fit to the temperature-dependent PF conduction mechanism to calculate the local temperature of a thin VO_2 film immediately preceding the IMT. The technique described in this thesis is unique in that it can measure the temperature of a film on the nanoscale without the use of a reference temperature or calibration. The thickness and temperature-dependent dielectric constant of the film must be known or measurable by another method, however our calculation leaves no free parameters to vary to obtain the temperature of the film.

This novel thermometry technique has addressed the debate surrounding the origin of the field-induced IMT in VO_2. The technique can readily be extended to other materials dominated by the PF mechanism. For example ZnO has been considered for application in resistance random access memory devices [103], for thin film transistors in displays, and for electron transfer layers in solar cells [104, 105]. Other materials that follow PF conduction, and also have potential applications in resistive switching devices include SnO_x, AlO_x, CeO_x, and WO_x [106].

Furthermore, the more general technique of using IV data to calculate the local temperature of the film can be extended to other temperature dependent conduction mechanisms. Section 2.4 discusses other conduction mechanisms in detail, but here we note that Schottky field emission, Fowler-Nordheim tunneling, thermionic-field emission, hopping conduction, Ohmic conduction, and ionic conduction can all be linearized in terms of current and voltage which will produce a slope that is dependent on the film temperature. Depending on the mechanism, various film properties must either be known or measured in order to accurately calculate the temperature of the film. As an example, which is discussed in Sect. 2.4, to reliably use the hopping mechanism to calculate the temperature of the film the hopping distance must either be known, measured, or assumed.

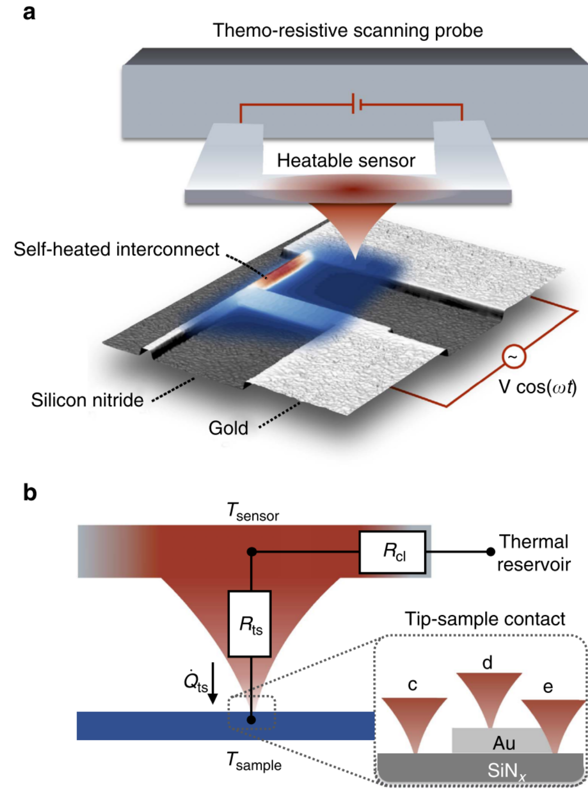

Figure 4.3: (a) Schematic of the thermoresistive scanning probe in contact with a self-heated gold (Au) interconnect (∼100 nm wide) on a silicon (111) substrate wafer covered with 150 nm of amorphous silicon nitride (SiN_x). An alternating voltage bias (V$\cos(\omega t)$) is applied to modulate the sample temperature. The sample temperature field (red - blue color scheme indicates the temperature from hot to cold) is inferred by simultaneously probing a time-dependent and a time-averaged heat flux signal between the heatable (red colored) sensor and the temperature-modulated sample. (b) The sensor is decoupled from its thermal reservoir by the thermal resistance of the cantilever (R_{cl}). The tip-sample heat flux $\dot{Q}_{\mathrm{ts}}$ is not only a function of the temperature difference between the sensor (T_{sensor}) and sample (T_{sample}), but also of the tip - sample contact thermal resistance (R_{ts}). Changes of the tip-sample contact due to (c - d) the material in contact with the tip, (d-e) the tip-sample contact area and tribological effects cause variations of R_{ts}. Reproduced from Menges *et. al* [98].

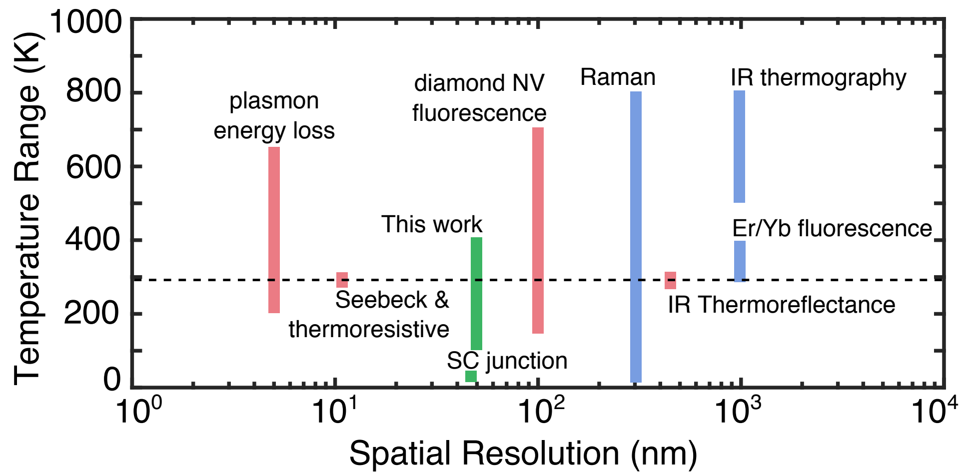

Figure 4.4: Reported applicable temperature ranges and spatial resolution of thermometry techniques. The dotted line is room temperature. Pink bars and red dots represent methods that require a reference temperature and measure the temperature fluctuation. Red dots were demonstrated at room temperature only. Blue lines represent models where a calibration is required to measure the temperature over the applicable range. Green lines represent methods where no calibration or reference temperature is required to measure the temperature over the range.

Chapter 5

Conclusion

We use a CAFM to ramp a voltage bias across a VO_2 thin film, and observe the IMT via the measured current. Using the voltage at which the film transitions and the local film thickness, we calculate an average electric field of 32 MV/m $\pm$ 3 MV/m at the transition. We then fit the measured IV curves to the temperature-dependent PF conduction mechanism. By using the film thickness and dielectric constant we directly calculate the average local temperature of the film immediately preceding the transition to be 335 K $\pm$ 4 K. The electric field at the transition ranges from around 27 MV/m to 37 MV/m, while the temperature values range from 326 K to 340 K.

All measurements were performed in an apparatus at room temperature and yet we measure a local temperature approximately 40 K above room temperature. We have shown that the film is locally warmed, and we have put a lower bound of the local temperature of the film. We argue that the film is close to and plausibly equal to the IMT temperature of 340 K. We conclude that the high applied voltage is not solely responsible for the transition, and instead Joule heating has locally warmed the film close to its transition temperature.

Bibliography

[1] C. N. R. Rao. Transition metal oxides. *Annual Review of Physical Chemistry*, 40:291–326, 1989. doi:10.1146/annurev.pc.40.100189.001451.

[2] F. J. Morin. Oxides Which Show a Metal-to-Insulator Transition at the Neel Temperature. *Physical Review Letters*, 3(1):34–36, 1959. doi:10.1103/PhysRevLett.3.34.

[3] A. L. Pergament, G. B. Stefanovich, and A. A. Velichko. Oxide Electronics and Vanadium Dioxide Perspective : A Review. *Journal on Selected Topics in Nano Electronics and Computing*, 1(1):24–43, 2013. ISSN 2311-1801. doi:10.15393/j8.art.2013.3002.

[4] Peijun Guo, Matthew S. Weimer, Jonathan D. Emery, Benjamin T. Diroll, Xinqi Chen, Adam S. Hock, Robert P. H. Chang, Alex B. F. Martinson, and Richard D. Schaller. Conformal Coating of a Phase Change Material on Ordered Plasmonic Nanorod Arrays for Broadband All-Optical Switching. *ACS Nano*, page acsnano.6b07042, 2016. ISSN 1936-0851. doi:10.1021/acsnano.6b07042.

[5] Aaron Holsteen, In Soo Kim, and Lincoln J. Lauhon. Extraordinary Dynamic Mechanical Response of Vanadium Dioxide Nanowires around the Insulator to Metal Phase Transition. *Nano Letters*, 14: 1898–1902, 2014. doi:10.1021/nl404678k.

[6] S. M. Babulanam, T. S. Eriksson, G. A. Niklasson, and C. G. Granqvist. Thermochromic VO2 films for energy-efficient windows. *Solar Energy Materials*, 16:347–363, 1987. doi:10.1016/0165-1633(87)90029-3.

[7] C. G. Granqvist. Window coatings for the future. *Thin Solid Films*, 193-194(Part 2):730–741, 1990. ISSN 00406090. doi:10.1016/0040-6090(90)90225-3.

[8] You Zhou, Xiaonan Chen, Changhyun Ko, Zheng Yang, Chandra Mouli, and Shriram Ramanathan. Voltage-triggered Ultra-fast Metal-insulator Transition in Vanadium Dioxide Switches. *IEEE Electron Device Letters*, 34:202, 2013. doi:10.1109/Led.2012.2229457.

[9] Petr Markov, Robert E. Marvel, Hiram J. Conley, Kevin J. Miller, Richard F. Jr. Haglund, and Sharon M. Weiss. Optically Monitored Electrical Switching in VO2. *ACS Photonics*, 2:1175–1182, 2015. doi:10.1021/acsphotonics.5b00244.

[10] Jeehoon Kim, Changhyun Ko, Alex Frenzel, Shriram Ramanathan, and Jennifer E Hoffman. Nanoscale imaging and control of resistance switching in VO 2 at room temperature. *Applied Physics Letters*, 96: 213106, 2010. doi:10.1063/1.3435466.

[11] C. Zhou, D. M. Newns, J. A. Misewich, and P. C. Pattnaik. A field effect transistor based on the Mott transition in a molecular layer. *Applied Physics Letters*, 70:598–600, 1997. doi:10.1063/1.118285.

[12] T. Driscoll, H. T. Kim, B. G. Chae, M. Di Ventra, and D. N. Basov. Phase-transition driven memristive system. *Applied Physics Letters*, 95(4):043503, 2009. ISSN 00036951. doi:10.1063/1.3187531.

[13] Sung-Hwan Bae, Sangmin Lee, Hyun Koo, Long Lin, Bong Hyun Jo, Chan Park, and Zhong Lin Wang. The memristive properties of a single VO2 nanowire with switching controlled by self-heating. *Advanced Materials*, 25(36):5098–5103, 2013. ISSN 09359648. doi:10.1002/adma.201302511.

[14] Jihoon Kim, Kyongsoo Park, Songhyun Jo, Bong-jun Kim, Hyun Wook Kang, Seung Yun Nam, Junghwan Oh, and Yong Wook Lee. Memristive states in vanadium-dioxide-based planar devices stimulated by 966 nm infrared laser pulses. *Japanese Journal of Applied Physics*, 54: 102601, 2015. doi:10.7567/JJAP.54.102601.

[15] Sven Westman. Note on a Phase Transition in VO2. *ACTA Chemica Scandinavica*, 15:217, 1961. doi:10.3891/acta.chem.scand.15-0217.

[16] John B. Goodenough. The two components of the crystallographic transition in VO2. *Journal of Solid State Chemistry*, 3(4):490–500, 1971. ISSN 1095726X. doi:10.1016/0022-4596(71)90091-0.

[17] Masatoshi Imada, Atsushi Fujimori, and Yoshinori Tokura. Metal-insulator transitions. *Reviews of Modern Physics*, 70(4):1039–1263, 1998. doi:10.1103/RevModPhys.70.1039.

[18] M. W. Haverkort, Z. Hu, A. Tanaka, W. Reichelt, S. V. Streltsov, M. A. Korotin, V. I. Anisimov, H. H. Hsieh, H. J. Lin, C. T. Chen, D. I. Khomskii, and L. H. Tjeng. Orbital-assisted metal-insulator transition in VO2. *Physical Review Letters*, 95(19):4–7, 2005. ISSN 00319007. doi:10.1103/PhysRevLett.95.196404.

[19] Salinporn Kittiwatanakul, Stuart A Wolf, and Jiwei Lu. Large epitaxial bi-axial strain induces a Mott-like phase transition in VO2. *Applied Physics Letters*, 105:073112, 2014. doi:10.1063/1.4893326.

[20] Gokul Gopalakrishnan, Dmitry Ruzmetov, and Shriram Ramanathan. On the triggering mechanism for the metal âĂŞ insulator transition in thin film VO 2 devices : electric field versus thermal effects. *Journal of Materials Science*, 44:5345–5353, 2009. doi:10.1007/s10853-009-3442-7.

[21] Changhyun Ko and Shriram Ramanathan. Observation of electric field-assisted phase transition in thin film vanadium oxide in a metal-oxide-semiconductor device geometry. *Applied Physics Letters*, 93:252101, 2008. doi:10.1063/1.3050464.

[22] Byung Gyu Chae, Hyun Tak Kim, Doo Hyeb Youn, and Kwang Yong Kang. Abrupt metal-insulator transition observed in VO2 thin films induced by a switching voltage pulse. *Physica B: Condensed Matter*, 369 (1-4):76–80, 2005. ISSN 09214526. doi:10.1016/j.physb.2005.07.032.

[23] Yong Wook Lee, Bong-Jun Kim, Jung-Wook Lim, Sun Jin Yun, Sungyoul Choi, Byung-Gyu Chae, Gyoungock Kim, and Hyun-Tak Kim. Metal-insulator transition-induced electrical oscillation in vanadium dioxide thin film. *Applied Physics Letters*, 92(16):52–55, 2008. ISSN 00036951. doi:10.1063/1.2911745.

[24] Dmitry Ruzmetov, Gokul Gopalakrishnan, Jiangdong Deng, Venkatesh Narayanamurti, and Shriram Ramanathan. Electrical triggering of metal-insulator transition in nanoscale vanadium oxide junctions. *Journal of Applied Physics*, 106:083702, 2009. doi:10.1063/1.3245338.

[25] Zheng Yang, Changhyun Ko, Viswanath Balakrishnan, Gokul Gopalakrishnan, and Shriram Ramanathan. Dielectric and carrier

transport properties of vanadium dioxide thin films across the phase transition utilizing gated capacitor devices. *Physical Review B*, 82: 205101, 2010. ISSN 10980121. doi:10.1103/PhysRevB.82.205101.

[26] A. Zimmers, L. Aigouy, M. Mortimer, A. Sharoni, Siming Wang, K. G. West, J. G. Ramirez, and Ivan K. Schuller. Role of Thermal Heating on the Voltage Induced Insulator-Metal Transition in VO 2. *Physical Review Letters*, 110(February):056601, 2013. doi:10.1103/PhysRevLett.110.056601.

[27] B. Wu, A. Zimmers, H. Aubin, R. Ghosh, Y. Liu, and R. Lopez. Electric-field-driven phase transition in vanadium dioxide. *Physical Review B*, 84:241410, 2011. doi:10.1103/PhysRevB.84.241410.

[28] C. N. Berglund and H. J. Guggenheim. Electronic Properties of VO2 near the Semiconductor-Metal Transition. *Physical Review*, 185(3): 1022–1033, 1969. ISSN 0031899X. doi:10.1103/PhysRev.185.1022.

[29] G. J. Hyland. On the electronic phase transitions in the lower oxides of vanadium. *Journal of Physics C: Solid State Physics*, 1(1):189–207, 1967. ISSN 00223719. doi:10.1088/0022-3719/1/1/322.

[30] C. J. Hearn. Phonon softening and the metal-insulator transition in VO2. *Journal of Physics C: Solid State Physics*, 5:1317–1334, 1972. doi:10.1088/0022-3719/5/12/012.

[31] Volker Eyert. The metal-insulator transitions of VO2: A band theoretical approach. *Annalen der Physik (Leipzig)*, 11(9):650–702, 2002. ISSN 00033804. doi:10.1002/1521-3889(200210)11:9<650::AID-ANDP650>3.0.CO;2-K.

[32] A. Zylbersztejn and N. F. Mott. Metal-Insulator Transition in Vanadium Dioxide. *Physical Review B*, 11(11):4383–4395, 1975. ISSN 0163-1829. doi:10.1103/PhysRevB.11.4383.

[33] Dmitry Ruzmetov, Don Heiman, Bruce B. Claflin, Venkatesh Narayanamurti, and Shriram Ramanathan. Hall carrier density and magnetoresistance measurements in thin-film vanadium dioxide across the metal-insulator transition. *Physical Review B*, 79:153107, 2009. ISSN 10980121. doi:10.1103/PhysRevB.79.153107.

[34] M. Marezio, D. B. McWhan, J. P. Remeika, and P. D. Dernier. Structural Aspects of the Metal-Insulator Transitions

in Cr-Doped VO2. *Physical Review B*, 5(7):2541–2551, 1972. doi:10.1103/PhysRevB.5.2541.

[35] Evgheni Strelcov, Alexander Tselev, Ilia Ivanov, John D. Budai, Jie Zhang, Jonathan Z. Tischler, Ivan Kravchenko, Sergei V. Kalinin, and Andrei Kolmakov. Doping-based stabilization of the M2 phase in free-standing VO2 nanostructures at room temperature. *Nano Letters*, 12 (12):6198–6205, 2012. ISSN 15306984. doi:10.1021/nl303065h.

[36] J. P. Pouget, H. Launois, J. P. D'Haenens, P. Merenda, and T. M. Rice. Electron Localization Induced by Uniaxial Stress in Pure VO2. *Physical Review Letters*, 35(13):873–875, 1975. doi:10.1103/PhysRevLett.35.873.

[37] J. Pouget and H. Launois. Metal-Insulator phase transition in VO2. *Journal de Physique Colloques*, 37:C4, 1976. doi:10.1051/jphyscol:1976408.

[38] T. M. Rice, H. Launois, and J. P. Pouget. Comment on "VO2. Peierls or Mott-Hubbard? A View from Band Theory". *Phys. Rev. Lett.*, 73 (22):3042, 1994. ISSN 0031-9007. doi:10.1103/PhysRevLett.73.3042.

[39] S. Biermann, a. Poteryaev, a. I. Lichtenstein, and a. Georges. Dynamical singlets and correlation-assisted peierls transition in vo 2. *Physical Review Letters*, 94(2):1–4, 2005. ISSN 00319007. doi:10.1103/PhysRevLett.94.026404.

[40] T. C. Koethe, Z. Hu, M. W. Haverkort, C. Schüßler-Langeheine, F. Venturini, N. B. Brookes, O. Tjernberg, W. Reichelt, H. H. Hsieh, H. J. Lin, C. T. Chen, and L. H. Tjeng. Transfer of spectral weight and symmetry across the metal-insulator transition in VO2. *Physical Review Letters*, 97(11):1–4, 2006. ISSN 00319007. doi:10.1103/PhysRevLett.97.116402.

[41] Cedric Weber, David D. O'Regan, Nicholas D. M. Hine, Mike C. Payne, Gabriel Kotliar, and Peter B. Littlewood. Vanadium Dioxide : A Peierls-Mott Insulator Stable against Disorder. *Physical Review Letters*, 108:256402, 2012. doi:10.1103/PhysRevLett.108.256402.

[42] G. B. Stefanovich, A. L. Pergament, and D. G Stefanovich. Electrical switching and Mott transition in VO 2. *Journal of Physics: Condensed Matter*, 12(41):8837–8845, 2000. ISSN 0953-8984. doi:10.1088/0953-8984/12/41/310.

[43] P. P. Boriskov, A. A. Velichko, A. L. Pergament, G. B. Stefanovich, and D. G Stefanovich. The Effect of Electric Field on Metal âĂŞ Insulator Phase Transition in Vanadium Dioxide. *Technical Physics Letters*, 28 (5):406–408, 2002. doi:10.1134/1.1482750.

[44] J. Frenkel. On Pre-Breakdown Phenomena in Insulators and Electronic Semi-Conductors. *Physical Review Letters*, 54:647–648, 1938. doi:10.1103/PhysRev.54.647.

[45] Fu-Chien Chiu. Review Article: A Review on Conduction Mechanisms in Dielectric Films. *Advances in Materials Science and Engineering*, 2014:578168, 2014. doi:10.1155/2014/578168.

[46] A. Cavalleri, Th. Dekorsy, H. H. W. Chong, J. C. Kieffer, and R. W. Schoenlein. Evidence for a structurally-driven insulator-to-metal transition in VO 2: A view from the ultrafast timescale [2]. *Physical Review B - Condensed Matter and Materials Physics*, 70(16):1–4, 2004. ISSN 01631829. doi:10.1103/PhysRevB.70.161102.

[47] A. Pashkin, C. Kuber, H. Ehrke, R. Lopez, A. Halabica, R. F. Jr Haglund, R. Huber, and A. Leitenstorfer. Ultrafast insulator-metal phase transition in VO 2 studied by multiterahertz spectroscopy. *Physical Review B*, 83:195120, 2011. doi:10.1103/PhysRevB.83.195120.

[48] Mengkun Liu, Harold Y Hwang, Hu Tao, Andrew C Strikwerda, Kebin Fan, George R Keiser, Aaron J Sternbach, Kevin G West, Salinporn Kittiwatanakul, Jiwei Lu, Stuart A Wolf, Fiorenzo G Omenetto, Xin Zhang, Keith A Nelson, and Richard D Averitt. Terahertz-field-induced insulator-to-metal transition in vanadium dioxide metamaterial. *Nature*, 487(7407):345–348, 2012. ISSN 0028-0836. doi:10.1038/nature11231.

[49] Brian T O'Callahan, Andrew C Jones, Jae Hyung Park, David H Cobden, Joanna M Atkin, and Markus B Raschke. Inhomogeneity of the ultrafast insulator-to-metal transition dynamics of VO2. *Nature communications*, 6:6849, 2015. ISSN 2041-1723. doi:10.1038/ncomms7849.

[50] Bin Hu, Yong Ding, Wen Chen, Dhaval Kulkarni, Yue Shen, Vladimir V. Tsukruk, and Zhong Lin Wang. External-strain induced insulating phase transition in VO2 nanobeam and its application as flexible strain sensor. *Advanced Materials*, 22(45):5134–5139, 2010. ISSN 09359648. doi:10.1002/adma.201002868.

[51] J. Cao, E. Ertekin, V. Srinivasan, W. Fan, S. Huang, H. Zheng, J. W. L. Yim, D. R. Khanal, D. F. Ogletree, J. C. Grossman, and J. Wu. Strain engineering and one-dimensional organization of metal-insulator domains in single-crystal vanadium dioxide beams. *Nature nanotechnology*, 4(November):732–737, 2009. ISSN 1748-3387. doi:10.1038/nnano.2009.266.

[52] Jiang Wei, Zenghui Wang, Wei Chen, and David H Cobden. New aspects of the metal-insulator transition in single-domain vanadium dioxide nanobeams. *Nature nanotechnology*, 4(7):420–424, 2009. ISSN 1748-3387. doi:10.1038/nnano.2009.141.

[53] Jaewoo Jeong, Nagaphani Aetukuri, Tanja Graf, Thomas D Schladt, Mahesh G Samant, and Stuart S P Parkin. Suppression of Metal-Insulator Transition in Vo2 by Electric Field-Induced Oxygen Vacancy Formation. *Scientific Reports*, 339:1402–1405, 2013. doi:10.1021/acscatal.5b00188.

[54] Xiong Ying, Wen Qi-Ye, Chen Zhi, Tian Wei, Wen Tian-Long, Jing Yu-Lan, Yang Qing-Hui, and Zhang Huai-Wu. Tuning the phase transitions of VO 2 thin films on silicon substrates using ultrathin Al 2 O 3 as buffer layers. *Journal of Physics D: Applied Physics*, 47(45):455304, 2014. ISSN 0022-3727. doi:10.1088/0022-3727/47/45/455304.

[55] Kenichi Miyazaki, Keisuke Shibuya, Megumi Suzuki, Hiroyuki Wado, and Akihito Sawa. Correlation between thermal hysteresis width and broadening of metal-insulator transition in Cr- and Nb-doped VO2 films. *Japanese Journal of Applied Physics*, 53(7), 2014. ISSN 13474065. doi:10.7567/JJAP.53.071102.

[56] Kenichi Miyazaki, Keisuke Shibuya, Megumi Suzuki, Kenichi Sakai, Jun Ichi Fujita, and Akihito Sawa. Chromium-niobium co-doped vanadium dioxide films: Large temperature coefficient of resistance and practically no thermal hysteresis of the metal-insulator transition. *AIP Advances*, 6(5), 2016. ISSN 21583226. doi:10.1063/1.4949757.

[57] Dmitry Ruzmetov, Kevin T. Zawilski, Venkatesh Narayanamurti, and Shriram Ramanathan. Structure-functional property relationships in rf-sputtered vanadium dioxide thin films. *Journal of Applied Physics*, 102:113715, 2007. ISSN 00218979. doi:10.1063/1.2817818.

[58] Yong Zhao, Joon Hwan Lee, Yanhan Zhu, M. Nazari, Changhong Chen, Haiyan Wang, Ayrton Bernussi, Mark Holtz, and Zhaoyang Fan. Structural, electrical, and terahertz transmission properties of VO 2 thin films grown on c-, r-, and m-plane sapphire substrates. *Journal of Applied Physics*, 111(5), 2012. ISSN 00218979. doi:10.1063/1.3692391.

[59] Y. Muraoka and Z. Hiroi. Metal-insulator transition of VO2 thin films grown on TiO 2 (001) and (110) substrates. *Applied Physics Letters*, 80(4):583–585, 2002. ISSN 00036951. doi:10.1063/1.1446215.

[60] Z. Yang, C. Ko, and S. Ramanathan. Metal-insulator transition characteristics of VO2 thin films grown on Ge(100) single crystals. *Journal of Applied Physics*, 108(073708):1–6, 2010. ISSN 00218979. doi:10.1063/1.3492716.

[61] Hyojin Yoon, Minseok Choi, Tae-won Lim, Hyunah Kwon, Kyu-wook Ihm, Jong Kyu Kim, Si-young Choi, and Junwoo Son. Reversible phase modulation and hydrogen storage in multivalent VO 2 epitaxial thin films. *Nature materials*, 15(July):1113–1120, 2016. doi:10.1038/NMAT4692.

[62] Asmaa Leila Sabeha Hassein-Bey, Hakim Tahi, and Amina Zouina Djafer-Ait. Substrate Effect on Electrical Properties of Vanadium Oxide Thin Film for Memristive Device Applications. *IEEE*, pages 240–243, 2016. doi:10.1109/SMELEC.2016.7573636.

[63] T. T. Lv, Y. X. Li, H. F. Ma, Z. Zhu, Z. P. Li, C. Y. Guan, J. H. Shi, H. Zhang, and T. J. Cui. Hybrid metamaterial switching for manipulating chirality based on VO2 phase transition. *Scientific Reports*, 6 (November 2015):23186, 2016. ISSN 2045-2322. doi:10.1038/srep23186.

[64] L. L. Fan, S. Chen, Y. F. Wu, F. H. Chen, W. S. Chu, X. Chen, C. W. Zou, and Z. Y. Wu. Growth and phase transition characteristics of pure M-phase VO2 epitaxial film prepared by oxide molecular beam epitaxy. *Applied Physics Letters*, 103(13), 2013. ISSN 00036951. doi:10.1063/1.4823511.

[65] Shi Chen, Xi Jun Wang, Lele Fan, Guangming Liao, Yuliang Chen, Wangsheng Chu, Li Song, Jun Jiang, and Chongwen Zou. The Dynamic Phase Transition Modulation of Ion-Liquid Gating VO2 Thin Film: Formation, Diffusion, and Recovery of Oxygen Vacancies. *Advanced Functional Materials*, 26(20):3532–3541, 2016. ISSN 16163028. doi:10.1002/adfm.201505399.

[66] Hyun-Tak Kim, Byung-Gyu Chae, Doo-Hyeb Youn, Gyungock Kim, Kwang-Yong Kang, Seung-Joon Lee, Kwan Kim, and Yong-Sik Lim. Raman study of electric-field-induced first-order metal-insulator transition in VO[sub 2]-based devices. *Applied Physics Letters*, 86:242101, 2005. ISSN 00036951. doi:10.1063/1.1941478.

[67] Hyun Tak Kim, Yong Wook Lee, Bong Jun Kim, Byung Gyu Chae, Sun Jin Yun, Kwang Yong Kang, Kang Jeon Han, Ki Ju Yee, and Yong Sik Lim. Monoclinic and correlated metal phase in VO2 as evidence of the mott transition: Coherent phonon analysis. *Physical Review Letters*, 97:266401, 2006. ISSN 00319007. doi:10.1103/PhysRevLett.97.266401.

[68] Bong-jun Kim, Yong Wook Lee, Sungyeoul Choi, Jung-wook Lim, Sun Jin Yun, Hyun-tak Kim, Tae-Ju Shin, and Hwa-Sick Yun. Micrometer x-ray diffraction study of VO 2 films : Separation between metal-insulator transition and structural phase transition. *Physical Review B*, 77:235401, 2008. doi:10.1103/PhysRevB.77.235401.

[69] Zhensheng Tao, Tzong-Ru Han, Subhendra Mahanti, Phillip Duxbury, Fei Yuan, Chong-Yu Ruan, Kevin Wang, and Junqiao Wu. Decoupling of Structural and Electronic Phase Transitions in VO2. *Physical Review Letters*, 109:166406, 2012. ISSN 0031-9007. doi:10.1103/PhysRevLett.109.166406.

[70] A. S. Barker Jr, H. W. Verleur, and H. J. Guggenheim. Infrared Optical Properties of Vanadium Dioxide Above and Below the Transition Temperature. *Physical Review Letters*, 17(26):1286–1289, 1966. ISSN 0031-9007. doi:10.1103/PhysRevLett.17.1286.

[71] M. M. Qazilbash, M. Brehm, B.G. Chae, P.-C. Ho, G. O. Andreev, B.J. Kim, S.Y. Yun, A. V. Balatsky, M. B. Maple, F. Keilmann, H.T. Kim, and D. N. Basov. Mott Transition in VO2 Revealed by Infrared Red Spectroscopy and Nano-imaging. *Science*, 318(December):1750–1753, 2007. ISSN 1095-9203. doi:10.1126/science.1150124.

[72] A. Frenzel, M. M. Qazilbash, M. Brehm, Byung-gyu Chae, Bong-jun Kim, Hyun-tak Kim, A. V. Balatsky, F. Keilmann, and D. N. Basov. Inhomogeneous electronic state near the insulator-to-metal transition in the correlated oxide VO 2. *Physical Review B*, 80(115115):1–7, 2009. doi:10.1103/PhysRevB.80.115115.

[73] Amos Sharoni, Juan Gabriel Ramirez, and Ivan K. Schuller. Multiple avalanches across the metal-insulator transition of vanadium oxide nanoscaled junctions. *Physical Review Letters*, 101(2):4–7, 2008. ISSN 00319007. doi:10.1103/PhysRevLett.101.026404.

[74] J. G. Ramírez, A. Sharoni, Y. Dubi, M. E. Gómez, and Ivan K. Schuller. First-order reversal curve measurements of the metal-insulator transition in VO2: Signatures of persistent metallic domains. *Physical Review B*, 79:235110, 2009. ISSN 10980121. doi:10.1103/PhysRevB.79.235110.

[75] M. M. Qazilbash, A. Tripathi, A. A. Schafgans, Bong-jun Kim, Hyun-tak Kim, Zhonghou Cai, M. V. Holt, J. M. Maser, F. Keilmann, O. G. Shpyrko, and D. N. Basov. Nanoscale imaging of the electronic and structural transitions in vanadium dioxide. *Physical Review B*, 83: 165108, 2011. doi:10.1103/PhysRevB.83.165108.

[76] Larry A. Ladd and William Paul. Optical and Transport Properties of High Quality Crystals of V2O4 Near the Metallic Transition temperature. *Solid State Communications*, 7(4):425–428, 1969. ISSN 00381098. doi:10.1016/0038-1098(69)90888-6.

[77] Changhyun Ko and Shriram Ramanathan. Dispersive capacitance and conductance across the phase transition boundary in metal-vanadium oxide-silicon devices. *Journal of Applied Physics*, 106(3):034101, 2009. ISSN 00218979. doi:10.1063/1.3186024.

[78] P. J. Hood and J. F. Denatale. Millimeter-wave dielectric properties of epitaxial vanadium dioxide thin films. *Journal of Applied Physics*, 70(1):376–381, 1991. ISSN 00218979. doi:10.1063/1.350285.

[79] H R Philipp. Optical Properties of Non-Crystalline Si, SiO, SiOx and SiO2. *Journal of Physics and Chemistry of Solids*, 32:1935–1945, 1971. doi:10.1016/S0022-3697(71)80159-2.

[80] Kevin J Yang and Chenming Hu. MOS Capacitance Measurements for High-Leakage Thin Dielectrics. *IEEE Transactions on Electron Devices*, 46(7):1500–1501, 1999. doi:10.1109/16.772500.

[81] E. L. Murphy and R. H. Good. Thermionic Emission, Field Emission, and the Transition Region. *Physical Review*, 102(6):1464–1473, 1956. ISSN 0031899X. doi:10.1103/PhysRev.102.1464.

[82] Jeremy M. Beebe, Bongsoo Kim, J. W. Gadzuk, C. Daniel Frisbie, and James G. Kushmerick. Transition from direct tunneling to field emission in metal-molecule-metal junctions. *Physical Review Letters*, 97(2):1–4, 2006. ISSN 00319007. doi:10.1103/PhysRevLett.97.026801.

[83] John G. Simmons. Generalized Formula for the Electric Tunnel Effect between Similar Electrodes Separated by a Thin Insulating Film. *Journal of Applied Physics*, 34(6):1793–1803, 1963. ISSN 00218979. doi:10.1063/1.1702682.

[84] P Rottländer, M Hehn, and A Schuhl. Determining the interfacial barrier height and its relation to tunnel magnetoresistance. *Physical Review B*, 65:054422, 2002. ISSN 0163-1829. doi:10.1103/PhysRevB.65.054422.

[85] Dong Yu, Congjun Wang, Brian L. Wehrenberg, and Philippe Guyot-Sionnest. Variable range hopping conduction in semiconductor nanocrystal solids. *Physical Review Letters*, 92:216802, 2004. ISSN 00319007. doi:10.1103/PhysRevLett.92.216802.

[86] Harry L. Tuller. Ionic conduction in nanocrystalline materials. *Solid State Ionics*, 131:143–157, 2000. doi:10.1016/S0167-2738(00)00629-9.

[87] Fu-Chien Chiu, Hong-Wen Chou, and Joseph Ya-min Lee. Electrical conduction mechanisms of metalâĹŢLa2O3âĹŢSi structure. *Journal of Applied Physics*, 97(10):103503, 2005. ISSN 0021-8979. doi:10.1063/1.1896435.

[88] Changhyun Ko, Zheng Yang, and Shriram Ramanathan. Work Function of Vanadium Dioxide Thin Films Across the Metal-Insulator Transition and the Role of Surface Nonstoichiometry. *ACS Applied Materials & Interfaces*, 3(9):3396–3401, 2011. ISSN 1944-8244. doi:10.1021/am2006299.

[89] A B Petrin. Thermionic field emission of electrons from metals and explosive electron emission from micropoints. *Journal of Experimental and Theoretical Physics*, 109(2):314–321, 2009. ISSN 1063-7761. doi:10.1134/S1063776109080184.

[90] Seid Sadat, Aaron Tan, Yi Jie Chua, and Pramod Reddy. Nanoscale thermometry using point contact thermocouples. *Nano Letters*, 10(7):2613–2617, 2010. ISSN 15306984. doi:10.1021/nl101354e.

[91] Kyeongtae Kim, Wonho Jeong, Woochul Lee, and Pramod Reddy. Ultra-High Vacuum Scanning Thermal Microscopy for Nanometer Resolution Quantitative Thermometry. *ACS Nano*, 6(5):4248–4257, 2012. doi:10.1021/nn300774n.

[92] Lionel Aigouy, Gilles Tessier, Michel Mortier, and Benoît Charlot. Scanning thermal imaging of microelectronic circuits with a fluorescent nanoprobe. *Applied Physics Letters*, 87:184105, 2005. doi:10.1063/1.2123384.

[93] J. S. Reparaz, E. Chavez-Angel, M. R. Wagner, B. Graczykowski, J. Gomis-Bresco, F. Alzina, and C. M. Sotomayor Torres. A novel contactless technique for thermal conductivity determination: Two-laser Raman thermometry. *Review of Scientific Instruments*, 85:034901, 2014. ISSN 10897623. doi:10.1063/1.4867166.

[94] Matthew Mecklenburg, William A Hubbard, E R White, Rohan Dhall, Stephen B Cronin, Shaul Aloni, and B C Regan. Nanoscale temperature mapping in operating microelectronic devices. *Science*, 347:629–633, 2015. ISSN 0036-8075. doi:10.1126/science.aaa2433.

[95] D. Teyssieux, L. Thiery, and B. Cretin. Near-infrared thermography using a charge-coupled device camera: Application to microsystems. *Review of Scientific Instruments*, 78:034902, 2007. ISSN 00346748. doi:10.1063/1.2714040.

[96] G Tessier, M Bardoux, C Boué, C Filloy, and D Fournier. Back side thermal imaging of integrated circuits at high spatial resolution. *Applied Physics Letters*, 90:171112, 2007. doi:10.1063/1.2732179.

[97] Seunghyup Lee, Heejin Kim, Dong-Jin Yun, Shi-Woo Rhee, and Kijung Yong. Resistive switching characteristics of ZnO thin film grown on stainless steel for flexible nonvolatile memory devices. *Applied Physics Letters*, 95(26):262113, 2009. ISSN 00036951. doi:10.1063/1.3280864.

[98] Fabian Menges, Philipp Mensch, Heinz Schmid, Heike Riel, Andreas Stemmer, and Bernd Gotsmann. Temperature mapping of operating nanoscale devices by scanning probe thermometry. *Nature Communications*, 7:10874, 2016. ISSN 2041-1723. doi:10.1038/ncomms10874.

[99] G Kucsko, P C Maurer, N Y Yao, M Kubo, H J Noh, P K Lo, H Park, and M D Lukin. Nanometre-scale thermometry in a living cell. *Nature*, 500(7460):54–8, 2013. ISSN 1476-4687. doi:10.1038/nature12373.

[100] P. Neumann, I. Jakobi, F. Dolde, C. Burk, R. Reuter, G. Waldherr, J. Honert, T. Wolf, A. Brunner, J. H. Shim, D. Suter, H. Sumiya, J. Isoya, and J. Wrachtrup. High-precision nanoscale temperature sensing using single defects in diamond. *Nano Letters*, 13(6):2738–2742, 2013. ISSN 15306984. doi:10.1021/nl401216y.

[101] D. M. Toyli, D. J. Christle, A. Alkauskas, B. B. Buckley, C. G. Van de Walle, and D. D. Awschalom. Measurement and control of single nitrogen-vacancy center spins above 600 K. *Physical Review X*, 2(3): 1–7, 2012. ISSN 21603308. doi:10.1103/PhysRevX.2.031001.

[102] D. Halbertal, J. Cuppens, M. Ben Shalom, L. Embon, N. Shadmi, Y. Anahory, H. R. Naren, J. Sarkar, A. Uri, Y. Ronen, Y. Myasoedov, L. S. Levitov, E. Joselevich, A. K. Geim, and E. Zeldov. Nanoscale thermal imaging of dissipation in quantum systems. *Nature*, 539(7629): 407–410, 2016. ISSN 0028-0836. doi:10.1038/nature19843.

[103] Wen-Yuan Chang, Yen-Chao Lai, Tai-Bor Wu, Sea-Fue Wang, Frederick Chen, and Ming-Jinn Tsai. Unipolar resistive switching characteristics of ZnO thin films for nonvolatile memory applications. *Applied Physics Letters*, 92:022110, 2008. doi:10.1063/1.2834852.

[104] Si Yun Park, Beom Joon Kim, Kyongjun Kim, Moon Sung Kang, Keon-hee Lim, Tae Il Lee, Jae M Myoung, Hong Koo Baik, Jeong Ho Cho, and Youn Sang Kim. Low-Temperature , Solution-Processed and Alkali Metal Doped ZnO for High-Performance Thin-Film Transistors. *Advanced Materials*, 24:834–838, 2012. doi:10.1002/adma.201103173.

[105] Steven K. Hau, Hin Lap Yip, Nam Seob Baek, Jingyu Zou, Kevin O'Malley, and Alex K Y Jen. Air-stable inverted flexible polymer solar cells using zinc oxide nanoparticles as an electron selective layer. *Applied Physics Letters*, 92:253301, 2008. ISSN 00036951. doi:10.1063/1.2945281.

[106] Ee Wah Lim and Razali Ismail. Conduction Mechanism of Valence Change Resistive Switching Memory: A Survey. *Electronics*, 4:586–613, 2015. doi:10.3390/electronics4030586.

[107] S.M. Lee and David G Cahill. Heat transport in thin dielectric films. *Journal of Applied Physics*, 81(6):2590–2595, 1997. ISSN 00218979. doi:10.1063/1.363923.

[108] Ruxandra Costescu, Marcel Wall, and David Cahill. Thermal conductance of epitaxial interfaces. *Physical Review B*, 67(5):54302, 2003. ISSN 0163-1829. doi:10.1103/PhysRevB.67.054302.

[109] O W Käding, H Skurk, and K E Goodson. Thermal conduction in metallized silicon-dioxide layers on silicon. *Applied Physics Letters*, 65 (1629):1629–1631, 1994. doi:10.1063/1.112933.

[110] V. N. Andreev, F. A. Chudnovskii, A. V. Petrov, and E. I. Terukov. Thermal conductivity of VO2, V3O5, and V2O3. *Physica Status Solidi (a)*, 48(2):K153–K156, 1978. ISSN 1521396X. doi:10.1002/pssa.2210480257.

Appendix A

Power Gradient

As previously stated, in the temperature map (Fig. 3.7) and more pronounced in the electric field map (Fig. 3.1), that the bottom third of the image requires a higher voltage to cause the transition. These pixels also display a larger voltage and current at the transition (Fig. A.1).

We compute the energy input $E_{\text{in}} = \int I \cdot V dt$ across the map (Fig. A.2 (a)), and we find that approximately double the energy is input into the film in the bottom third of the image than at the top two thirds. The calculated temperature follows the same pattern, but the difference between the top and bottom of the image is only ~ 5 K, or less than a 2 % change over the image. We hypothesize that a slightly varying thickness or composition of the SiO_x interface would increase the amount of Joule heating energy leaked from the VO_2 film to the substrate and would explain how a higher voltage and current is required to cause the transition in the lower portion of the image. Here, we calculate the input energy from the tip, the energy required to cause a transition in VO_2, and the energy leaked into a thin SiO_2 interface and determine that a thickness change of 1 nm in the SiO_2 interface could result in the energy input change observed.

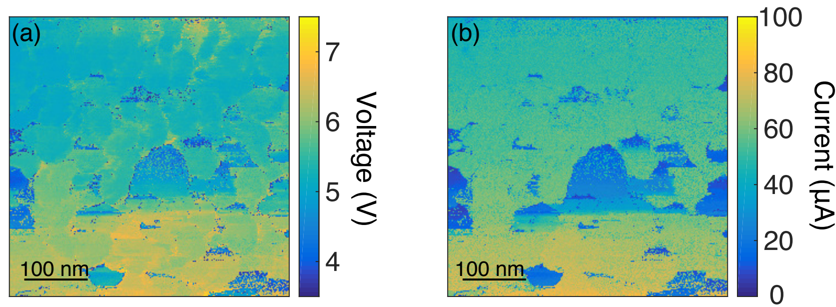

Figure A.1: Map showing the voltage (a) and current (b) through the film at the transition.

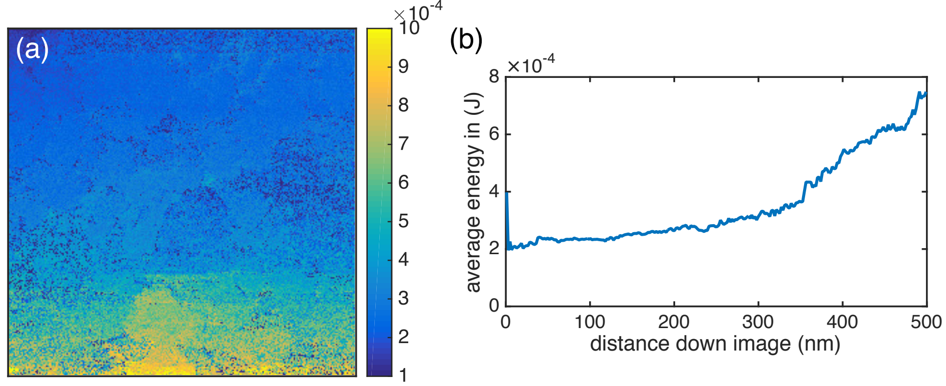

Figure A.2: (a) Map showing the energy input to the film through the tip. (b) The average energy per row input to the film through the tip.

A.1 Input energy from tip

The first step is to calculate the energy put into the film to cause the transition. We are interested in the energy input into the film, so the corrected voltage through the film is used for the calculation, not the applied voltage. The data points are sufficiently close to calculate the input power as the sum of rectangles of width ΔV, and height I. To calculate the energy we then multiply by the time taken for the film to transition. The total time is $t \approx 0.0180$ s, calculated by multiplying the number of steps before the transition (180 for the representative pixel analyzed in this section) and the step time, $\Delta t = 10^{-4}$ s. The energy input is

$$\begin{aligned} E &= \left[\sum_i I(i) \cdot V_{\text{film}}(i)\right] \cdot \Delta t \cdot 180 \\ &= \left[\sum_i I(i) \cdot V_{\text{film}}(i)\right] \cdot 0.018\text{s} \\ &\approx 3.5 \times 10^{-4} \text{ J} \end{aligned} \tag{A.1}$$

for a representative pixel in the top half of the film.

Using this method, the average energy input in of the first two thirds of the map is 2.65×10^{-4} J, and the average for the bottom third is 5.52×10^{-4} J. There's an average of about 3×10^{-4} J of extra energy needed to cause the transition at the bottom of the image. A map of the calculated input energy is shown in Fig. A.2, with the average input per row shown in panel

(b). In panel (b) the distinct change from $\sim 2.5 \times 10^{-4}$ J to $\sim 5.5 \times 10^{-4}$ J about two thirds of the way down the map can be seen.

A.2 Heat required to cause IMT in VO_2

The specific heat of VO_2 near room temperature is $C = 690$ J/(kg K)[20], and increases up to ~ 750 J/(kg K) before the transition [28]. We use the specific heat immediately preceding the transition to calculate an upper bound for the total energy

$$\Delta E = m_{\text{grain}} C \Delta T = \rho_{\text{VO}_2} V_{\text{grain}} C \Delta T. \tag{A.2}$$

Using a grain diameter of 72 nm, a film thickness of 187 nm, the density of VO_2 in the insulating state of 4571 kg/m^2, and a ΔT of 42 K, gives $\Delta E \sim 1 \times 10^{-13}$ J. This result indicates that almost none of the energy input by the tip is actually required to cause the transition in a single VO_2 grain, and implies that the energy is going elsewhere, nominally through the SiO_x interface and into the substrate, or diffusing into neighboring VO_2 grains.

A.3 Thermal Conductivity of SiO_2

The thermal conductivity, κ, is defined as the constant of proportionality between the power dQ/dt, per contact area A, and the thermal gradient $\Delta T/\Delta x$,

$$\frac{dQ}{dt}\frac{1}{A} = \kappa \frac{\Delta T}{\Delta x}. \tag{A.3}$$

Lee *et. al* measured the thermal conductivity of SiO_2 films grown by plasma-enhanced chemical vapor deposition (PECVD) on Si substrates using the 3ω method, which can be used to both heat and monitor the temperature of the surface of a film. They patterned a heater/thermometer line onto the surface of the films using photolithography and wet chemical etching, the result of which is shown in the inset of Fig. A.3. Their SiO_2 films ranged in thickness from 32 nm to 190 nm, and in a temperature from 80 K to 300 K [107]. Lee modeled the apparent thermal conductivity of thin film SiO_2 at 300 K using the equation

$$\kappa_{\text{d}} = \frac{\kappa_{\text{i}}}{1 + R_{\text{i}} \kappa_{\text{i}}/d} \tag{A.4}$$

where κ_d is the thickness dependent apparent thermal conductivity, κ_i is the intrinsic thermal conductivity, R_i is the interface thermal conductance and d is the thickness of the film. Using this model along with Lee *et. al*'s [107], Costescu *et. al*'s [108], and Käding *et. al*'s [109] data for amorphous thin film SiO_2 at 300 K, we fit the apparent thermal conductivity for SiO_2. We show the three data sets and the fit (red data points) in Fig. A.3. We vary both the intrinsic thermal conductivity and the interface thermal conductance fit the data, and find $\kappa_\mathrm{i} = 0.9$ W/m·K and $R_\mathrm{i} = 0.9 \times 10^{-9}$ m^2·K/W. The intrinsic thermal conductivity of SiO_2 grown by ion beam sputtering has a known value of 1.1 W/m·K, which is comparable to our fit value. Lee *et. al* fit the interface thermal conductance to be $\sim 2 \times 10^{-8}$ m^2·K/W. Our fit R_i is an order of magnitude smaller due to considering other measurements at lower thicknesses.

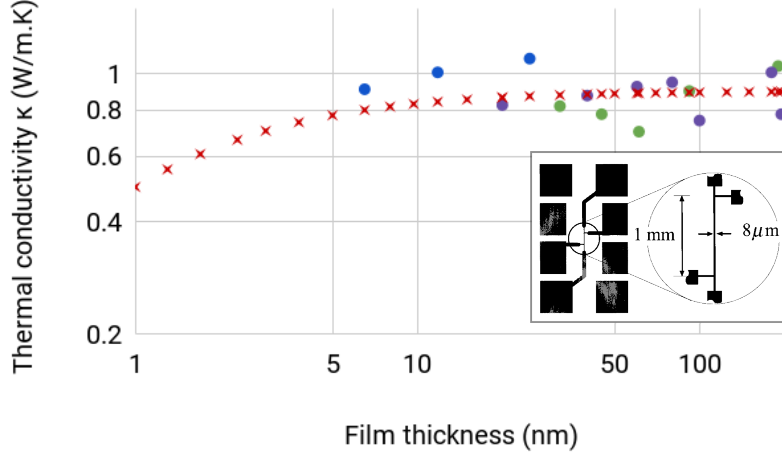

Figure A.3: Fit SiO_2 thermal conductivity κ as a function of film thickness (red crosses) from Lee *et. al* (purple) [107], Costescu *et. al* (blue) [108], and Käding *et. al* (green) [109]. Inset: Pattern for the heater/thermometer line and contact pads are patterned using photolithography and wet chemical etching. The data was fit to Eq. A.4, from Lee *et. al*.

To calculate the energy lost through the SiO_2 interface, we must approximate the instantaneous temperature of the film, and the time spent at each temperature. Using a 5-point approximation of the PF slope, then using the slope to estimate the temperature, we calculate the temperature at each voltage. Figure A.4 shows the estimated film temperature based on the estimated PF slope and film thickness 187 nm for each voltage through the film. We assume that the film starts at room temperature, and any result below 293 K is a consequence of applying the PF fit to a region where it was not the dominant mechanism. We notice that the film warms quickly at first, and spends most of the ramp time at 335 K. The approximate thermal energy lost through the SiO_2 interface is

$$\Delta Q = \frac{\kappa_{\mathrm{d}} \cdot A}{d_{\mathrm{i}}} \Delta T \Delta t, \tag{A.5}$$

where κ_d is the thickness dependent apparent thermal conductivity, A is the contact area, d_{i} is the interface thickness, ΔT is the change in temperature, and Δt is the time the thermal gradient is maintained. As an upper bound we take the temperature difference to be 42 K, since the film temperature increases quickly from 293 K to 335 K. To estimate the time the thermal

gradient is maintained, we notice the transition occurs approximately 0.0195 s after the voltage starts ramping. From figure A.4, we estimate the film only starts to warm around 2 V or approximately 4 ms, so $\Delta t = 0.0175$ s.

Approximating the thermal conductivity of SiO_x as that of SiO_2, and using the contact area of the grain the energy leaked through the 2 nm thick interfacial layer is calculated to be about 7.9 $\times 10^{-7}$ J. The heat leaked through the SiO_x layer is three orders of magnitude smaller than the calculated energy input into the film.

For a more accurate description we assume that the current warms an area larger than that of one grain via an amorphous VO_x layer, which is nominally conducting at and above room temperature so it does not alter the effective circuit diagram or data correction. We model the two interfacial oxide layers as two insulators. The thermal resistances of the two interface layers are added in series,

$$\frac{\kappa_{\text{eff}}}{d_{\text{eff}} A_{\text{eff}}} = (R_{\text{SiO}_x} + R_{\text{VO}_x})^{-1} = \left(\frac{d_{\text{SiO}_x}}{\kappa_{\text{SiO}_x} A_{\text{SiO}_x}} + \frac{d_{\text{VO}_x}}{\kappa_{\text{VO}_x} A_{\text{VO}_x}} \right)^{-1}. \tag{A.6}$$

The area is the same for both layers, therefore the effective $\kappa_{\text{eff}}/d_{\text{eff}}$ is calculated as a function of SiO_x thickness using

$$\frac{\kappa_{\text{eff}}}{d_{\text{eff}}} = \left(\frac{d_{\text{SiO}_x}}{\kappa_{\text{SiO}_x}} + \frac{d_{\text{VO}_x}}{\kappa_{\text{VO}_x}} \right)^{-1}. \tag{A.7}$$

The VO_x layer is assumed to be 5 Å, and the thermal conductivity is taken to be about 5 W/ m$\cdot$ K [110]. The interface layer with the smaller thermal conductivity and larger thickness will dominate when adding, so we do not vary the VO_x thickness since it will affect the effective κ/d very little. For one grain, this correction still produces a low energy leak, $\sim 7.7 \times 10^{-7}$ J.

We've assumed that the contact area is that of a single grain and that there is no lateral heat leakage. If instead we consider that the heated area is equivalent to 400 individual grains ($\sim$1.4 μm square area), we calculate that the energy leak is on the order of 10^{-4} J. The energy leak as a function of SiO_2 thickness for 400 grains is shown in Fig. A.5.

We see that a small change in SiO_x interface thickness ($\gtrsim$ 1 nm) can change the thermal energy leak on the order of 3×10^{-4} J, which we observe across the image in Fig. A.2 (a). We conclude that if the SiO_x layer is thinner on the bottom third of the map than the top on the order of a nm, then it will leak more thermal energy, which would in turn require more energy input to the film before the VO_2 transitions.

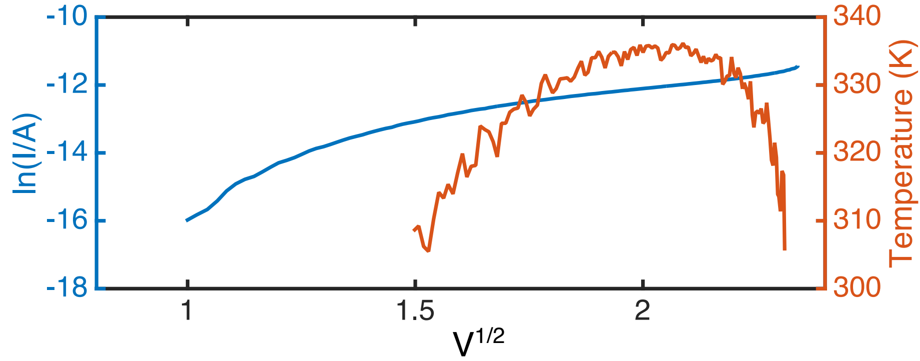

Figure A.4: Approximation of the temperature (red) using a sweeping PF slope on the IV data (blue).

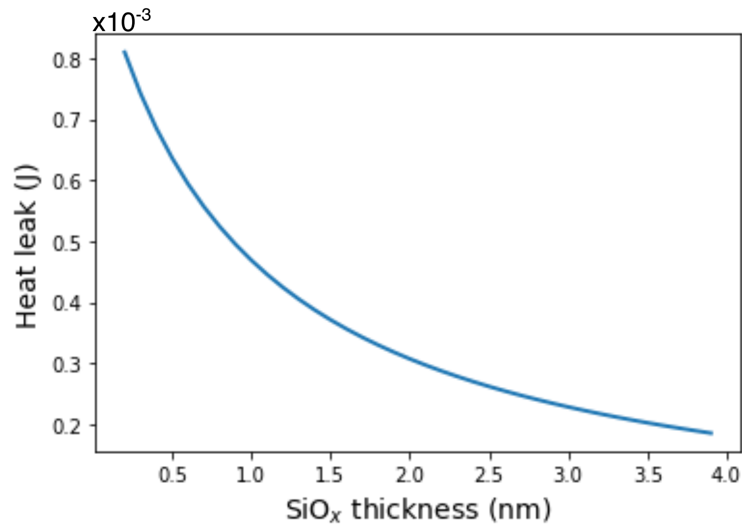

Figure A.5: Energy leaked through the SiO_2 interface as a function of SiO_2 thickness assuming a 5 Å layer of VO_x, and that heat diffuses through a 1.4 μm square area.

Appendix B

Uncertainty in the calculated Temperature

To calculate the uncertainty of the temperature T, we use uncertainties associated with the film thickness d, the PF fit P, and the dielectric constant ϵ_V, and propagate uncertainty. Since the dielectric constant is a function of temperature we must propagate the uncertainty for an implicit expression. We collect the varying parameters and set it equal to the fundamental constants. Writing ε_{V} in terms of its parameters (Eq. 2.2), a, b, and c, and write

$$T \cdot P \cdot d^{1/2} \cdot (a + b \cdot e^{(T-273.15)/c})^{1/2} = \frac{e^{3/2}}{(\pi\varepsilon_0)^{1/2} k_B}. \tag{B.1}$$

For simplicity, combine the fundamental constants into one constant,

$$K \equiv \frac{e^{3/2}}{(\pi\varepsilon_0)^{1/2} k_B}. \tag{B.2}$$

Writing the parameters as a function, f,

$$f(T, P, d, a, b, c) = T \cdot P \cdot d^{1/2} \cdot (a + b \cdot e^{(T-273.15)/c})^{1/2} = K \tag{B.3}$$

where five of the variables (a, b, c, d, P) have known uncertainties, and we want to calculate the uncertainty of the sixth, T.

To confirm implicit uncertainty propagation, consider the simpler example of $z(x, y) = k/xy$, where x and y are variables and k is a constant. From the usual propagation of uncertainty, we know that

$$\delta z^2 = \left(\frac{\partial z}{\partial x}\right)^2 \delta x^2 + \left(\frac{\partial z}{\partial y}\right)^2 \delta y^2. \tag{B.4}$$

$$\delta z^2 = \left(\frac{-k}{x^2 y}\right)^2 \delta x^2 + \left(\frac{-k}{x y^2}\right)^2 \delta y^2 = z^2 \left(\frac{\delta x^2}{x^2} + \frac{\delta y^2}{y^2}\right). \tag{B.5}$$

If instead we represent this equation as $zxy = k$, we can still use Eq. B.4 even if there is no explicit function for z, by defining the function $g = g(x, y, z) = zxy$, and using the fact that

$$\left|\frac{\partial z}{\partial x}\right| = \left|\frac{\partial g}{\partial x}\right| / \left|\frac{\partial g}{\partial z}\right|. \tag{B.6}$$

Equation B.4 then becomes

$$\delta z^2 = \left(\frac{\partial g}{\partial x} / \frac{\partial g}{\partial z}\right)^2 \delta x^2 + \left(\frac{\partial g}{\partial y} / \frac{\partial g}{\partial z}\right)^2 \delta y^2, \tag{B.7}$$

and taking the partial derivatives gives,

$$\delta z^2 = \left(\frac{zy}{xy}\right)^2 \delta x^2 + \left(\frac{zx}{xy}\right)^2 \delta y^2 = z^2 \left(\frac{\delta x^2}{x^2} + \frac{\delta y^2}{y^2}\right). \tag{B.8}$$

We produce the same expression for the uncertainty of z. We now apply this method to our temperature expression given by Eq. B.3 to calculate δT,

$$\delta T^2 = \sum_{\alpha} \left(\frac{\partial f}{\partial \alpha} / \frac{\partial f}{\partial T}\right)^2 \delta \alpha^2, \quad \alpha = a, b, c, d, P. \tag{B.9}$$

We can now calculate the temperature uncertainty at each pixel, but we first quantify δa, δb, δc, δd, and δP.

B.1 Dielectric contant, $\varepsilon_{\mathbf{V}}(T)$

The uncertainty of the dielectric constant is calculated using the standard error values associated with each fit parameter. To check these are reasonable uncertainties we self-consistently use the temperature uncertainty and calculate the associated uncertainty of ε_{V}. The uncertainty of ε_{V}, using temperature in Kelvin is given by

$$\begin{aligned} \delta\varepsilon_{\mathrm{V}}^2 &= \delta a^2 + (e^{(T-273.15)/c})^2 \delta b^2 \\ &+ \left(\frac{b}{c^2}(T - 273.15) e^{(T-273.15)/c}\right)^2 \delta c^2 + \left(\frac{b}{c} \cdot e^{(T-273.15)/c}\right)^2 \delta T^2. \end{aligned} \tag{B.10}$$

If we assume the the standard error stated above (Eq. 2.3), and a temperature uncertainty of 0.1 K, the uncertainty of the dielectric constant is calculated to be less than 1 for temperatures under 313 K, 1.4 for the measurement at 323 K, 2.5 the measurement at 328 K, and 4.4 for the measurement at 333 K. Ko has reported errors of approximately 1 for each of the

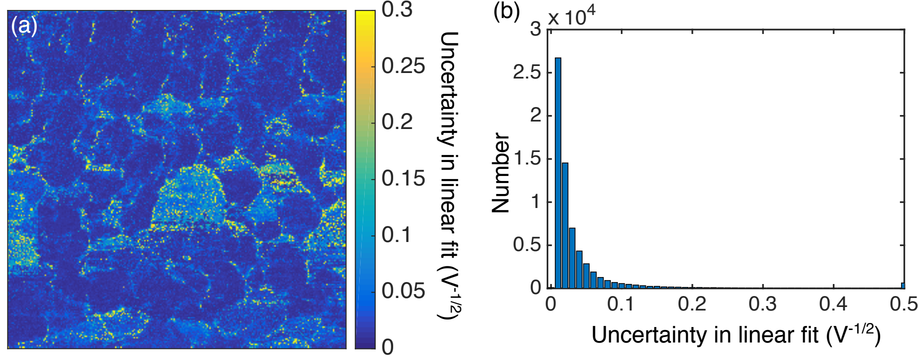

Figure B.1: (a) The uncertainty at each point in the map from performing a linear fit on the IV data. (b) The corresponding histogram.

data points. The uncertainty of ε_{V} calculated using the standard deviation of our fitting function and a generic uncertainty in the temperature of about 1K is higher than the reported error for the data closest to the transition, and on the same order of magnitude or smaller for the lower values. Therefore the uncertainty in the parameters a, b, and c are conservative errors for temperatures greater than 323 K, which is the calculated temperature range.

B.2 Thickness, d

The largest source of uncertainty in the thickness stems from measuring the average overall thickness. The uncertainty in the average thickness comes from the possibility that the TEM image and IV curves may be taken on different regions of the sample with different average thickness. We assume a constant uncertainty of $\delta d = 5$ nm.

B.3 PF slope, P

When calculating the PF slopes we concurrently calculate the error associated with fitting a straight line to the data. A map of the uncertainty due to the linear fit is shown in Fig. B.1, with corresponding histogram.

To estimate the uncertainty from varying the PF fitting region, we find a representative slope that gives a reasonable estimate of the PF slope had no minimizing been done. Since the data is slightly ‘S’-shaped, we know the PF mechanism does not dominate for all applied voltages. During the fitting we define a minimum voltage the start point can be, defined by the approximate

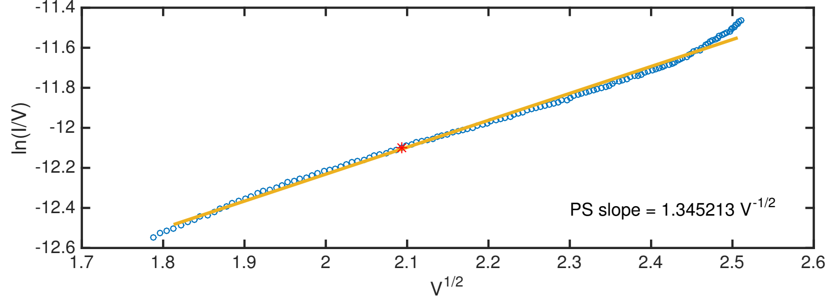

Figure B.2: A representative curve, with the maximum domain PF slope. The voltage range shown is the largest region considered that could possibly be dominated by the PF mechanism

minimum electric field for PF dominated conduction. From Sect. 2.4, PF effect has been observed down to ~ 15 MV/m. For an average film thickness of 187 nm, the minimum applied voltage we expect the PF conduction to dominate is ~ 2.8 V. The maximum value of the endpoint of the fit region is constrained by the position of the jump. The slope obtained by fixing the endpoints to their maximum values is defined as the maximum domain PF slope, and a representative IV curve is shown in Fig. B.2. Fig. B.3 shows the maximum domain PF slope at each point on the map along with histogram in panel (b). We compare the minimized PF slopes and the maximum domain PF slopes by comparing histograms (Fig. B.4). As expected the histogram of minimized PF slope is slightly narrower and translated to lower values in relation to the maximum domain PF slope.

The uncertainty due to allowing both endpoints to vary is the difference between the minimized PF slope and the maximum domain PF slope. This uncertainty is shown in Fig. B.5, with histogram in panel (b).

The total uncertainty in the used PF slope at each point on the map is calculated by combining in quadrature the uncertainty from fitting a linear line and the uncertainty from allowing the endpoints to vary. Fig. B.6 shows the total uncertainty at each point and the corresponding histogram.

B.4 Temperature, T

We present a map of the uncertainty of the measured temperature for each pixel (Fig. B.7) using the equation for the temperature uncertainty (Eq. B.9), along with the uncertainty in the dielectric constant fit (Eq. B.10), the un-

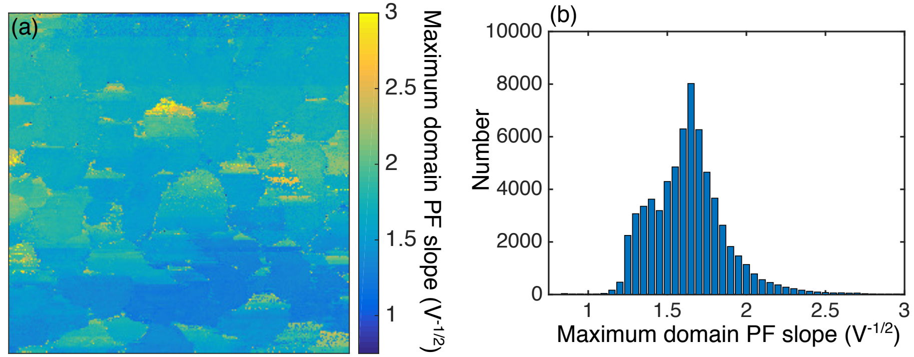

Figure B.3: (a) A map of the PF slope found by taking the maximum region considered to be PF (b) The corresponding histogram.

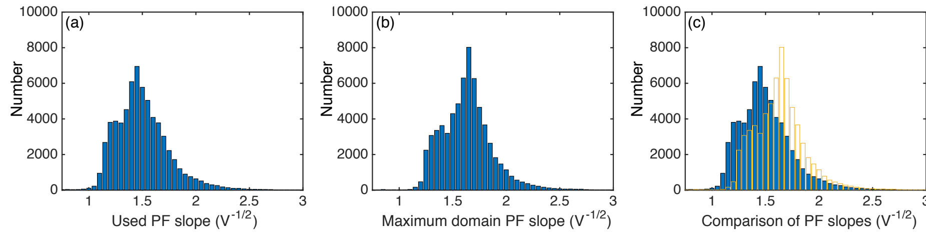

Figure B.4: (a) The histogram of the PF slope values used to calculate the temperature of the film. (b) The maximum domain PF slope values. (c) Superimposed histograms of minimizing the PF slope (blue) and the maximum domain slope (yellow outline).

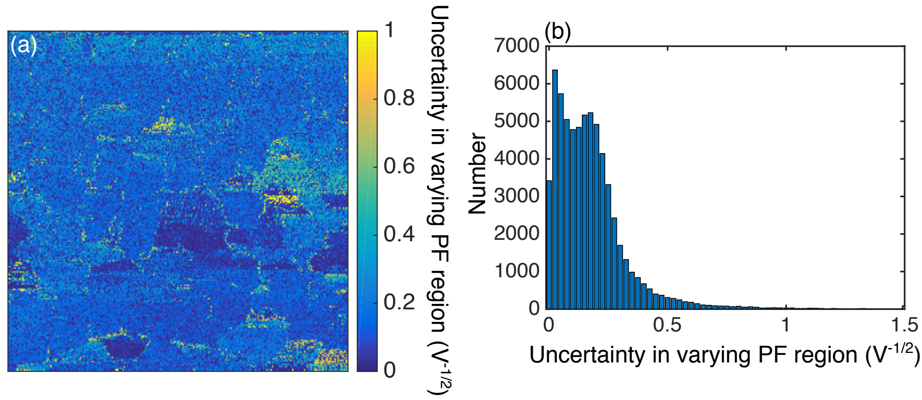

Figure B.5: (a) Map showing uncertainty due to a varying fit region. This uncertainty is the difference between the minimized PF slope at each point, and the PF slope by fitting the maximum domain. (b) Histogram of the difference between the minimized PF slope and the maximum domain PF slope.

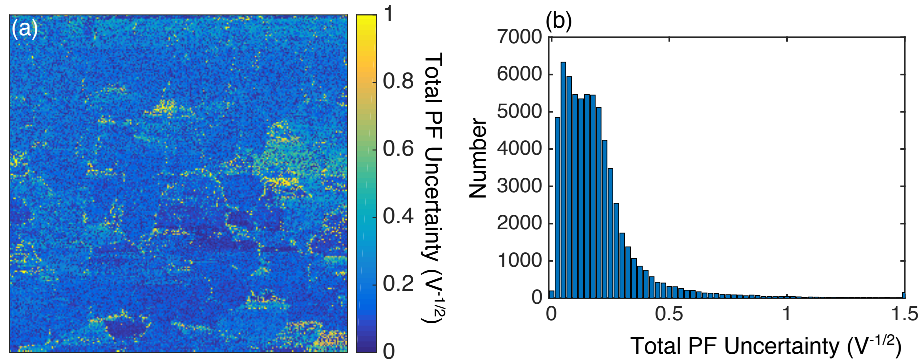

Figure B.6: (a) Map showing the total PF uncertainty due to the uncertainty in the linear fit added to the uncertainty due to the endpoints of the fit. (b) Histogram of the map of the total PF slope uncertainty.

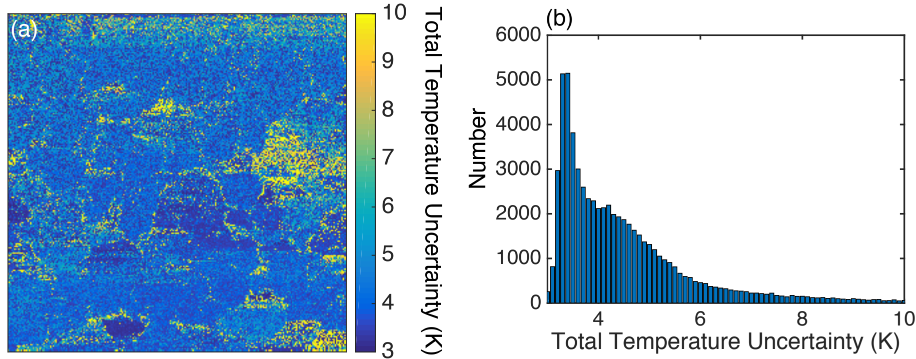

Figure B.7: (a) Map showing the uncertainty of T at each pixel. (b) Histogram of the δT map.

certainty in the film thickness (5 nm), and the uncertainty in fitting the PF slope (Fig. B.6). As shown in the histogram, most of the temperature uncertainty values are between 3 - 5 K, with a long tail for values greater than 5 K. The average uncertainty is 5.12 K, with a median of 4.14 K. By comparing to the PF uncertainty map (Fig. B.6) we note that the regions with the largest PF uncertainty also have the largest temperature uncertainty. For the majority of the pixels in the map, the uncertainty of each individual temperature measurement is less than $\sim$ 4.2 K. This temperature uncertainty is less than the overall standard deviation of the temperature map (5 K), and corroborates our calculated temperature values.

Appendix C

Model Circuit and Bounding Circuit Element Values

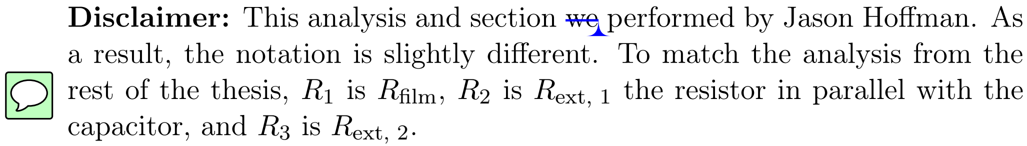

Disclaimer: This analysis and section we performed by Jason Hoffman. As a result, the notation is slightly different. To match the analysis from the rest of the thesis, R_1 is R_{film}, R_2 is $R_{\text{ext, 1}}$ the resistor in parallel with the capacitor, and R_3 is $R_{\text{ext, 2}}$.

Figure C.1 shows a schematic diagram of the circuit that we wish to analyze. The film resistance is given my R_1 in the insulating state, but changes to $R_{1'}$ in the metallic state. This is done by flipping the switch between the two states. Here, we assume the insulator to metal transition happens when the voltage source reaches 10 V.

C.1 Setting up equations for the upsweep

To begin, we write down Kirchhoff's current law

$$I_1(t) = I_2(t) + \frac{dQ(t)}{dt}, \tag{C.1a}$$

$$I_3(t) = I_2(t) + \frac{dQ(t)}{dt}. \tag{C.1b}$$

Our approach will be to solve for $Q(t)$, so we eliminate the other time dependent variables. To proceed, we know that the voltage drop across resistor R_2 and the capacitor must be equal, which allows us to write

$$I_2(t) R_2 = \frac{Q(t)}{C} \rightarrow I_2(t) = \frac{Q(t)}{R_2 C}. \tag{C.2}$$

Substituting Eqn. C.2 into Eqn. C.1, we obtain

$$I_1(t) = \frac{Q(t)}{R_2 C} + \frac{dQ(t)}{dt}, \tag{C.3a}$$

$$I_3(t) = \frac{Q(t)}{R_2 C} + \frac{dQ(t)}{dt}. \tag{C.3b}$$

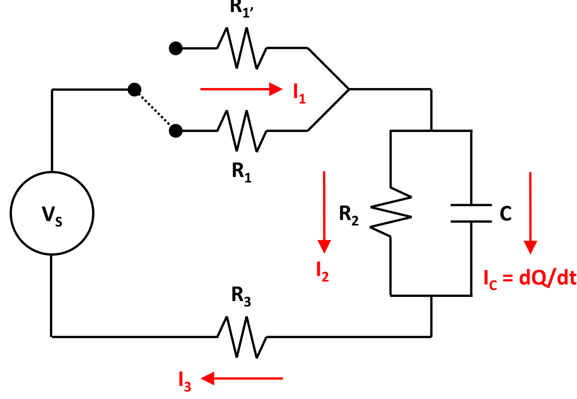

Figure C.1: The circuit we consider.

We now use Kirchoff's voltage law,

$$V_s(t) = I_1(t) R_1 + I_2(t) R_2 + I_3(t) R_3. \tag{C.4}$$

It is straightforward to plug Eqns. C.2 and C.3 into Eqn. C.4,

$$V_s(t) = R_1 \left(\frac{Q(t)}{R_2 C} + \frac{dQ(t)}{dt} \right) + \frac{Q(t)}{C} + R_3 \left(\frac{Q(t)}{R_2 C} + \frac{dQ(t)}{dt} \right). \tag{C.5}$$

We can rearrange terms to obtain,

$$V_s(t) = (R_1 + R_3) \frac{dQ(t)}{dt} + \left(\frac{R_1}{R_2} + \frac{R_2}{R_2} + \frac{R_3}{R_2} \right) \frac{Q(t)}{C}. \tag{C.6}$$

Rearranging further, we find that

$$\frac{dQ(t)}{dt} = \frac{1}{R_1 + R_3} \left[V_s(t) - \left(\frac{R_1 + R_2 + R_3}{R_2} \right) \frac{Q(t)}{C} \right]. \tag{C.7}$$

This is the differential equation that we must solve. Before going further, we have to know the source voltage, $V_s(t)$. We assume that the voltage changes linearly, with constant ramp rate, $\dot{V}$, with units volts per second, i.e., $V_s(t) = \dot{V} t$. Making this substitution,

$$\frac{dQ(t)}{dt} = \frac{1}{R_1 + R_3} \left[\dot{V} t - \left(\frac{R_1 + R_2 + R_3}{R_2} \right) \frac{Q(t)}{C} \right]. \tag{C.8}$$

We can rewrite this equation as,

$$\frac{dQ(t)}{dt} = \alpha t - \beta Q(t), \tag{C.9}$$

where

$$\alpha_{\mathrm{i}} = \frac{\dot{V}}{R_1 + R_3} \tag{C.10a}$$

and

$$\beta_{\mathrm{i}} = \frac{R_1 + R_2 + R_3}{R_2 C (R_1 + R_3)}. \tag{C.10b}$$

Here, we add a "$_\mathrm{i}$" subscript to explicitly note that we are considering the insulating state.

C.2 Solving the case of the Insulating State

We assume that the capacitor is uncharged initially, (i.e, $Q(t = 0) = 0$) and can use Matlab to find the solution to Eqn. C.9, which is

$$Q_{\mathrm{i}}^{\uparrow}(t) = \frac{\alpha_{\mathrm{i}} t}{\beta_{\mathrm{i}}} - \frac{\alpha_{\mathrm{i}}}{\beta_{\mathrm{i}}^2}\left[1 - \exp(-\beta_{\mathrm{i}} t)\right], \tag{C.11}$$

where we have added the $^{\uparrow}$ superscript to make explicit that we are dealing with the upsweep. Therefore,

$$\frac{dQ_{\mathrm{i}}^{\uparrow}(t)}{dt} = \frac{\alpha_{\mathrm{i}}}{\beta_{\mathrm{i}}}\left[1 - \exp(-\beta_{\mathrm{i}} t)\right]. \tag{C.12}$$

One can easily verify that Eqn. C.11 is the correct solution by plugging Eqns. C.11 and C.12 into Eqn. C.9. We can now calculate $I_{2,\mathrm{i}}^{\uparrow}(t)$, the current through resistor R_2 from Eqn. C.2.

C.2.1 Current through R_2

$$\begin{aligned} I_{2,\mathrm{i}}^{\uparrow}(t) = \frac{Q_{\mathrm{i}}^{\uparrow}(t)}{R_2 C} &= \left(\frac{\dot{V}}{R_1 + R_3}\right)\left(\frac{R_2 C (R_1 + R_3)}{R_1 + R_2 + R_3}\right)\left(\frac{t}{R_2 C}\right) \\ &- \left(\frac{\dot{V}}{R_1 + R_3}\right)\left(\frac{R_2 C (R_1 + R_3)}{R_1 + R_2 + R_3}\right)\left(\frac{R_2 C (R_1 + R_3)}{R_1 + R_2 + R_3}\right)\left(\frac{1}{R_2 C}\right) \\ &+ \left(\frac{\dot{V}}{R_1 + R_3}\right)\left(\frac{R_2 C (R_1 + R_3)}{R_1 + R_2 + R_3}\right)\left(\frac{R_2 C (R_1 + R_3)}{R_1 + R_2 + R_3}\right)\left(\frac{1}{R_2 C}\right)\exp(-\beta_{\mathrm{i}} t) \end{aligned} \tag{C.13}$$

$$I^{\uparrow}_{2,\mathrm{i}}(t) = \frac{\dot{V}t}{R_1+R_2+R_3} - \left(\frac{\dot{V}}{R_1+R_2+R_3}\right)\left(\frac{R_2C(R_1+R_3)}{R_1+R_2+R_3}\right) + \left(\frac{\dot{V}}{R_1+R_2+R_3}\right)\left(\frac{R_2C(R_1+R_3)}{R_1+R_2+R_3}\right)\exp(-\beta_{\mathrm{i}}t) \quad \text{(C.14)}$$

C.2.2 Current through the film

More importantly, we can calculate $I^{\uparrow}_{1,\mathrm{i}}$, which is the current through the film,

$$I^{\uparrow}_{1,\mathrm{i}}(t) = \frac{\alpha t}{\beta R_2 C} - \left(\frac{\alpha - \alpha\exp(-\beta t)}{\beta^2 R_2 C}\right) + \frac{\alpha - \alpha\exp(-\beta t)}{\beta}. \quad \text{(C.15)}$$

$$\begin{aligned} I^{\uparrow}_{1,\mathrm{i}}(t) = & \left(\frac{\dot{V}}{R_1+R_3}\right)\left(\frac{R_2C(R_1+R_3)}{R_1+R_2+R_3}\right)\left(\frac{t}{R_2C}\right) \\ & - \left(\frac{\dot{V}}{R_1+R_3}\right)\left(\frac{R_2C(R_1+R_3)}{R_1+R_2+R_3}\right)\left(\frac{R_2C(R_1+R_3)}{R_1+R_2+R_3}\right)\left(\frac{1}{R_2C}\right) \\ & + \left(\frac{\dot{V}}{R_1+R_3}\right)\left(\frac{R_2C(R_1+R_3)}{R_1+R_2+R_3}\right)\left(\frac{R_2C(R_1+R_3)}{R_1+R_2+R_3}\right)\left(\frac{1}{R_2C}\right)\exp(-\beta t) \\ & + \left(\frac{\dot{V}}{R_1+R_3}\right)\left(\frac{R_2C(R_1+R_3)}{R_1+R_2+R_3}\right) \\ & - \left(\frac{\dot{V}}{R_1+R_3}\right)\left(\frac{R_2C(R_1+R_3)}{R_1+R_2+R_3}\right)\exp(-\beta t) \end{aligned} \quad \text{(C.16)}$$

$$\begin{aligned} I^{\uparrow}_{1,\mathrm{i}}(t) = & \left(\frac{\dot{V}t}{R_1+R_2+R_3}\right) - \left(\frac{\dot{V}}{R_1+R_2+R_3}\right)\left(\frac{R_2C(R_1+R_3)}{R_1+R_2+R_3}\right) \\ & + \left(\frac{\dot{V}}{R_1+R_2+R_3}\right)\left(\frac{R_2C(R_1+R_3)}{R_1+R_2+R_3}\right)\exp(-\beta t) \\ & + \left(\frac{\dot{V}R_2C}{R_1+R_2+R_3}\right) - \left(\frac{\dot{V}R_2C}{R_1+R_2+R_3}\right)\exp(-\beta t) \end{aligned} \quad \text{(C.17)}$$

$$I^{\uparrow}_{1,\mathrm{i}}(t) = \left(\frac{\dot{V}t}{R_1+R_2+R_3}\right) + \left(\frac{\dot{V}R_2C}{R_1+R_2+R_3}\right)\left(1-\frac{R_1+R_3}{R_1+R_2+R_3}\right)(1-\exp(-\beta t)) \tag{C.18}$$

$$\boxed{I^{\uparrow}_{1,\mathrm{i}}(t) = \underbrace{\left(\frac{\dot{V}}{R_1+R_2+R_3}\right)}_{\text{Term 1}} t + \underbrace{\left(\frac{\dot{V}R_2^2C}{(R_1+R_2+R_3)^2}\right)}_{\text{Term 2}}(1-\exp(-\beta t))} \tag{C.19}$$

C.2.3 Current through the capacitor

The current though the capacitor is given by Eqn. C.12, which is reproduced below:

$$\frac{dQ^{\uparrow}_{\mathrm{i}}(t)}{dt} = \frac{\alpha_{\mathrm{i}}}{\beta_{\mathrm{i}}}\left[1-\exp(-\beta_{\mathrm{i}}t)\right].$$

The *steady state* current through the capacitor (i.e., for times much longer than β_{i}^{-1}) is given by

$$\bar{I}^{\uparrow}_{\mathrm{C,i}}(t) \approx \frac{\alpha_{\mathrm{i}}}{\beta_{\mathrm{i}}} = \frac{R_2C\dot{V}}{R_1+R_2+R_3}. \tag{C.20}$$

C.3 Solving the case of the Metallic State

We now turn to looking at the metallic state. We assume that the insulator to metal transition occurs instantaneously at a critical time, t_c. To model this, we assume that the switch closes, which changes the circuit quantitatively (but not qualitatively). We set up the problem the same way as before.

The differential equation that we need to solve is the same as before,

$$\frac{dQ'(t)}{dt} = \alpha' t - \beta' Q'(t), \tag{C.21}$$

where

$$\alpha' = \frac{\dot{V}}{R_{1'}+R_3} \quad \text{and} \tag{C.22a}$$

$$\beta' = \frac{R_{1'}+R_2+R_3}{R_2C(R_{1'}+R_3)} \tag{C.22b}$$

and the primes ($'$) indicate properties of the metallic state. The main difference between solving in insulating and metallic states is that in the metallic state, we can no longer assume that the capacitor is initially uncharged (in fact, it's fully charged by the time the insulator to metal transition takes place). So, now the boundary condition is $Q'(t = t_c) = Q(t = t_c)$. With the help of Matlab,

$$Q'(t) = \frac{\alpha'}{\beta'}t - \frac{\alpha'}{\beta'^2} + \left[\frac{\alpha}{\beta}t_c - \frac{\alpha'}{\beta'}t_c + \frac{\alpha'}{\beta'^2} - \left(\frac{\alpha - \alpha\exp(-\beta t_c)}{\beta^2}\right)\right]\exp\left(-\beta'(t - t_c)\right) \tag{C.23}$$

and

$$\frac{dQ'(t)}{dt} = \frac{\alpha'}{\beta'} - \beta'\left[\frac{\alpha}{\beta}t_c - \frac{\alpha'}{\beta'}t_c + \frac{\alpha'}{\beta'^2} - \left(\frac{\alpha - \alpha\exp(-\beta t_c)}{\beta^2}\right)\right]\exp\left(-\beta'(t - t_c)\right). \tag{C.24}$$

Let's make the following definition:

$$\gamma = \frac{\alpha}{\beta}t_c - \frac{\alpha'}{\beta'}t_c + \frac{\alpha'}{\beta'^2} - \frac{\alpha}{\beta^2}\left(1 - \exp(-\beta t_c)\right) \tag{C.25}$$

C.3.1 Current through R_2

The current through resistor 2 (the one in parallel with the stray capacitance) is,

$$I^{\uparrow}_{2,\mathrm{m}}(t) = \frac{Q'(t)}{R_2C} = \frac{\alpha'}{\beta' R_2C}t - \frac{\alpha'}{\beta'^2 R_2C} + \frac{\gamma}{R_2C}\exp\left(-\beta'(t - t_c)\right). \tag{C.26}$$

C.3.2 Current through the film

The current through the film can then be written,

$$I^{\uparrow}_{1,\mathrm{m}}(t) = \frac{\alpha'}{\beta' R_2C}t - \frac{\alpha'}{\beta'^2 R_2C} + \frac{\gamma}{R_2C}\exp\left(-\beta'(t - t_c)\right) + \frac{\alpha'}{\beta'} - \beta'\gamma\exp\left(-\beta'(t - t_c)\right). \tag{C.27}$$

$$I^{\uparrow}_{1,\mathrm{m}}(t) = \frac{\alpha'}{\beta' R_2C}t + \left(\beta' - \frac{1}{R_2C}\right)\frac{\alpha'}{\beta'^2} - \left(\beta' - \frac{1}{R_2C}\right)\gamma\exp\left(-\beta'(t - t_c)\right) \tag{C.28}$$

Now, we note that

$$\beta' - \frac{1}{R_2C} = \frac{R_{1'} + R_2 + R_3}{R_2C(R_{1'} + R_3)} - \frac{1}{R_2C} = \frac{1}{R_2C}\left(\frac{R_{1'} + R_2 + R_3}{R_{1'} + R_3} - \frac{R_{1'} + R_3}{R_{1'} + R_3}\right) = \frac{1}{C(R_{1'} + R_3)}. \tag{C.29}$$

With this simplification,

$$I^{\uparrow}_{1,\mathrm{m}}(t) = \frac{\alpha'}{\beta' R_2 C} t + \frac{1}{C\left(R_{1'} + R_3\right)} \left[\frac{\alpha'}{\beta'^2} - \gamma \exp\left(-\beta'\left(t - t_c\right)\right)\right] \tag{C.30}$$

$$\boxed{I^{\uparrow}_{1,\mathrm{m}}(t) = \underbrace{\frac{\dot{V} R_2^2 C}{\left(R_{1,\mathrm{m}} + R_2 + R_3\right)^2}}_{\text{Term 1}} + \underbrace{\left(\frac{\dot{V}}{R_{1,\mathrm{m}} + R_2 + R_3}\right)}_{\text{Term 2}} t - \underbrace{\frac{\gamma}{C\left(R_{1,\mathrm{m}} + R_3\right)}}_{\text{Term 3}} \exp\left(-\beta_{\mathrm{m}}\left(t - t_c\right)\right)} \tag{C.31}$$

The first term is a constant. Note that in the present model, this term must be *positive*, which is contrary to the measured data, which has a *negative* offset at $V = t = 0$. For this reason, we do not use this information in trying to determine the values of the circuit elements. One possible source on the negative offset is some form of nonlinear conduction in VO_2 in the metallic state (e.g., $I \propto V^2$).

The second term is the slope of the IV curve at high voltage (i.e., well above the IMT). We *do* use this data in determining the values of the circuit elements, as we believe it is mostly dominated by ohmic elements in the sample system and therefore well captured by the circuit model. For pixel [109, 109] (zero-indexed) the slope of the IV curve in the metallic state corresponds to 67,951.004 Ω. Thus, the first equation that we solve is:

$$\boxed{R_{1,\mathrm{m}} + R_2 + R_3 = 67,951.004.} \tag{C.32}$$

Obviously, this places some bounds on the values of the individual resistances:

$$\boxed{R_{1,\mathrm{m}} \leq 67,951.004\ \Omega} \tag{C.33}$$

$$\boxed{R_2 \leq 67,951.004\ \Omega} \tag{C.34}$$

$$\boxed{R_3 \leq 67,951.004\ \Omega} \tag{C.35}$$

The exponential decay time of the current in the metallic state is given by β_{m}^{-1}, which equals 310.7 μs. This gives us the second equation that we need to solve.

$$\boxed{\frac{R_2 C\left(R_{1,\mathrm{m}} + R_3\right)}{R_{1,\mathrm{m}} + R_2 + R_3} = \tau_{\mathrm{m}} = 3.107 \times 10^{-4}\ \mathrm{s}} \tag{C.36}$$

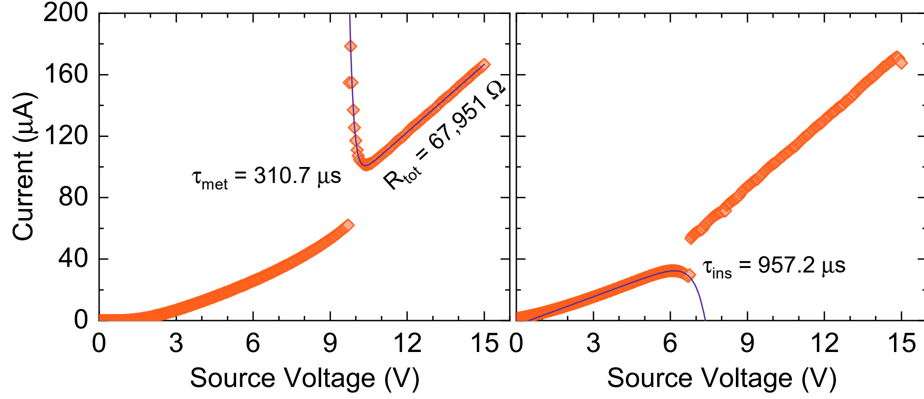

Figure C.2: *IV* curves.

We know the denominator on the left hand side of Eqn. C.36 from Eqn. C.32, and can therefore rewrite Eqn. C.36 as,

$$R_2C\,(67,951.004\ \Omega - R_2) = 21.115\ \Omega\cdot\text{s}. \tag{C.37}$$

This gives a quadratic equation,

$$-R_2^2C + 67,951.004R_2C - 21.115 = 0. \tag{C.38}$$

Using the quadratic formula,

$$R_2 = \frac{-67,951.004C \pm \sqrt{67,951.004^2C^2 - 4\cdot 21.115C}}{-2C}. \tag{C.39}$$

Because R_2 must be real, we require that the term under the radical be positive. To satisfy this condition,

$$67,951.004^2C^2 - 4\cdot 21.115C = 0, \tag{C.40}$$

which has two solutions: the trivial solution, $C = 0$, and a second solution at $C_{\text{critical}} = 1.829\times 10^{-8}$. We thus have another bound,

$$\boxed{C \geq 1.829\times 10^{-8}\ \text{F}} \tag{C.41}$$

At the critical capacitance, the resistance $R_2 = 67,951.004/2 = 33,975.502\,\Omega$.

C.4 Setting up equations for the downsweep

We can now consider the downsweep. There are several important facts to keep in mind for this step: (*i*) the voltage ramp rate is negative; (*ii*) the charge on the capacitor is nonzero at the start of the downsweep; (*iii*) the differential equation that we need to solve is no longer given by Eqn. C.21, but we use $V_s(t) = \dot{V} \times (t_{\mathrm{max}} - t)$ (i.e., $t = 0$ now corresponds to the start of the downsweep) to obtain

$$\frac{dQ_{\mathrm{m}}^{\downarrow}(t)}{dt} = t_{\mathrm{max}}\alpha_{\mathrm{m}} - \alpha_{\mathrm{m}}t - \beta_{\mathrm{m}}Q_{\mathrm{m}}^{\downarrow}(t) . \tag{C.42}$$

The boundary condition is given by, $Q_{\mathrm{m}}^{\downarrow}(t = 0) = Q_{\mathrm{m}}^{\uparrow}(t = t_{\mathrm{max}}) \equiv Q_{\mathrm{max}}$. The math here is ugly. I'll skip it.

C.4.1 Current through the film

The important part is that the exponential decay time of the current in the insulating state is given by β_{i}^{-1}, which equals 957.2 μs. This gives us the third equation that we need to solve:

$$\boxed{\frac{R_2 C\left(R_{1,\mathrm{i}} + R_3\right)}{R_{1,\mathrm{i}} + R_2 + R_3} = \tau_{\mathrm{i}} = 9.572 \times 10^{-4} \text{ s.}} \tag{C.43}$$

C.4.2 Lower bound on R_2

Returning to Eqn. C.36, we can write

$$C = \frac{\tau_{\mathrm{m}} R_2}{R_2\left(R_{\mathrm{total,m}} - R_2\right)}, \tag{C.44}$$

which we can then plug into Eqn. C.43 and then solve for R_2:

$$R_2 = \frac{R_{\mathrm{total,i}} \cdot R_{\mathrm{total,m}}\left(\tau_{\mathrm{i}} - \tau_{\mathrm{m}}\right)}{\tau_{\mathrm{i}} R_{\mathrm{total,i}} - \tau_{\mathrm{m}} R_{\mathrm{total,m}}}, \tag{C.45}$$

Which is plotted in Fig. C.3. We can derive two additional bounds from this equation. First, because $R_2 \geq 0$, the denominator must be positive (N.B. the numerator is always positive as $\tau_{\mathrm{i}} > \tau_{\mathrm{m}}$). Thus,

$$\tau_{\mathrm{i}} R_{\mathrm{total,i}} > \tau_{\mathrm{m}} R_{\mathrm{total,m}}, \tag{C.46}$$

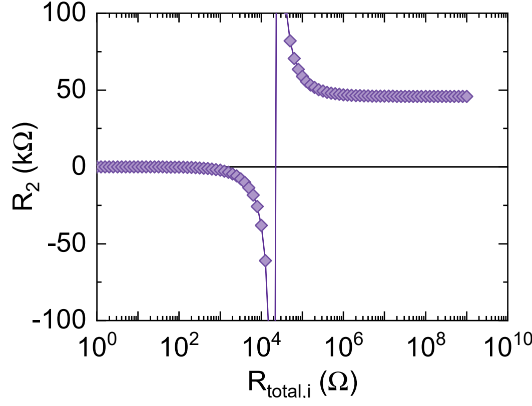

Figure C.3: Plot of Eqn. C.45 showing R_2 as a function of $R_{\mathrm{total,i}}$. Note that there is a critical value for $R_{\mathrm{total,i}}$ below which R_2 is negative. Also, as $R_{\mathrm{total,i}}$ increases R_2 approaches its limit asymptotically.

or,

$$\boxed{R_{\mathrm{total,i}} > \frac{\tau_{\mathrm{m}} R_{\mathrm{total,m}}}{\tau_{\mathrm{i}}} = 22,058.316\ \Omega.} \tag{C.47}$$

Second, in the limit $R_{\mathrm{total,i}} \to \infty$, we see (Fig. C.3) that R_2 asymptotically approaches a limiting value. Therefore,

$$\boxed{R_2 > \frac{R_{\mathrm{total,m}}\left(\tau_{\mathrm{i}} - \tau_{\mathrm{m}}\right)}{\tau_{\mathrm{i}}} = 45,892.688\ \Omega.} \tag{C.48}$$

This places upper bounds on the values of $R_{1,\mathrm{m}}$ and R_3 and $R_{1,\mathrm{m}} + R_3$:

$$\boxed{R_{1,\mathrm{m}} \leq R_{\mathrm{total,m}} - R_2^{\mathrm{min}} = 22,058.316\ \Omega,} \tag{C.49}$$

$$\boxed{R_3 \leq R_{\mathrm{total,m}} - R_2^{\mathrm{min}} = 22,058.316\ \Omega,} \tag{C.50}$$

$$\boxed{R_{1,\mathrm{m}} + R_3 \leq R_{\mathrm{total,m}} - R_2^{\mathrm{min}} = 22,058.316\ \Omega.} \tag{C.51}$$

C.5 Summary

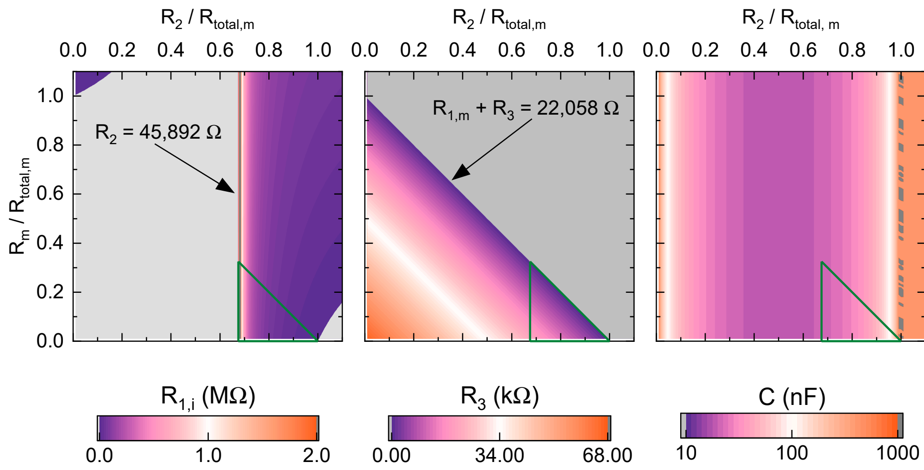

Figure C.4: Wide area maps of insulating state resistance of the film ($R_{1,\mathrm{i}}$), external resistor 2 (R_3), and the capacitance (C). Note that the green triangle denotes the region where all bounds are satisfied.

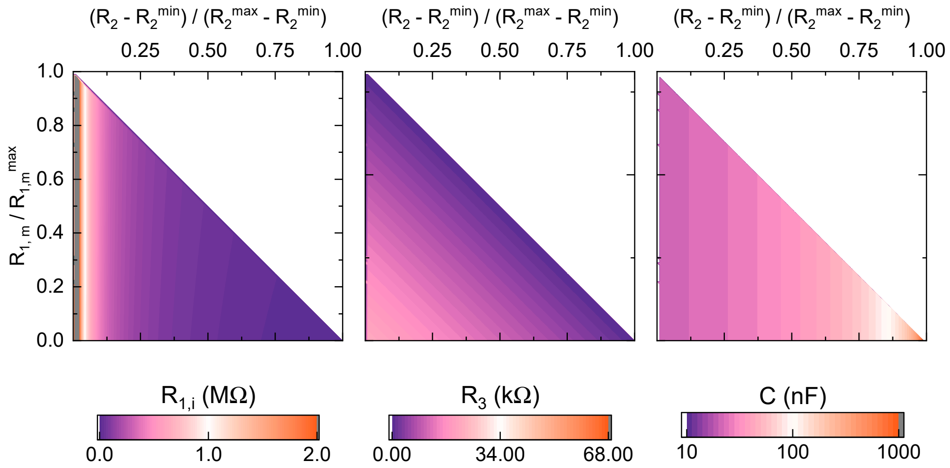

Figure C.5: Same as above, but only calculated over the region where all constraints are satisfied.

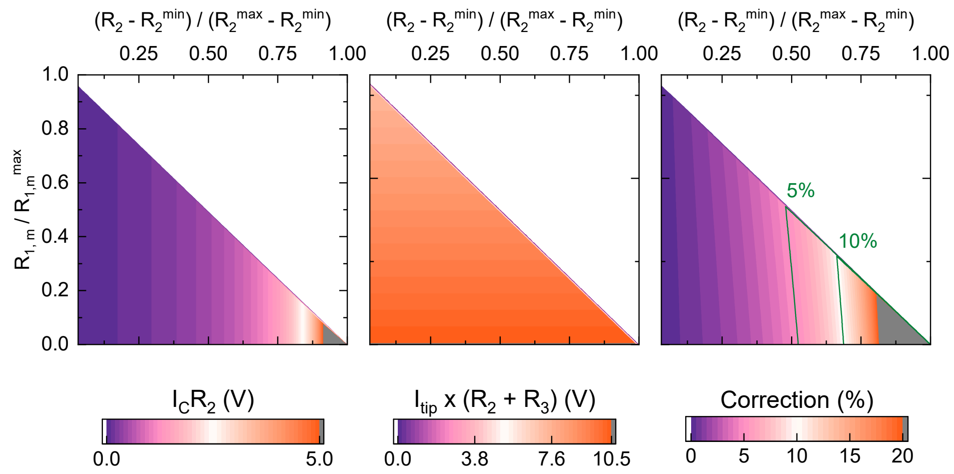

Figure C.6: Maps showing the various correction terms to the voltage across the film. The third panel shows the correction due to the current through the capacitor as a percentage of the correction due to the non-film resistances. Over a large fraction of the plausible parameter space, the correction is less than 10%.